

RADIO FREQUENCY SIGNAL PROCESSING WITH
MICROELECTROMECHANICAL RESONATING SYSTEMS

A Dissertation

Presented to the Faculty of the Graduate School
of Cornell University

In Partial Fulfillment of the Requirements for the Degree of
Doctor of Philosophy

by

Robert Bruce Reichenbach

August 2006

© Robert Bruce Reichenbach 2006

RADIO FREQUENCY SIGNAL PROCESSING WITH MICROELECTROMECHANICAL RESONATING SYSTEMS

Robert Bruce Reichenbach, Ph.D.

Cornell University 2006

This thesis presents a study of the dynamics and applications of a high frequency micromechanical (MEMS) resonator. Mechanical systems, which have been scaled in dimension to the micron scale, show promise for replacing electrical resonant systems, which have larger physical size and lower performance. MEMS resonators can also be integrated into a chip containing conventional field effect transistors. A process incorporating both frequency dependent resonant systems as well as analog and digital electronics will enable all hardware in a communication architecture to be placed on a single silicon chip.

In this study, a micron-sized circular membrane, suspended in the middle and clamped on the periphery, forms the basis of the resonant mechanical system. A small degree of curvature is fabricated into the resonator, which serves to stiffen the device and hence increase the frequency range. A microheater, defined in proximity to the resonator, is used to induce motion in the membrane. The frequency dependent response of the membrane is then detected through either interferometric or piezoresistive techniques.

Resistive actuation and detection allow the membrane and actuators to be fabricated into a single plane of silicon, facilitating integration of the complete MEMS system. It is demonstrated how both the resonators and transducers can be implemented into two CMOS processes. Both designs incorporate the mechanical

system as well as the solid-state electronics for output signal detection into a single fabrication process.

Finally, the dynamics of the MEMS resonator, both in the linear and non-linear regime, are explored. The micron-sized mechanical system is demonstrated to perform several types of signal processing that are critical for wireless communication architectures. These studies shed new light on how the nonlinear dynamics of these systems may be characterized and harnessed for new applications.

BIOGRAPHICAL SKETCH

Robert B. Reichenbach was born in Grand Rapids, MI on July 17th, 1978. He grew up in Roseville and Shoreview, MN (two suburbs of the Twin Cities) and attended Minnehaha Academy for junior high and high school. Rob's youth was formed around numerous trips into the boundary water canoe area as well as yearly trips around the U.S. and world with his parents. He was gainfully employed by such prestigious companies as OfficeMax and also tried to strike it rich selling lawn care services, strawberries, Christmas ornaments and even maple seeds to neighbors.

Following high school, Rob went to Hope College, a small liberal arts school in Holland, MI. There he studied engineering and also filled his capitalism interests with an economics degree. The summer after his sophomore year he met a nice girl named Kristen Lantz at the Hope College engineering REU program. His junior year he was inducted into the Baker Scholar program, which would provide him many exciting forays into the business world. The following summer he and Kristen again participated in a REU program, this time at Lawrence Berkeley National Lab, in Berkeley, CA, where virtually every weekend was spent camping at a national park. In May 2001 he graduated from Hope with a B.S. in Engineering and a B.A. in Economics.

Although his mother wanted him to pursue biology, his father had philosophy in mind, and his grandfather was always suggesting the Army, Rob decided to begin pursuit of a Ph.D. in electrical engineering at Cornell University, Ithaca, NY. It also happened that Kristen thought a PhD at Cornell was a good idea as well. The summer between college and graduate school, Kristen and he (notice a trend?) spent traveling and camping in the Baja, Mexico peninsula.

During his first summer at Cornell, he convinced Professor Harold Craighead and Professor Jeevak Parpia to allow him to work in their joint research group. About this time, Rob also decided that he was fed up with renting and was going to buy a house; however, with very little financial resources, all he could find was a fixer-upper. With the help of his parents, sister, Kristen, and some good friends, he turned a beat-up rental on West Buffalo Street into a wonderful place to live. By fall 2002, he was working closely with a team of scientists, Maxim Zalalutdinov and Keith Aubin, in the Craighead-Parpia group on microelectromechanical systems.

In January 2003, Rob decided that Kristen was the right one for him and proposed to her on the shore of Lake Michigan, in Holland, MI. where they first met. Later in 2003, Rob, Keith, and Max entered their dome resonator in a collegiate competition at the National Inventors Hall of Fame. They were selected as one of the graduate prize winners and were subsequently inundated with requests for interviews and articles. After the chaos calmed down and real work resumed, they decided to give commercialization of their technology a shot, partnering with a company called Innovative Biotechnology International to pitch their product to many companies.

6-5-4 was the big date for Kristen and Rob, deciding to get hitched in Kristen's home town of Baraboo, WI. Two days later, they were off to a dream honeymoon on the Caribbean Islands of Puerto Rico, St. Lucia, and Grenada. Back in the lab, research on MEMS resonators and related topics continued over the next two years.

Receiving his PhD in August 2006, now comes the time for Rob to choose his future path – will it be engineering, entrepreneurship, or wilderness? Either way, he will be happy with Kristen by his side.

To my wife, Kristen

ACKNOWLEDGMENTS

A PhD is more than just a dissertation, it is an amalgamation of whom you collaborate with, study under, and interact with, as well as what you have learned. The realization of the work in this thesis undoubtedly would not have been possible without the contributions from the following people. First and foremost, I would like to thank my advisors Professor Harold Craighead and Professor Jeevak Parpia for letting me pursue my interests in the field of RF micromechanical resonators. Their combination of micro and macro managing allowed me to find guidance and develop persistence in my scientific journey.

I would also like to thank Professor Parpia's research associate, Maxim Zalalutdinov, – now at NRL – for teaching me the definition of “ridiculous” and “work harder”. Without his ideas, late night discussions, and interesting methods of motivation, I would still be at square one. Similarly, the seemingly endless patience, creativity, and knowledge contributed by Professor Craighead's graduate student, Keith Aubin, is the foundation of much that I have learned and accomplished during my graduate work.

I would like to thank Professor Richard Rand for his collaboration on modeling the nonlinear dynamics of MEMS and for inspiration of someone who truly sees his work in all aspects of life. Thanks are also due to graduate students Manoj Pandey for much discussion on modeling and system dynamics, Seppe Kuehn, Tad Kaburaki, Arend Van Der Zande, and Scott Verbridge. I greatly appreciate Professors Amit Lal, Sunil Bhave and Alan Zehnder for letting me spontaneously drop by and discuss my research. The entire CNF staff, most notably Rob “Bubbles” Ilic, deserve due praise for patience with seemingly endless processing questions and problems. The graduate

students of the Craighead research group also receive credit for enduring group talk, random advice, and friendship.

Finally, I would like to thank my parents, Bruce and Sharon, sister, Rachel, and grandparents for their encouragement, support and interest in whatever I am doing. Perhaps most important, I would like to thank my wife Kristen, for her companionship, patience, skepticism, and knowledge that is a continual inspiration to me.

TABLE OF CONTENTS

BIOGRAPHICAL SKETCH.....	iii
ACKNOWLEDGMENTS.....	vi
TABLE OF CONTENTS.....	viii
LIST OF FIGURES.....	x
1 Introduction	1
1.1 Micro/Nano Mechanical Systems.....	1
1.2 Historical Perspective on Micromechanics	3
1.3 Types of RF Micromechanical Resonators	5
1.4 Resonant Mechanical Analysis.....	7
1.5 High Frequency Actuation	13
1.5.1 Electrostatic	13
1.5.2 Piezoelectric	15
1.5.3 Lorentz.....	16
1.5.4 Thermal.....	16
1.6 High Frequency Detection.....	18
1.6.1 Electrostatic	18
1.6.2 Interferometric Detection	21
1.6.3 Piezoresistive Detection	23
2 The Shell-Type, High Frequency, Micromechanical Resonator	25
2.1 Fabrication.....	25
2.2 Higher Frequencies.....	34
2.3 Damping	38
3 Integrated Resistive Transduction.....	44
3.1 Resistive Actuation.....	44
3.2 Resistive Detection.....	52
3.3 DC Heating Frequency Control and Temperature Effects	62
4 CMOS Integration of MEMS Resonators.....	64
4.1 Introduction	64
4.2 3D-SOI	65
4.3 IBM BICMOS	74
5 Micromechanical Radio Frequency Signal Processing.....	82
5.1 The Basic RF Communication Architecture	82
5.2 MEMS Filter.....	86
5.3 MEMS Mixer.....	88
5.4 MEMS RF Radio Receiver.....	93
5.5 MEMS Oscillator.....	95
5.6 Voltage Controlled MEMS Oscillator.....	101
5.7 Phase Tunable MEMS Emitter	103
6 Nonlinear Dynamics of MEMS Resonators	111
6.1 Non-Linear Effects in Communications.....	111
6.2 Resonator Non-Linear Effects.....	112
6.3 Analytical Model for Intermodulation.....	121

7	Conclusion	125
	Appendix A: Autostep 200 Setup Parameters	127
	Appendix B: Macsyma code to solve ODE (6-4)	129
	References	131

LIST OF FIGURES

Figure: 1-1	First MEMS Resonator.....	4
Figure: 1-2	Micromechanical Resonator.....	11
Figure: 1-3	Classical Mass-Spring System.....	11
Figure: 1-4	Frequency Dependent Amplitude Response.....	12
Figure: 1-5	Frequency Dependent Phase Response.....	12
Figure: 1-6	Electrostatic Transducer Impedance.....	20
Figure: 1-7	Optical Interference Pattern Calculation.....	22
Figure: 2-1	Dome Fabrication Process.....	30
Figure: 2-2	Dome Micrographs.....	31
Figure: 2-3	Resonant Frequency Calculation.....	31
Figure: 2-4	Dome Frequency Spectrum.....	32
Figure: 2-5	Simulated Mode Shapes of Dome.....	32
Figure: 2-6	Experimental Mode Shapes of Dome.....	33
Figure: 2-7	High Frequency Response.....	35
Figure: 2-8	Calculated Advantage Provided by Curvature.....	36
Figure: 2-9	Fabrication Process for Hemispherical Dome.....	36
Figure: 2-10	Hemispherical Dome Micrograph.....	37
Figure: 2-11	Micrograph of Mesa Domes.....	42
Figure: 2-12	Experimental Results of Mesa Domes.....	43
Figure: 2-13	Resonance in Air.....	43
Figure: 3-1	Resistor and Resonator Micrograph.....	49
Figure: 3-2	Simulated Temperature and Deflection in Dome.....	50
Figure: 3-3	Resonator with Adjacent Resistor.....	50
Figure: 3-4	Vacuum Test Chamber Setup.....	51
Figure: 3-5	Experimental Effect of DC Bias.....	51
Figure: 3-6	Micrograph of Resistive Transducers.....	56
Figure: 3-7	Gauge Factor in Silicon.....	57
Figure: 3-8	Piezoresistor Implantation Profile.....	58
Figure: 3-9	Response from Resistively Coupled Resonator.....	59
Figure: 3-10	Response of Resonator Coupled to OP Amplifier.....	60
Figure: 3-11	Electrical-Mechanical Signal Path.....	60
Figure: 3-12	Integrated Experimental Setup.....	61
Figure: 3-13	Diagram of Resonator and OP Amplifier.....	61
Figure: 4-1	3D SOI Wafer stack.....	69
Figure: 4-2	Process for Integrating Membrane in 3D SOI.....	70
Figure: 4-3	Resonance of Membrane in 3D SOI process.....	71
Figure: 4-4	Cadence Layout of 3D SOI process.....	72
Figure: 4-5	Circuit Schematic of 3D SOI Detection Electronics.....	73
Figure: 4-6	Simulated Response of Detection Electronics.....	73
Figure: 4-7	Cadence Layout of Membrane in IBM BiCMOS process.....	77
Figure: 4-8	Process for Integrating Membrane in IBM BiCMOS.....	78
Figure: 4-9	Parasitic Capacitive Voltage Division.....	79

Figure: 4-10	Cadence Layout of IBM BiCMOS process	80
Figure: 4-11	Circuit Schematic of IMB BiCMOS Detection Electronics.....	81
Figure: 5-1	Heterodyne Receiver Schematic.....	84
Figure: 5-2	CMDA PCS Heterodyne Receiver	85
Figure: 5-3	CMDA PCS Cell Phone	85
Figure: 5-4	Multiple Order MEMS Filter.....	87
Figure: 5-5	MEMS Mixer Diagram.....	91
Figure: 5-6	Input Impedance of MEMS Mixer	91
Figure: 5-7	Experimental Mixing Characteristics	92
Figure: 5-8	MEMS Radio Diagram.....	94
Figure: 5-9	Dome Oscillator Schematic	98
Figure: 5-10	Dome Oscillator Spectrum	99
Figure: 5-11	Stability of Dome Oscillator.....	99
Figure: 5-12	Resistively Transduced Dome Oscillator	100
Figure: 5-13	MEMS Oscillator Tuning	102
Figure: 5-14	Micrograph of Dual Drive Dome	102
Figure: 5-15	Dome Resonator Entrainment Schematic.....	107
Figure: 5-16	Experimental Entrainment V.....	107
Figure: 5-17	Conceptual Source of Phase Lag in Locked System	108
Figure: 5-18	Experimental Phase Lag in MEMS System	109
Figure: 5-19	Schematic of MEMS Phase Shifter and Modulator	109
Figure: 5-20	Rate of FM and PM Modulation	110
Figure: 6-1	Nonlinear Response of Dome.....	117
Figure: 6-2	Nonlinear Duffing Backbone Curve.....	118
Figure: 6-3	Intermodulation Measurement Schematic	119
Figure: 6-4	IM ₃ Experimental Results.....	119
Figure: 6-5	Experimental Resistive Drive Power Sweep.....	120
Figure: 6-6	Conceptual Source Nonlinear Effects	120
Figure: 6-7	Experimental Validation of IM ₃ Model.....	124

1 Introduction

1.1 Micro/Nano Mechanical Systems

Much research has been focused on using well-developed and commonplace integrated circuit (IC) fabrication techniques to create micro-miniaturized mechanical devices made out of materials such as silicon, silicon-oxide, silicon-nitride and various metals. Such components can be implemented as sensors, switches, actuators, valves, and gears and offer tremendous advantages in size, cost, and power consumption over their macro-scaled counterparts. These devices are typically fabricated out of or onto a semiconductor substrate which may also contain solid state electronics to interface with the MEMS device enabling large scale system integration.

Recently, radio-frequency microelectromechanical systems (RF MEMS) have been developed which can manipulate or produce electrical signals in communication systems by implementing MEMS as frequency and phase determining elements within the mechanical domain. MEMS signal processing is made possible by scaling laws that shorten the time of mechanical response and increase the resonant frequency of micron-size mechanical structures into the MHz or GHz range. By converting electrical signals into mechanical motion and leveraging linear and nonlinear resonant properties, MEMS can be used to change the characteristics of an incident signal, or even selectively generate a new signal. Tailoring the geometry of the micromechanical devices tunes the characteristic response of the resonator to cover the many frequency bands used in modern communications, leading to a broad range of applications.

The draw to use RF MEMS imparts from several significant performance advantages over their electrical counterparts. Low material damping and minimal

nonlinear effects reduce signal distortion and permit very narrow band performance. Additionally, their small physical dimensions and ability to be integrated along side solid-state ICs are advantageous for eliminating components such as III-V mixers, quartz crystal oscillators, and off-chip filters, enabling significant scaling in modern communication systems. Integration of RF MEMS resonators, sensors, and electronics that share the same silicon substrate yields a complete single die package rather than discrete components with a variety of process technologies and packages. Merging electrical and mechanical components into one process is a critical step toward the realization of a complete radio-on-chip product which will be applicable to modern portable communication handsets.

The focus of this research is to develop a MEMS resonator and corresponding transduction electronics, which would be ideal for radio-on-chip based applications, and to demonstrate the functionality of using MEMS as the critical building blocks of wireless communication architectures. To be commercially viable, this MEMS device must be able to be integrated into a conventional CMOS environment, while at the same time occupy minimal physical space, consume less power and demonstrate superior performance when compared to conventional components.

This thesis presents research on a complimentary-metal-on-oxide (CMOS) process compatible, high frequency, shell-type, MEMS resonator, which uses resistive transduction to thermally couple MHz-range electrical signals into the mechanical resonator and to subsequently convert high frequency mechanical motion back into an electrical signal. The RF resonator is demonstrated to replace fundamental components in a heterodyne receiver such as high frequency and intermediate frequency filters, wide-band mixers, and low phase noise voltage controlled oscillators [1,2]. Based on these components an actual FM heterodyne MEMS radio is implemented. To discuss and quantify the component's performance, the nonlinear

behavior of the MEMS system is measured and modeled. Finally, several methods are presented to integrate the shell-type resonator and its corresponding transduction electronics into a standard CMOS fabrication process, which is a fundamental step in the development of a complete radio-on-chip package [3].

1.2 Historical Perspective on Micromechanics

The concept of a moving silicon microstructure which can be controlled by electrical signals has been experimentally pursued for almost 40 years. In 1967 Nathanson et al. at Westinghouse conceived the idea of a resonant cantilever transistor gate electrode (figure 1-1). The 100 μm long cantilever was controlled with electrostatic forces and its corresponding motion modulated the gate capacitance of a field effect transistor, enabling electrical readout of the 5 kHz, $Q = 500$ mechanical motion [1]. In 1979, IBM, using conventional IC photolithography, fabricated a beam of silicon that could be used as an electrostatically controlled mechanical relay or switch on the micron scale [5]. These two discoveries were paramount for establishing interest in micromechanics. The 80s and 90s saw the co-development of silicon processing for integrated circuits (ICs) and MEMS technology. MEMS switches and phase shifters were designed specifically for microwave applications [6]. Commercial development concentrated on low frequency MEMS as pressure sensors, accelerometers and temperature sensors for automotive applications and micro mirrors for projection. In the early 90s, MEMS varactors and inductors began to be developed in research labs, and finally in the late 90s and early 2000s micromechanical resonators for RF communications began to emerge [7, 8]. In 2002, Agilent revealed its high- Q FBAR filter complete with chip-scale packaging, and presently there are several startup companies (Discera, Si-Clocks, Silicon Time,

Harmonic Devices) working toward implementing resonant RF micromechanics into modern communication architectures.

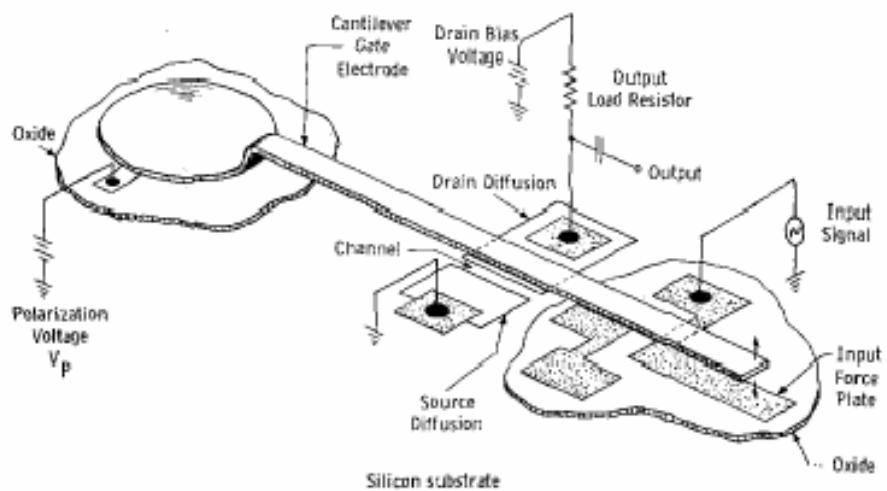


Figure 1-1: The resonant cantilever transistor gate electrode widely regarded to be the first MEMS device. Reproduced from [4] ©1967 IEEE.

1.3 Types of RF Micromechanical Resonators

There are two main classes of micromechanical resonators that have resonant frequencies capable of reaching the MHz or GHz range (necessary for mechanical signal processing): flexural and extensional resonators. Flexural resonators, previously demonstrated in [9, 10] are thin film geometries with one or more anchoring points in which vibrations are primarily characterized by bending modes. A cantilever, more or less the micron-sized equivalent of a swimming pool diving board, is a beam with one fixed end and one free end. The fundamental mode of vibration is characterized by out-of-plane beam deflection at the free end. A doubly clamped beam on the other hand has two anchor points and, in the fundamental mode, has an out-of-plane displacement maximum half way between the anchors. Recent research [11,12] has focused on mushroom type flexural resonators, which are thin film circular disks supported by a central oxide pillar. Quality factors of flexural resonators have been demonstrated to be as large as 200,000 [13,14], opening the door for applications requiring extremely sensitive measurements.

Generally speaking, this class of resonator is relatively easy to produce. The microresonators are primarily fabricated out of a thin structural film which can be patterned and subsequently exposed to a selective chemical etch to remove sacrificial material below a beam or disk, creating a suspended structure.

Flexural resonators have numerous advantages. First, they are low mass and can therefore be configured to be sensitive to external perturbations such as temperature, pressure, and added mass [15,16]. Second, their frequency is defined by both the lateral dimensions of the resonator as well as by the spring constant, which is the bending modulus (usually on the order of a few N/m) of the material, allowing macroscopic and microscopic tuning of resonator frequency. Finally, flexural

resonators typically have large mechanical displacements, facilitating motion detection.

A second, relatively new type of resonator is the extensional mode resonator, otherwise known as a bulk acoustic wave (BAW) resonator. Vibrations are characterized by either in-plane expansion of a plate resonator [17,18], or expansion through the film thickness [19,20]. The resonant frequency of the in-plane BAW resonator is determined by the lateral dimensions and the 2-D extensional modulus, which depends primarily on the Young's modulus of the material.

BAW resonators offer the advantage of having high quality factors, high resonant frequencies, and low transduction losses, but require very narrow gaps surrounding the resonator to produce detectable displacement. BAW devices from companies such as Agilent and Infineon already established themselves in cell phones as duplexers and front end filters. The FBAR duplexer, by January 2005, had already captured more than 70 percent of the CDMA phone segment [21, 22].

The subject of this research is a hybrid design between the flexural and extensional resonators. The resonator is a circular membrane which is supported by an infinitely clamped periphery [23]. A slight degree of curvature in the membrane causes the device to resemble the basin of a steel drum rather than the membrane of a timpany drum. This curvature makes resistance to out-of-plane mechanical displacement a function of both bending and extensional resistance. This design allows the shell resonator to achieve high membrane displacement to facilitate motion detection, while also, due to the added stiffness from the curvature, increases the resonant frequency over traditional flexural resonators.

1.4 Resonant Mechanical Analysis

The behavior of a micromechanical resonator is modeled as a damped, driven harmonic oscillator. The micromechanical structure in figure 1-2 (a doubly clamped paddle oscillator) is identical to a simple mass-spring system (figure 1-3) where the force pulling the suspended mass back towards the equilibrium position is provided by the stiffness of the material. In extensional mode resonators the spring constant is determined by the elongation resistance (the Young's modulus) in the resonator mass, while in flexural resonators, the spring is represented by the bending resistance of a membrane.

The mass-spring mechanical system is governed by a linear differential equation that balances forces according to Newton's 2nd law. The forces acting on the mass are the external driving force, $F(t)$, the restoring force proportional to the displacement, and the damping force proportional to the speed:

$$m \frac{d^2 x}{dt^2} + c \frac{dx}{dt} + kx = F(t). \quad 1-1$$

An analogous system that obeys a similar differential equation is the inductor-capacitor-resistor (LCR) tank circuit,

$$L \frac{d^2 q}{dt^2} + R \frac{dq}{dt} + q/C = V(t), \quad 1-2$$

where charge (q) is the electrical equivalent of the mechanical displacement around the equilibrium position (x), the inductance (L) is related to the mass (m), the

resistance (R) is the damping or loss coefficient (c), and the capacitance (C) is inversely related to the mass-spring system spring constant, (k).

Proceeding with the mechanical model, dividing out the mass and writing $c = \omega_o m / Q$ and $k = \omega_o^2 * m$, 1-1 becomes

$$\frac{d^2 x}{dt^2} + \frac{\omega_o}{Q} \frac{dx}{dt} + \omega_o^2 x = \frac{F(t)}{m} \quad 1-3$$

An arbitrary sinusoidal driving force can be written as $F_o \cos(\omega t + \Delta)$. Using Euler's identity, $e^{i\omega t} = \cos \omega t + i \sin \omega t$, $F(t)$ can then be expressed in complex notation as

$$F(t) = F_o^{-j\Delta} e^{j\omega t} = \hat{F} e^{j\omega t} \quad 1-4$$

where the driving force is the real part of $F(t)$. We can then guess a solution to 1-3 of the form $x(t) = \hat{x} e^{j\omega t}$, where the displacement is the real part of $x(t)$. Substituting the complex expressions for $x(t)$ and $F(t)$ into 1-3, we evaluate the derivatives and get

$$(j\omega)^2 \hat{x} e^{j\omega t} + \frac{\omega_o}{Q} (j\omega) \hat{x} e^{j\omega t} + \omega_o^2 \hat{x} e^{j\omega t} = \frac{\hat{F}}{m} e^{j\omega t} \quad 1-5$$

Solving for \hat{x} , we find the response of the system to be

$$\hat{x} = \frac{\hat{F}}{m(\omega_o^2 - \omega^2 + \frac{j\omega_o \omega}{Q})} \quad 1-6$$

Thus the magnitude of the displacement is related to the product of the force (\hat{F}) and

the factor $\hat{S} = \frac{1}{m(\omega_o^2 - \omega^2 + \frac{j\omega_o\omega}{Q})}$. To isolate the real and imaginary parts of this

scaling factor we multiply both the numerator and denominator by the complex conjugate:

$$\hat{S} = \frac{1}{m(\omega_o^2 - \omega^2 + \frac{j\omega_o\omega}{Q})} \cdot \frac{m(\omega_o^2 - \omega^2 - \frac{j\omega_o\omega}{Q})}{m(\omega_o^2 - \omega^2 - \frac{j\omega_o\omega}{Q})} \quad 1-7$$

$$= \frac{\omega_o^2 - \omega^2 - \frac{j\omega_o\omega}{Q}}{m \left[(\omega^2 - \omega_o^2)^2 + \left(\frac{\omega_o\omega}{Q} \right)^2 \right]} = \frac{\omega_o^2 - \omega^2}{m \left[(\omega^2 - \omega_o^2)^2 + \left(\frac{\omega_o\omega}{Q} \right)^2 \right]} - j \frac{\frac{\omega_o\omega}{Q}}{m \left[(\omega^2 - \omega_o^2)^2 + \left(\frac{\omega_o\omega}{Q} \right)^2 \right]} \quad 1-8$$

The square magnitude of equation 1-8 is the amplitude of \hat{S} ; therefore if $\hat{S} = \rho e^{j\theta}$, 1-6 can be rewritten as the following

$$\hat{x} = \hat{F}\hat{S} = F_o e^{j\Delta} \rho e^{j\theta} = F_o e^{j(\Delta+\theta)} \sqrt{\frac{1}{m^2 \left[(\omega^2 - \omega_o^2)^2 + \left(\frac{\omega_o\omega}{Q} \right)^2 \right]}} \quad 1-9$$

Recalling that $x(t) = \text{Re}(\hat{x}e^{j\omega t})$ and therefore $x(t) = \rho F_o \cos(\omega t + \Delta + \theta)$, the absolute amplitude of displacement is ρF_o , where ρ is plotted in figure 1-4. When the driving frequency, ω , matches the characteristic frequency of the resonator, ω_o , the mechanical displacement is enhanced by the factor Q and large amplitude motion

occurs. If the damping term were not included in (1-1), the response at $\omega = \omega_o$ would be infinite; however, any damping exerted on the resonator will limit the on resonance amplitude of vibration.

The phase angle added by the resonator, which is the time delay between the driving force and the mechanical response, is given by

$$\theta = \tan^{-1}\left(\frac{\text{Im}(\hat{S})}{\text{Re}(\hat{S})}\right) = \tan^{-1}\left(\frac{-\omega_o\omega}{Q(\omega_o^2 - \omega^2)}\right). \quad 1-10$$

Since $x(t) = \rho F_o \cos(\omega t + \Delta + \theta)$, the phase lag of the resonant circuit is simply added onto the lag of the driving signal.

Plotting θ vs. ω in figure 1-5, we find that at driving frequencies much below ω_o , the response of the mass is in-phase with the driving force. On resonance the drive and the mechanical amplitude are 90° out of phase, while at frequencies much higher than ω_o the response lags the driver by 180° . Thus the phase of the mechanical motion in relation to the input varies depending on the instantaneous frequency of operation (ω). This significance will be put into context in section 5.7.

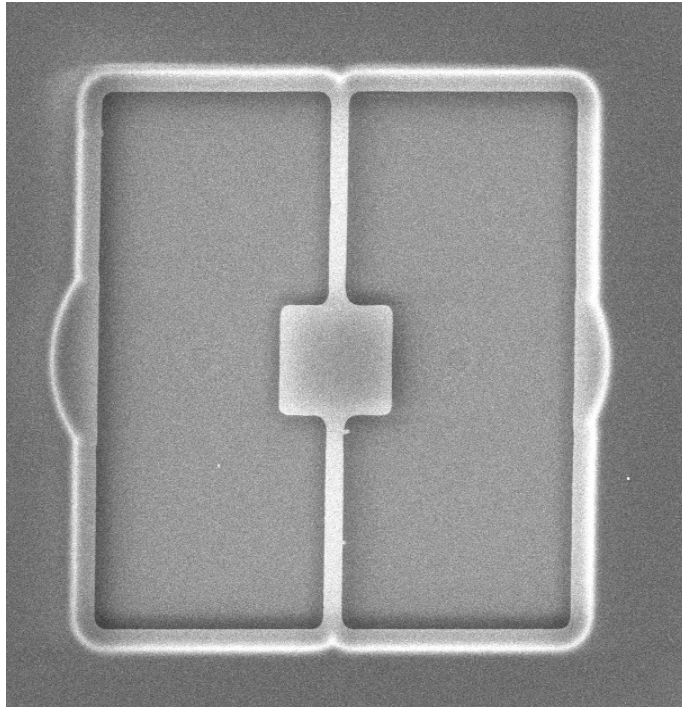


Figure 1-2: Scanning electron image of a doubly clamped, silicon nitride paddle oscillator fabricated using a two step lithography process to minimize overhang undercut.

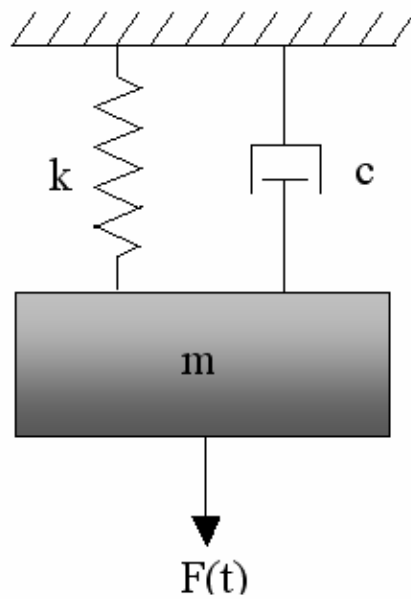


Figure 1-3: Mass – damper – spring system.

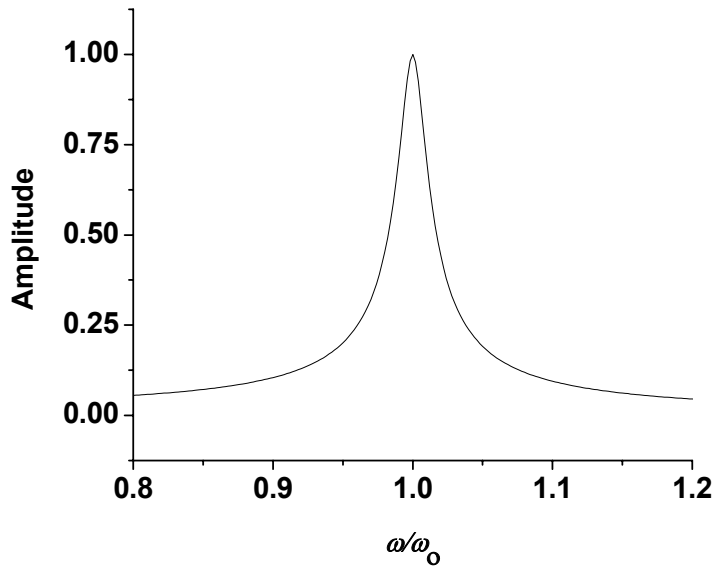


Figure 1-4: Frequency dependent amplitude response of a driven and damped simple-harmonic oscillator ($Q = 50$). Both amplitude and frequency are normalized.

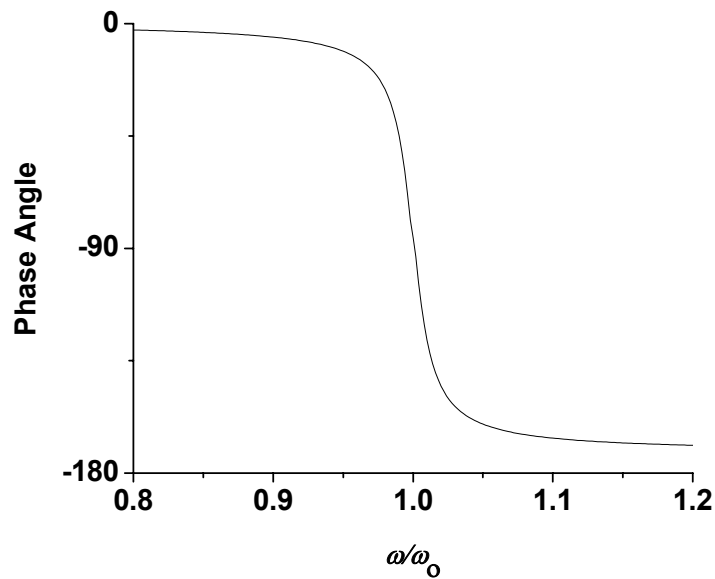


Figure 1-5: Frequency dependent phase response of a driven and damped simple-harmonic oscillator with a ($Q = 50$).

1.5 High Frequency Actuation

1.5.1 Electrostatic

There are four principle methods for transforming electrical energy carried by a voltage signal to mechanical energy in a RF MEMS resonator. Electrostatic actuators, the most common energy conversion method, rely on the force,

$$F = -\frac{1}{2} \frac{Q^2(t)}{C_0 d_0}, \quad 1-11$$

between two charged plates, where Q is the charge on each plate, C_0 is the capacitance and d_0 is the gap distance between the two plates [24, 25]. Many of the first and current MEMS resonators, such as comb drives [26], doubly clamped beams [27], and BAW resonators [28], function through electrostatic actuation. Typically, one plate corresponds to the freely suspended MEMS resonator and the second plate is anchored to the substrate. When a voltage difference is applied across the two plates, the suspended plate will be drawn towards the fixed plate.

The equation of motion follows the form of (1-1) replacing $F(t)$ with an electrostatic driving force,

$$m \frac{d^2x}{dt^2} + c \frac{dx}{dt} + kx = -\frac{1}{2} \frac{Q^2}{\epsilon A}, \quad 1-12$$

where A is the area of the plate and ϵ is the dielectric permittivity. The driving force can be rewritten as

$$\frac{1}{2} \frac{Q^2}{\varepsilon A} = \frac{1}{2} \frac{\varepsilon A V_{in}^2}{(d_0 - x)^2} = \frac{1}{2} \frac{\varepsilon A V_{in}^2}{d_0^2 \left(1 - \frac{x}{d_0}\right)^2} \quad 1-13$$

1-13

Since x/d_0 is a very small quantity, can be linearized using the binomial expansion. Additionally, V_{in} has both an AC and DC component and is written as:

$$V_{in} = V_0 + v_{ac} e^{j\omega t} \quad 1-14$$

Substituting a linearized 1-13 and 1-14 into 1-12 and solving for the x , we find the displacement of the electrostatic resonator behaves as

$$\hat{x}_{ac} = \hat{v}_{ac} \frac{\frac{\varepsilon A V_0}{d_0^2 k'}}{\frac{j\omega}{Q\omega_0} + 1 - \left(\frac{\omega}{\omega_0}\right)^2} \quad 1-15$$

where k' is the DC tunable spring constant,

$$k' = k \left(1 - \frac{\varepsilon A V_0^2}{k d_0^3}\right) \quad 1-16$$

Electrostatic actuation is advantageous in that it is independent of material properties, it is very effective at high frequencies, and the large impedance reduces power consumption. However, there are numerous disadvantages that electrostatic actuation must overcome. Significant nonlinearities (to be discussed more in section 6.2) are inherent to the driving force. Both nanometer sized gaps (which present significant fabrication challenges) as well as large DC voltages (often over 100 volts)

are required to produce sufficient driving forces and detectable motion [29]. Additionally, significant electrostatic fields generated in the transducer can be influenced by outside forces and can couple with the MEMS motion detection mechanism. Finally, due to the capacitive nature of the actuation method, the input impedance is very high. Consequently, in order to interface a MEMS filter with a standard 50Ω network, a lossy and bulky matching network is required if substantial signal reflection from the impedance mismatch is to be avoided.

1.5.2 Piezoelectric

A second commonly used method of electromechanical transduction relies on the piezoelectric effect to convert voltage into displacement. In piezoelectric materials, free carriers are generated when the material is subjected to mechanical stress. Lead zirconate titanate (PZT) and quartz are the most commonly used materials that demonstrate this property. Although piezoelectric actuators are most common to static MEMS sensors, high frequency BAW resonators commonly use a thin film of AlN to produce a driving force. MEMS devices can also be subjected to inertial stimulation by placing samples on a piezoelectric quartz crystal, thus directly coupling the device to mechanical vibrations in the crystal. On the macroscale perspective, quartz crystal oscillators and surface acoustic wave (SAW) filters rely on the piezoelectric effect for transduction. The use of piezoelectric materials in MEMS is limited by sensitivity to film quality and the accuracy of processing parameters, making reliability difficult. In addition, currently no piezoelectric film option exists in standard IC processes, complicating attempts at integration.

1.5.3 Lorentz

A seldom employed but interesting method of actuating a MEMS resonator is through the use of magnetomotive forces [30]. Displacement is induced by sending current through a device placed in a strong magnetic field. According to the Lorentz force law, a force perpendicular to the velocity of the charge and to the magnetic field will be exerted on the device, causing mechanical deflection. Conveniently, detection of the motion is enabled by monitoring the EMF induced along the current path. To its disadvantage, Lorentz force transduction requires large magnetic fields (~ 8 T) and cryogenic temperatures in order to be effective, rendering integration and practical applications impossible.

1.5.4 Thermal

The final method for inducing mechanical motion with an electrical signal is via thermal effects. Commonly, thermal actuation is associated with low frequency or static actuators for use in MEMS structures such as optical switches [31], optical mirrors [32], micro grippers for microassembly [33], MEMS RF switches [34], as well as in some tunable capacitors [35] and inductors. In larger structures, long thermal diffusion time constants limit the effectiveness of this method to low frequency devices. However, as the dimensions of resonators are scaled down to achieve higher frequencies, the thermal diffusion time constants likewise scale, creating a regime where purely thermal excitation can excite high frequency resonant vibrations.

Mechanical displacement can be induced in a MEMS device by bimorph thermal expansion [36], which exists between different types of materials. For example, a mechanical resonator may be fabricated out of a standard semiconductor

material. A second material, most commonly a metal, with a significantly different thermal expansion coefficient, is deposited on top of the semiconductor. Current is passed through the device and Joule heat is dissipated by the internal resistance of the two materials. Since there is a differential expansion coefficient between the top and the bottom film, any expansion in the device will produce out-of-plane deflection. This actuation method has a significant disadvantage for high frequency resonators in that metallization of the structure dramatically increases intrinsic losses, reducing the efficiency of the structure.

In previous research by Keith Aubin [37], high frequency intensity modulation of laser light was employed to excite three-dimensional MEMS structures. This work was significant because it showed that thermally induced stresses in slightly curved silicon or polysilicon structures are able to produce out-of-plane motion without a bimorph effect. Second, it demonstrated that the thermal time constant of some MEMS resonators is short enough to induce MHz mechanical oscillations. This method of actuation, termed optical drive, focuses an internally modulated 417 nm diode laser onto a micromechanical resonator located inside a high vacuum chamber. The approximately $1 \times 1 \mu\text{m}^2$ laser focal volume produces a local temperature gradient, causing thermal expansion, that in turn generates a stress profile within the membrane. In a perfectly flat device, a stress gradient will cause virtually no out-of-plane deflection; however, for a membrane with a slight degree curvature, stress generated in the device layer will be relieved through out-of-plane deflection.

The process of heat diffusion out of the resonator can be modeled by a one dimensional heat equation,

$$u_n(r, t) = B_n \sin\left(\frac{n\pi r}{R}\right) e^{-\lambda_n t} \quad 1-17$$

with time constant,

$$\lambda_n = \frac{K}{C\rho} \left(\frac{n\pi}{R} \right)^2 \quad 1-18$$

where κ is the thermal conductivity, c is the heat capacity, R is the radius of a 2D plate, and $n = 2.4$ is the root of a Bessel function $J_0(\mu_i^{(0)})=0$. Due to the micron-size radius of the device, the cooling rate, $1/\lambda_n$, is on the order of microseconds, allowing high frequency modulation of the dissipated power to excite standing wave resonant vibrations in the micromechanical structure.

1.6 High Frequency Detection

1.6.1 Electrostatic

One of the most common methods for detecting the mechanical motion of a MEMS device is by monitoring the capacitive characteristics of the electromechanical resonator. A micromechanical resonator can be configured to have a capacitive output port, i.e. the resonator membrane forms one non-stationary side of the capacitor and the substrate or adjacent structure forms the static side of the capacitive output port. The current flowing through the MEMS capacitor is

$$i = \frac{dQ}{dt} \quad 1-19$$

Since at resonance the gap is varying with time, equation 1-19 becomes

$$i = V_o \frac{d(CV)}{dt} \quad 1-20$$

which, following the notation of (1-13, 1-14) and again linearizing x/d_0 , can be written as

$$i = \frac{d\left(\frac{\varepsilon A}{d_0 - x}(V_0 + v_{ac})\right)}{dt} = \frac{d\left(\frac{\varepsilon A}{d_0}\left(1 + \frac{x}{d_0}\right)(V_0 + v_{ac})\right)}{dt} \quad 1-21$$

Thus, by measuring the displacement current produced by the vibrating resonator, the characteristics of the mechanical motion can be determined. When monitoring the current, the MEMS resonator can be viewed as a two-port system where vibrations are induced and measured on separate actuators. Like the electrostatic actuator, displacement current detection has disadvantages due to its capacitive (high impedance) nature, its susceptibility to electrostatic cross-talk, its nonlinear dependence on d_0 , and the necessity for small gaps.

The electrostatic MEMS resonator can also be implemented as a one-port system, where motion is both induced and sensed with the same capacitive transducer. Substituting x from (1-15) into (1-21) and solving for the impedance, $Z(\omega)=v/i$, we find

$$Z(\omega) = \frac{\omega^2 - j\omega\frac{\omega_o}{Q} - \omega_o^2}{j\omega C_0\left(\omega^2 - j\omega\frac{\omega_o}{Q} + \omega_{AR}^2\right)} \quad 1-22$$

where ω_o is the resonant frequency and ω_{AR} is defined as the antiresonant frequency with $\omega_{AR}^2 = \omega_o^2 \left(1 + \left(\frac{\varepsilon A V_o}{g_o^2} \right)^2 \frac{1}{k' C_o} \right)$. Depending on the frequency of stimulation, the impedance of the actuator will vary, enabling detection of the resonant motion. Equation 1-22 is plotted in figure 1-6 where ω_o and ω_{AR} are located at the minimum and maximum points. This one port method has numerous disadvantages [38] in addition to the previously mentioned electrostatic hysteresis. First, a transresistance circuit is required in order to detect the output signal. Second, the presence of ω_{AR} distorts the measured signal and by shifting the resonance alters the passband and complicates the measurement process.

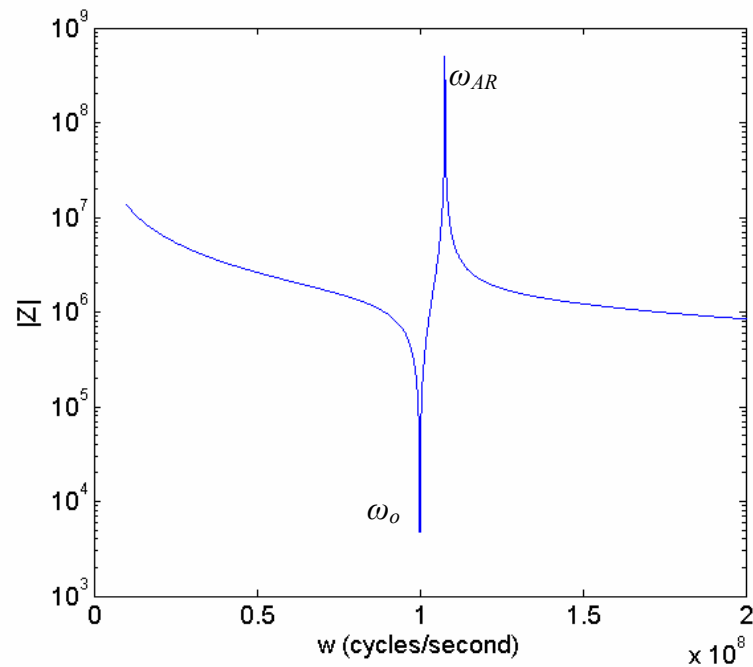


Figure 1-6: Calculated input impedance for an electrostatic transducer covering half of a 30 μm dome resonator. Gap spacing is 200 nm.

1.6.2 Interferometric Detection

High-speed optical sensing of micromechanical motion has been previously demonstrated and developed by Carr [39]. The resonators used in this thesis are similar to previous optically detected resonators in that they are suspended over a substrate wafer. The resulting cavity created by the air gap separating the membrane from the wafer forms a Fabry Perot cavity. Incident light will establish a standing wave interference pattern based on the film stack parameters. The theory to predict the intensity of the reflected, adsorbed, and transmitted wave has been well established, but a particularly eloquent summary can be found in the thesis of Keith Aubin [37]. Figure 1-7 displays the theoretically predicted interference pattern produced by the dome cavity in response to a 633 nm HeNe CW laser focused onto the surface of the membrane. We chose the thickness of the sacrificial oxide based on the maximum of the derivative of the reflected light pattern. Any change in the sacrificial gap (i.e. resonator vibrations) will be translated to the intensity of the reflected signal. The amplitude modulated light reflected from the device surface is then detected by a high speed New Focus 1601 1 GHz bandwidth photodetector. With this method, fluctuations in the voltage output signal from the photodetector are a representation of the resonator's mechanical vibrational amplitude.

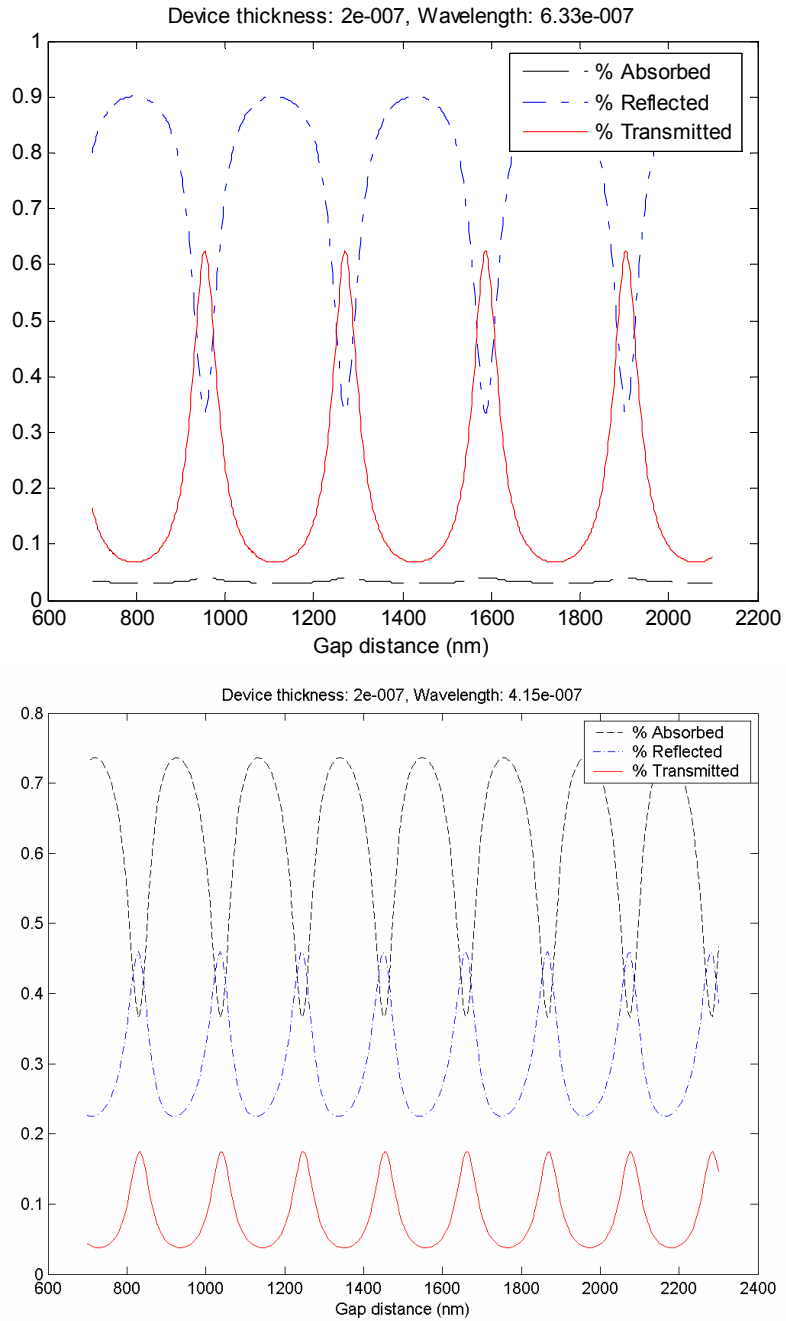


Figure 1-7: Calculated normalized reflection pattern for both 633 nm HeNe red laser and 415 nm diode blue laser produced by a film stack of 200 nm thick polysilicon over an air gap, all over a silicon wafer.

1.6.3 Piezoresistive Detection

Another common way of detecting the motion of integrated sensors is to use the piezoresistive effect, present in many semiconductors and metals, to transduce mechanical deformation. Piezoresistive sensors have been commonly employed in MEMS strain gauges such as accelerometers [40] and pressure torque or displacement sensors [41]. Piezoresistive cantilevers have also been used in place of conventional optical measurement techniques for Atomic Force Microscopy (AFM) applications [42] to measure the low-frequency resonant motion of a cantilever.

Piezoresistivity is the linear coupling of mechanical stress and electrical resistivity that is seen in semiconducting materials such as silicon, germanium, diamond and some thin-film metals. It is quantified as a change in the ratio of an electric field component to a current density component in the same direction [43]. The effect can be described completely by a set of equations relating the electric field (E), current density, (i) and stress components (T) in each crystallographic direction. When considering a single dimension (l) a simplified expression can be used:

$$\frac{E}{R} = i(1 + G T) \quad 1-23$$

where R is the material resistivity under zero stress, E/i is the resistivity under tension $T = \Delta l / l$, and G is the piezoresistive coefficient. Thus

$$\frac{E}{i} = R + \Delta R \quad 1-24$$

and through 1-23 and 1-24 we find that the piezoresistive coefficient relates the fractional change in resistivity to the fractional change in elongation.

$$\frac{\Delta R}{R} = G \frac{\Delta l}{l} \quad 1-25$$

The constant, G , commonly called the gauge factor, is an intrinsic property of a material and is dependent on crystallographic orientation.

Piezoresistive detection has also been used for measurement of high frequency resonant motion [44]; however, experiments were performed using heterodyne detection, where the transducer mixed the output RF voltage to DC. The magnitude of the DC output voltage is then a relative indicator of the maximum resonant amplitude. This method removes frequency information from the output signal, which reduces parasitic effects; however it makes feedback and filtering systems nearly impossible to implement.

2 The Shell-Type, High Frequency, Micromechanical Resonator

The majority of this thesis is devoted to a new, self-aligning, MEMS geometry which has been termed the “dome resonator”. The dome resonator is unique because it is created using a very simple fabrication process, lending its usefulness to IC-MEMS integration while maintaining high performance characterized by a high resonant frequency, low damping, and small nonlinear effects.

2.1 Fabrication

The dome shaped resonator takes form on a polysilicon-on-insulator wafer (figure 2-1 a). A utility grade 100 mm single side polished silicon wafer is used as the structural base of the device. Next, a film of either LPCVD SiO₂ or PECVD SiO₂ is deposited on the wafer. Wet LPCVD SiO₂ is the preferred method since it is much more dense, and therefore suitable for subsequent high temperature processing. The thickness of this film is not critical for the operation of the dome resonator, although it should be larger than the maximum resonator deflection (less than 10 nm) and, if using interferometric detection, should be tuned to achieve maximum signal reflection. A thickness of approximately 1.5 μm was used for the majority of this research. The final deposition step is a high quality LPCVD polysilicon film used to form the mechanical resonator. The film is deposited at 570 °C at a pressure of 150 mTorr with 150 sccm SiH₄ gas mixture. Initially this process yields an amorphous silicon film which can have significant tensile stress. Deposition rates for this process are on average 3 nm/min, which, for a commonly used 200 nm thick film, means a SiH₄ gas flow time of 70 min. Immediately following the amorphous silicon film deposition, a high temperature anneal in a N₂ environment forms grains in the silicon film and

diminishes the film stress. Removing the wafers after a one hour anneal results in a virtually stress-free polysilicon film. An anneal time of 1.5 hours produces a film with significant compressive stress. After annealing the wafer for 1.5 hours at 1150° C, the 200 nm polysilicon film is measured using a Flexus F2320 to have a compressive stress of ~300 MPa, calculated from the change in the curvature of the wafer due to the presence of the polysilicon film on one side.

To define the central hole of the dome resonator, a basic 1-step lithography process is used (figure 2-1 b). The wafer is first primed with either HMDS vapor or spin on P-20. Next, a g-line (436 nm) sensitive resist such as Shipley 1813 or an i-line (365 nm) resist such as OIR 620.07 or SPM955-0.7 is spun on the wafer to a thickness between 0.5 μm and 1 μm and then softbaked at 115 °C for 90 seconds. Photolithography is performed using an i-line GCA Autostep AS200. A detailed description of the Autostep program is given in Appendix A. Following exposure, the wafer is again baked at 115 °C for 90 seconds and then developed using MIF-300 either manually or with an automated Hamatech wafer handler for 60 to 90 seconds.

Defining the 2-3 μm diameter “etch hole” in the polysilicon device layer permits a wet chemical etchant to access the underlying sacrificial oxide. Following resist lithography, a reactive ion etch is used to selectively remove the exposed polysilicon from the hole. Two plasma chemistries can be used at this point. A chlorine based plasma in a Plasma-Therm 720 allows high selectivity to the photoresist mask as well as to the oxide underneath the poly. When the PT720 is not operational, an anisotropic silicon etch using CF_4 plasma in a Plasma-Therm 72 is used, which is slower and much less selective to oxide and photoresist. Following definition of the etch hole, the photoresist is stripped from the wafer in a heated Shipley 1165 resist bath.

The final step in fabrication of the dome resonator is removal of the oxide below the polysilicon film with a hydrofluoric acid etch. For example, to create a 30 μm diameter dome, the wafer is dipped in a 49% hydrofluoric acid bath for 10 minutes. This removes the oxide in a radial direction from the etch hole, leaving a suspended circular membrane. Although this is the quickest method, using buffered oxide etch instead of 49% HF will result in a more controlled and precise radial etch. The wafer is moved from the HF bath, to a water bath, then directly to an ethanol bath. Ethanol has much lower surface energy, preventing unintentional adhesion (stiction) between the membrane and the substrate due to capillary forces and surface tension.

The final suspended dome resonator is shown in figure 2-2. The resulting membrane has non-zero curvature due to the large compressive stress incorporated into the device layer through the high temperature annealing process. When the sacrificial silicon dioxide is released through the etch hole, the in-plane poly film stress produces out-of-plane buckling, forming a shallow shell. The vertical projection can be estimated by counting the interferometric Newton rings as seen in figure 2-2 b. A 200 nm thick membrane, 30 μm in diameter with 300 MPa of compressive film stress projects approximately 1 μm out-of-plane at the apex of the dome.

The out-of-plane component in the curvature significantly increases the resonant frequency over a two dimensional structure. The natural frequency of a flat annulus clamped on the periphery and free in the center is predicted [45] to be

$$f_{mn} \Big|_{\text{flat plate}} = \frac{\pi h}{2R^2} \sqrt{\frac{E}{3\rho(1-\nu^2)}} (\beta_{mn})^2, \quad 2-1$$

where h is the polysilicon thickness, R is the in-plane radial projection of the plate, E is Young's modulus, ρ is the material density, ν is Poisson's Ratio, and β is a

geometrical constant. Shallow shell theory [46] is used to derive 2-2, which accounts for the extra rigidity provided by the dome's out of plain projection

$$f_{mn} \Big|_{\substack{\text{shallow} \\ \text{spherical} \\ \text{shell}}} = \left(f_{mn}^2 \Big|_{\text{flat plate}} + \frac{E}{\rho(2\pi\chi)^2} \right)^{1/2}, \quad 2-2$$

where χ is the radius of curvature of the dome. The increased stiffness allows large diameter structures to achieve significantly higher frequencies. Simulation results are shown in figure 2-3, illustrating the effect of radial projection and curvature on the resonant frequency of a shallow shell. As evident in the plot, very high frequencies can be achieved by simultaneously increasing the vertical projection and decreasing the lateral dimension.

The experimental frequency spectrum of the aforementioned 30 μm diameter dome is pictured in figure 2-4. Multiple modes of the resonator, ranging between 8 and 26 MHz, are easily excited in the shell membrane. Both numerical simulations and experiments were performed to characterize the shape of the resonant modes. A simulation using ANSYS is pictured in figure 2-5 showing the first 6 modes of the resonator. The resonant modes are discriminated by the number of radial and circumferential nodes in the membrane standing wave. Modes with only radial nodal lines (e.g. γ_{02}) are referred to as axisymmetric modes, and modes with both circumferential and radial nodal lines (e.g. γ_{21}) are non-axisymmetric modes. The modes of vibration were also experimentally characterized based on the relative phase and amplitude of the membrane displacement. Figure 2-6 shows three resonant modes of the 30 μm diameter dome at 10, 14 and 17 MHz. The MEMS resonator is subjected to resistive stimulation to provide stable excitation. The response of the membrane is then systematically sampled by rastering a 1 x 1 μm^2 pixel size interferometric

detection method across the surface. The relative phase and amplitude of motion can then be reconstructed in a 3D plot. Both the 12.7 and 14.7 MHz modes are γ_{0x} axisymmetric modes, having no circumferential nodes. The phase picture indicates that this is a high order mode with multiple radial nodes; however, the interferometric detection method is sensitive to the membrane curvature, producing artificial phase inversions in the radial direction. Thus it is impossible to experimentally tell how many circumferential nodes are present. The 17.7 MHz mode is an example of a mixed mode.

Inevitable fabrication irregularities across the surface of a wafer result in variations on the order of 0.1% in the frequency of dome resonators. Nonuniformities are produced from variations in the local film stress, film thickness, release etch timing, and photolithography process, as well as from polysilicon material defects. Such variations should be addressed before undertaking high-volume manufacturing; however, most of these parameters can be precisely controlled with precision manufacturing tools. Additionally, individual resonator tuning can be enabled by controlling the stress state of the membrane, which will be discussed in section 5.6.

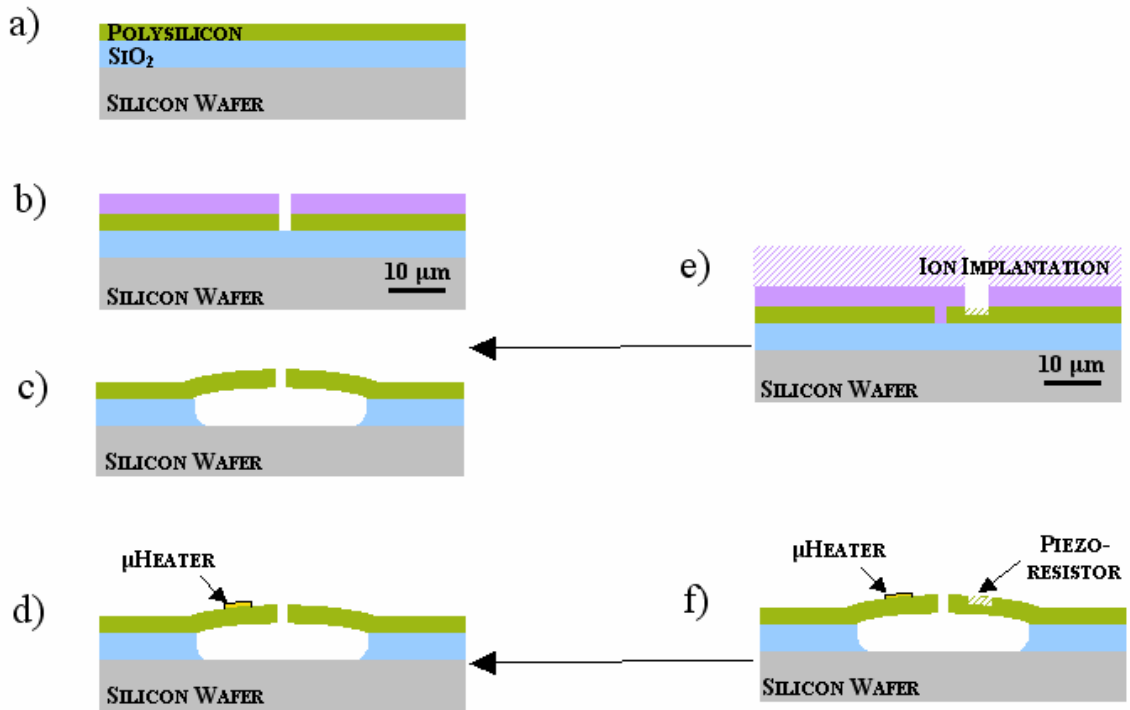


Figure 2-1 a-d): Diagram displaying fabrication process to make dome resonator and resistive actuator. e,f) illustrates fabrication modifications to incorporate an implanted piezoresistor which can be utilized for either driving or detection.

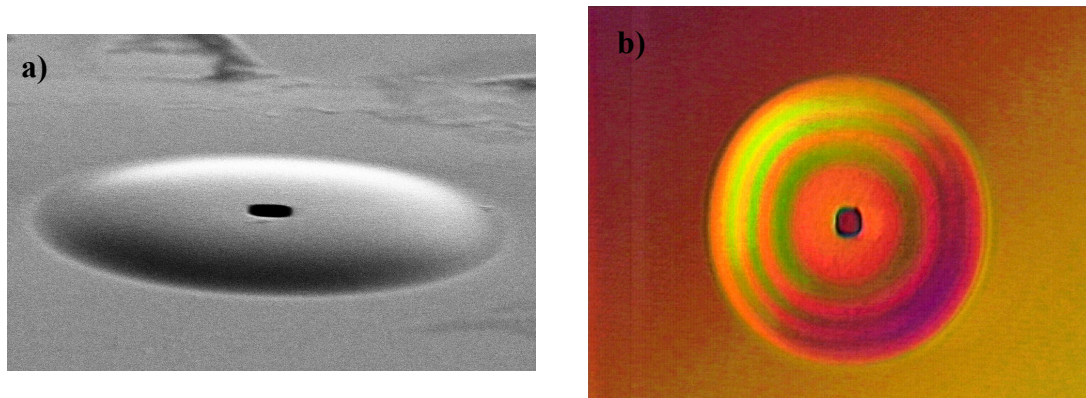


Figure 2-2 a): SEM image of a 30 μm diameter shell type resonator. Image taken at a 45° angle to illustrate curvature. b) Optical micrograph of similar resonator. Newton interference rings spaced at $\lambda/2$ provide an estimate of 1 μm vertical projection.

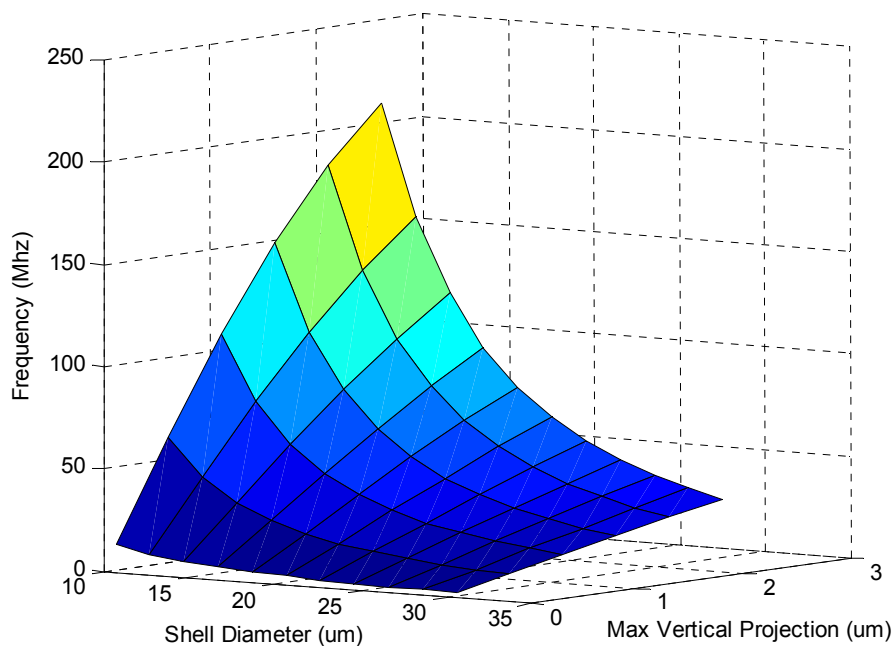


Figure 2-3: Numerical calculation of resonant frequency dependence on membrane diameter and curvature. Young's modulus (E) = 150×10^9 Pascal, film thickness (h) = 200×10^{-9} m, density (ρ) = 2328 kg/m^3 , Poisson's ratio (ν) = 0.22.

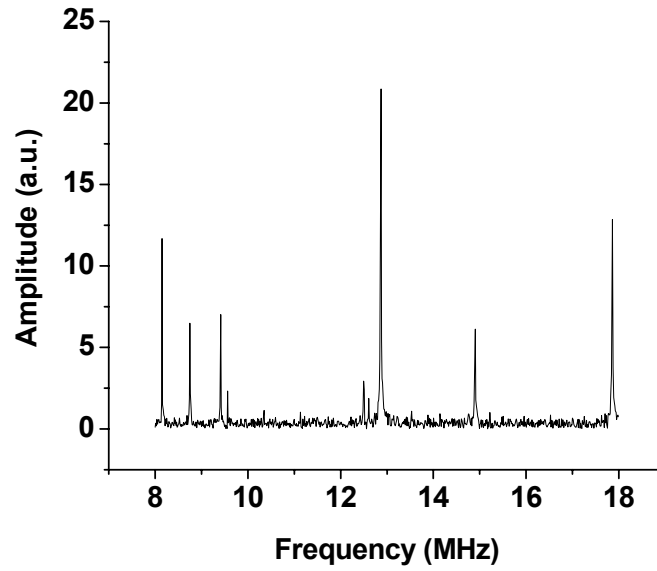


Figure 2-4: Experimental frequency spectrum of a 30 μm diameter dome resonator, illustrating its multiple modes of vibration. Resonator excited by resistor and detected by interferometer. Spectrum could be viewed as a fingerprint [58], (i.e. identification mechanism) which, due to fabrication variances and high Q -factor, will be unique for each device.

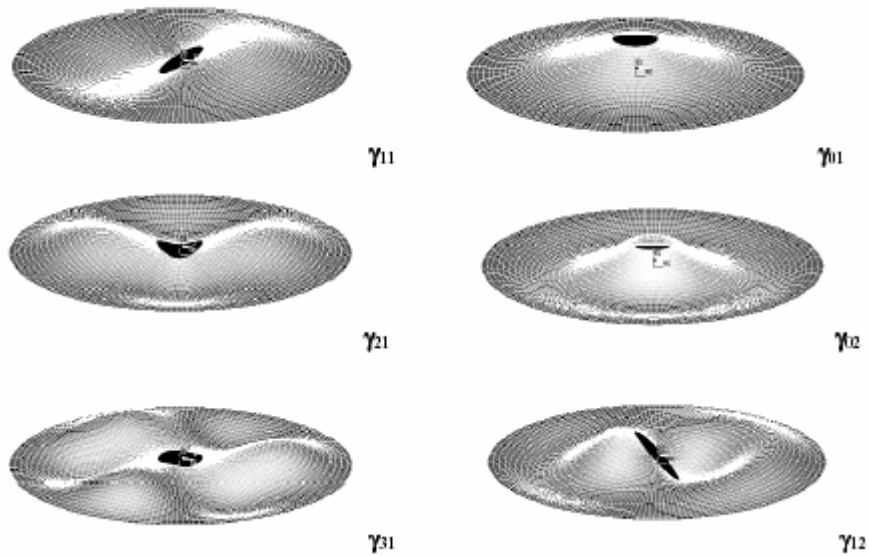


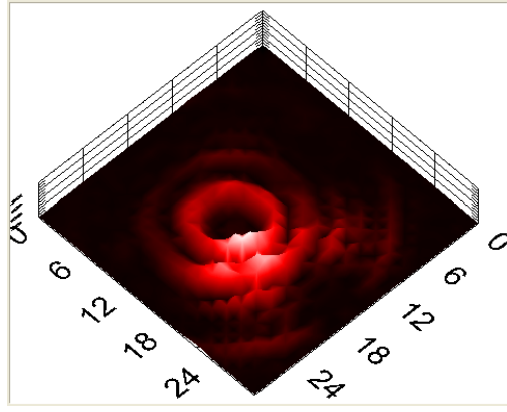
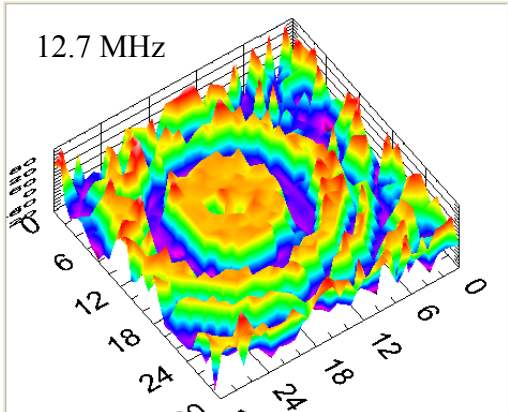
Figure 2-5: ANSYS FEM model of first 6 mode shapes of dome resonator. Reproduced from [47].

PHASE

AMPLITUDE

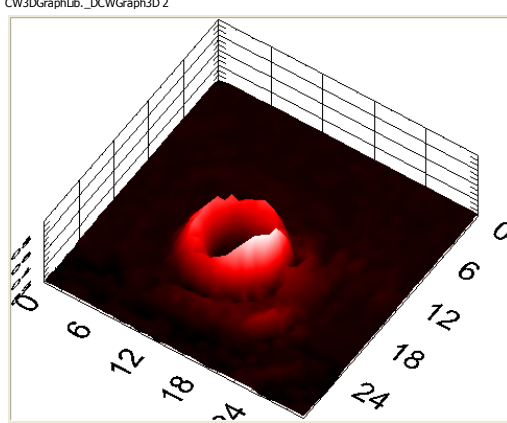
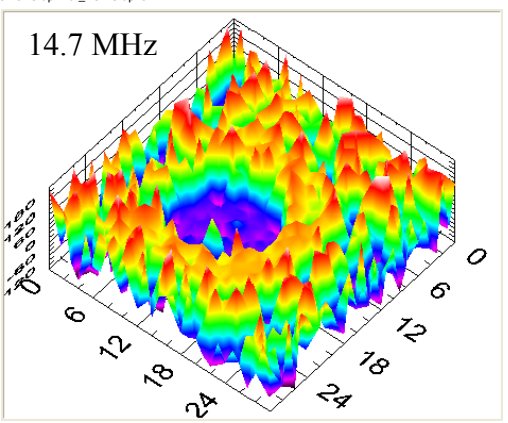
CW3DGraphLib._DCWGraph3D

CW3DGraphLib._DCWGraph3D 2



CW3DGraphLib._DCWGraph3D

CW3DGraphLib._DCWGraph3D 2



CW3DGraphLib._DCWGraph3D

CW3DGraphLib._DCWGraph3D 2

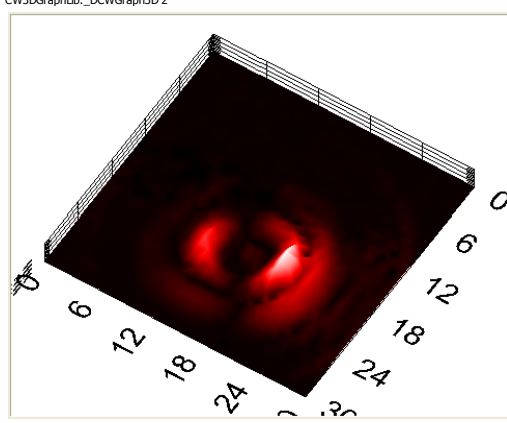
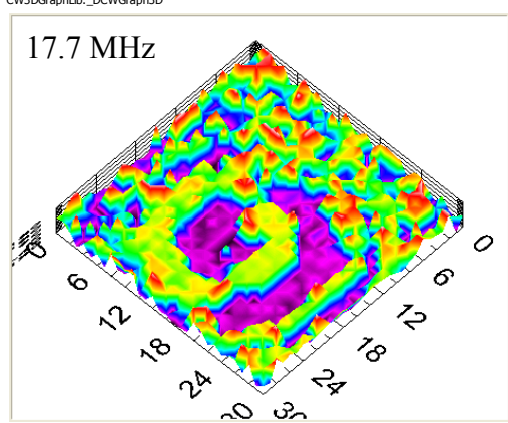


Figure 2-6: Experimental mode shapes of 12.7, 14.7, 17.8 MHz modes in dome resonator. The membrane is excited with a metallic resistor. Interferometric detection method is rastered across the surface to for 2D map of amplitude and phase.

2.2 Higher Frequencies

A significant advantage of MEMS systems is that by scaling down the geometry of the mechanical resonators and hence, scaling the mass of the resonant system, the resonant frequency can be increased. This allows mechanical signal processing to be performed in a wide variety of established communication bands. For example, MEMS resonators could be scaled in size to serve bands such as 900 or 1900 MHz used by PCS cellular phones, 125 KHz, 13.56 MHz, and 900 MHz bands allocated for radio frequency identification (RFID) tags, or 88-108 MHz for FM radio.

To reach higher frequencies than those provided by the aforementioned 30 μm device, we scale both the lateral dimension as well as the vertical projection of the shell. Scaling the projection of the resonator corresponds to decreasing R in equation 2-1 and 2-2. A 3 μm diameter device was fabricated and exhibited a fundamental frequency at 260 MHz with a Q of 2,500. A higher order mode of vibration at 460 MHz (figure 2-7) was also detected in this resonator. Dramatic scaling into the nanometer size scale presented numerous difficulties. Small vertical displacements coupled with a diminished physical size makes motion detection impossible given the sensitivity of our current method of detection.

The other approach for scaling the frequency is to increase the curvature of the resonator, in turn increasing the stiffness. Figure 2-8 numerically demonstrates how, by scaling curvature up to that of a hemisphere, the resonant frequency can be enhanced while preserving the footprint and thus the “detectability” of a structure. Figure 2-10 illustrates one concept for producing a hemispherical resonator. A hemispherical preform is made by placing a glass microsphere into a hole etched in the substrate. The wafer is then coated with a PECVD polysilicon film to form an effective substrate that can withstand HF acid. A sacrificial layer of SiO_2 is deposited

over the wafer followed by a structural layer of polysilicon. The SiO_2 was then removed through an etch hole to form the suspended, curved membrane (figure 2-10). Unfortunately, interferometric detection could not detect motion in the convex curved structure. One possible explanation is that the spring constant was increased to the extent that resonant motion was undetectable. Additionally, the curved surface tended to deflect and disperse focused laser light, creating complications in detecting the modulation that is superimposed on the reflected beam. Future designs should focus on a concave structure which would dip into the surface rather than project out from surface. This alternative would create a lensing effect for the incident light beam rather than deflecting the beam. Our standard method of interferometric detection is obviously not the optimal method and should be replaced by capacitive or piezoresistive detection.

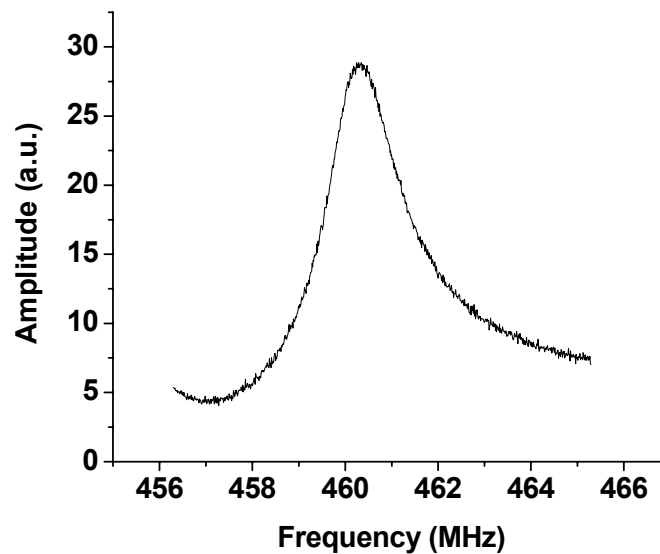


Figure 2-7: Experimental response from a $3\ \mu\text{m}$ diameter flat membrane: Fundamental mode at 260 MHz with a $Q = 2,500$, highest detectable mode at 460 MHz

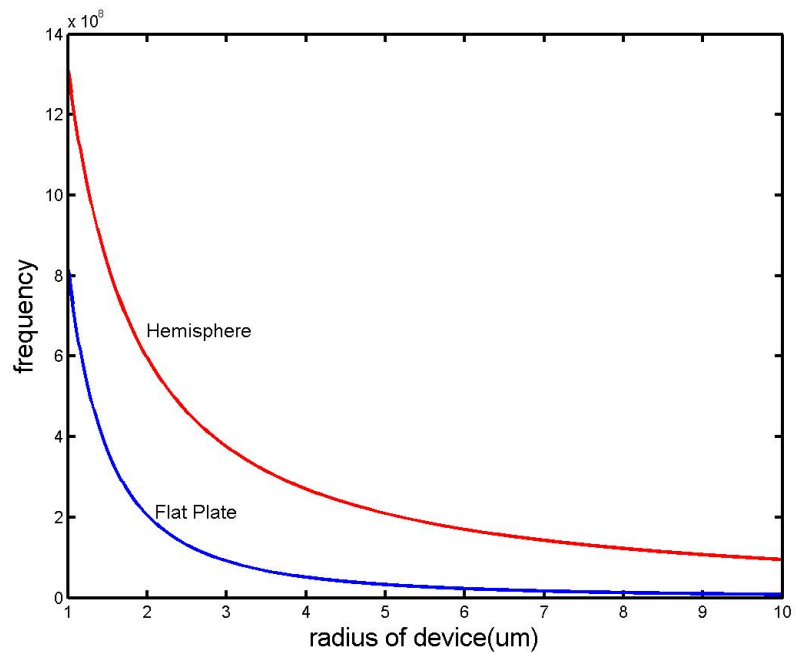


Figure 2-8: The frequency advantage provided by hemispherical curvature. Simulation parameters given in figure 2-3.

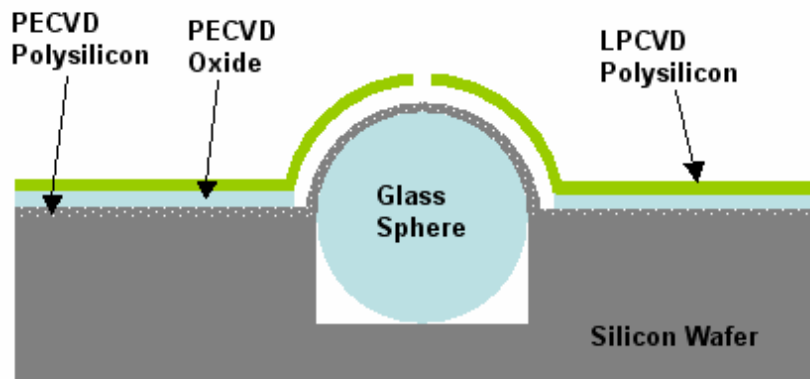


Figure 2-9: Fabrication process for the hemispherical resonator picture in figure 15.

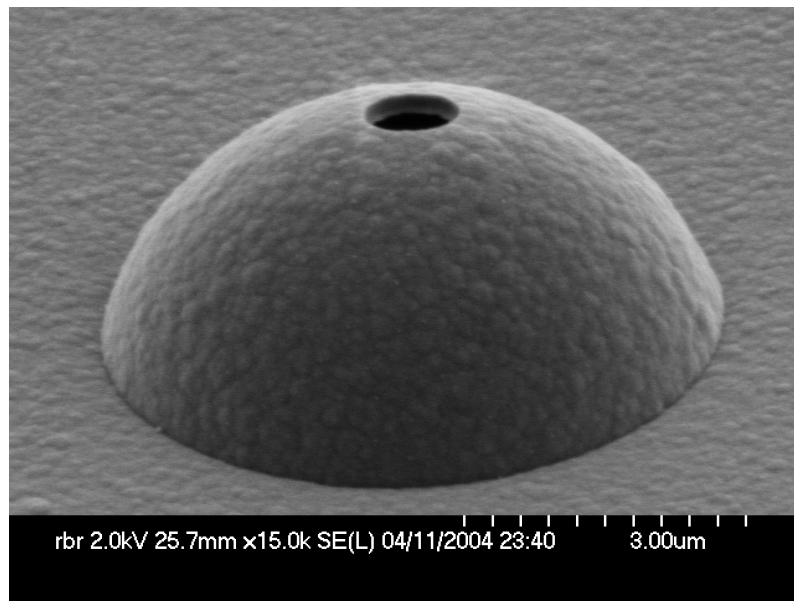


Figure 2-10: SEM image of hemispherical polysilicon resonator fabricated using $2.5 \mu\text{m}$ diameter glass sphere preforms.

2.3 Damping

Another significant advantage of using microscaled silicon resonators is the very high quality factors (Q) that can be achieved. The Q of the resonator is measured as $f_o/\Delta f$, where Δf is the full width at half maximum power of the Lorentzian response and f_o is the center frequency of the response. From an energy perspective, Q is $E/\Delta E$ where E is the stored vibrational energy and ΔE is the energy lost per cycle of vibration. The Q of the 30 μm dome's 12.7 MHz mode was measured to be 5,000, the 14.7 MHz was 3,700 and the 17.76 MHz was 15,000. For comparison, the Q of an on-chip LC tank circuit would be about 10 to 100 due to substantial electrical resistance and parasitic capacitive effects. For RF applications, the Q of the filter is one of the most important characteristics, governing the selectivity of the element and the ability to suppress signals outside of the frequency band of interest. Additionally, since the amplitude on resonance is increased by the Q of the resonator, a higher Q will reduce the power consumption and improve the conversion loss of the system.

All experiments on the dome resonator were performed in a custom built vacuum chamber at a pressure of 10^{-6} Torr, thus eliminating viscous damping effects that would substantially increase losses in the mechanical system. For a resonator operating in vacuum, vibrational energy is dissipated through several mechanisms [48]. Losses are experienced through mechanical dissipation such as acoustic coupling to the support structure (clamping loss), through intrinsic internal friction primarily dominated by thermoelastic dissipation (TED) [49], and through extrinsic crystallographic defects and disorder in the film [50].

TED is generally contributed to heat flow between regions of alternating stress, causing power dissipation. It is most pronounced when the period of cyclic stress is

comparable to the thermal time constant of the heat flow. The magnitude of this damping has been previously characterized [50, 52] for cantilever beams as:

$$\delta = \frac{1}{2Q} = \Gamma(T)\Omega(f) \quad 2-3$$

with

$$\Gamma(T) = \frac{\alpha^2 TE}{4\rho C_p} \quad \text{and} \quad \Omega(f) = \frac{2f / F_0}{1 + (f / F_0)^2} \quad 2-4$$

where

$$F_0 = \frac{\pi\kappa}{2\rho C_p t^2} \quad 2-5$$

Here α is the coefficient of thermal expansion, c_p is the specific heat capacity, and T is the temperature. Since there is no width dependence in (2-3), it may be a reasonable assumption that a dome is essentially a wide cantilever and TED losses would be on the same order of magnitude. From equation (2-3) the Q factor limited by TED losses is approximately 3.5×10^5 , an order magnitude higher than the Q s obtained experimentally – indicating that dissipation in the dome is not primarily dominated by internal friction.

One disadvantage of the dome shaped resonator design is that uniform clamping around the periphery may be a significant source of energy loss. Although the as-fabricated dome had similar Q factors to mushroom resonators of similar dimensions, the intrinsic Q of the mushroom was limited by crystallographic defects

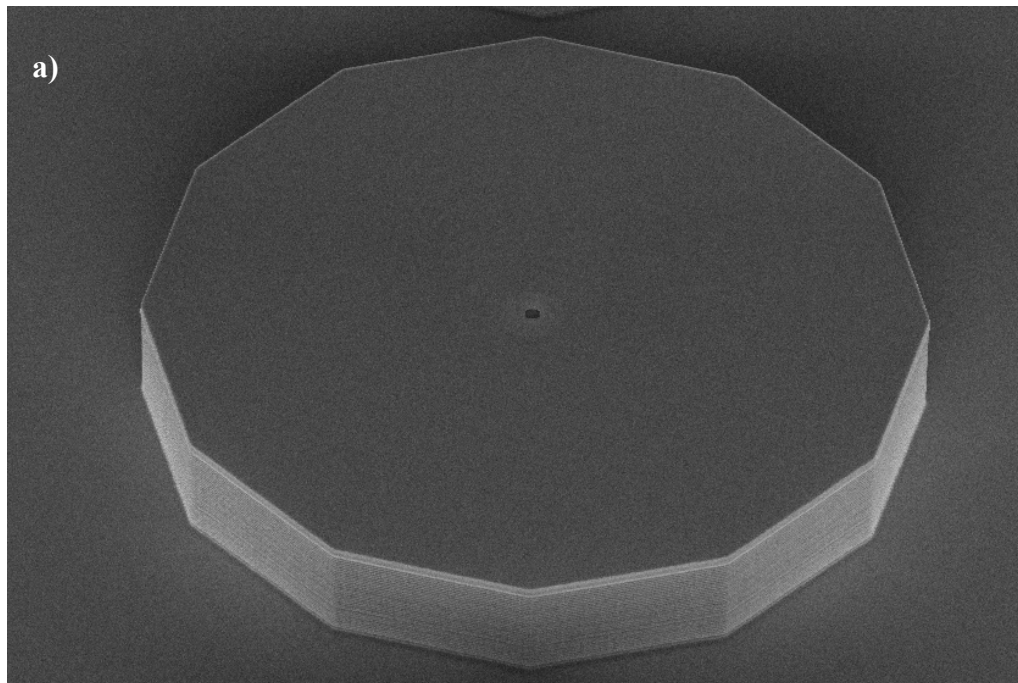
and surface dissipation [13]. Due to the small area of clamping in the mushrooms, Q s on the order of 10^5 could be attained through laser annealing treatments. Analytical simulations performed on the dome resonators, however, determined that surface acoustic waves produced from the mechanical motion and carried to the substrate were the most significant source of energy loss [53]. In fact, anchor coupling losses increase exponentially with increasing frequency. Simulations which modeled both surface and bulk acoustic waves being perfectly transmitted from the resonator to the surrounding film produced a Q of 2,600 for a 14.5 MHz mode and a Q of 2,267 for a 19.1 MHz mode in a $30\ \mu\text{m}$ dome. These Q s were about 50 % lower than Q s obtained experimentally for similar modes indicating that the substrate may not be a perfectly absorbing boundary; however this substantiates the claim that losses in the dome resonators are clearly dominated by clamping losses.

One way to reduce effect of clamping losses and improve the dome Q is to focus acoustic energy back into the resonator by designing a reflecting mesa surrounding the dome. The surface acoustic wave is reflected from the abrupt change in impedance between the semiconductor and the air gap and will form either a constructive or destructive interference pattern. Simulations indicate that a mesa surrounding the resonator at a distance of $0.25\ \lambda$, $1.25\ \lambda$, and $1.75\ \lambda$ will form a constructive interference pattern, which traps energy inside the system and improves the Q by several factors.

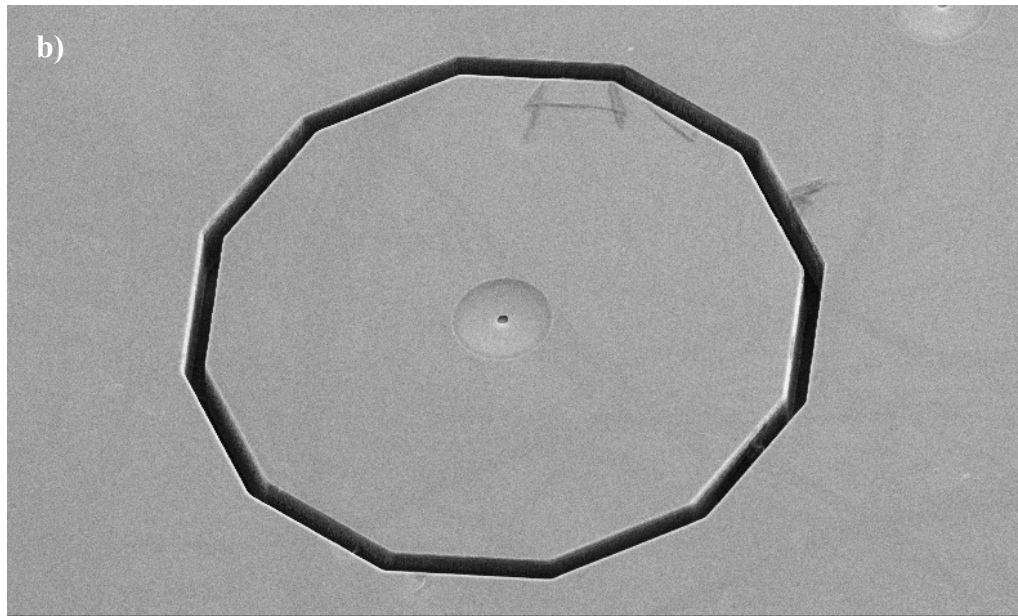
Figure 2-11 illustrates two mesa-isolated domes, one with an infinite width trench and one with a finite width trench. The outlines of the trenches are defined in a second step of photolithography after the dome resonator is released. Once the resist is developed, a short Bosch silicon ICP etch is used to penetrate the device layer, followed by a ICP oxide etch and finally a longer Bosch silicon etch to excavate approximately $13\ \mu\text{m}$ into the silicon substrate. The experimental results and

theoretical predictions for the 104 MHz mode of a 5.3 μm diameter mesa dome are seen in figure 2-12. Multiple-sized mesas were tested which, for a given mode of oscillation and SAW wavelength, will form different interference patterns. A periodic pattern can be clearly seen where there are Q improvements at 0.75, 1.25, 1.75 $R_{\text{mesa}}/\lambda_{\text{SAW}}$.

When the mechanical resonators are not operated in a vacuum of less than several mTorr, air damping becomes the ultimate limiting factor. Viscous drag and possible squeeze film damping between the resonator and the substrate reduce the Q by several orders of magnitude. Figure 2-13 demonstrates 14 MHz resonant vibrations with a $Q < 100$ for a 30 μm dome in atmosphere.



WD = 10 mm Aperture Size = 30.00 μm Signal A = InLens Date : 13 Apr 2006
Mag = 1.67 K X EHT = 8.00 kV Pixel Size = 211.2 nm Signal B = InLens Time : 18:50:44



WD = 14 mm Aperture Size = 60.00 μm Signal A = SE2 Date : 10 Apr :
Mag = 764 X EHT = 10.00 kV Pixel Size = 455.9 nm Signal B = SE2 Time : 22:58:1

Figure 2-11: Dome mesa built to reflect acoustic wave energy back into resonator structure.

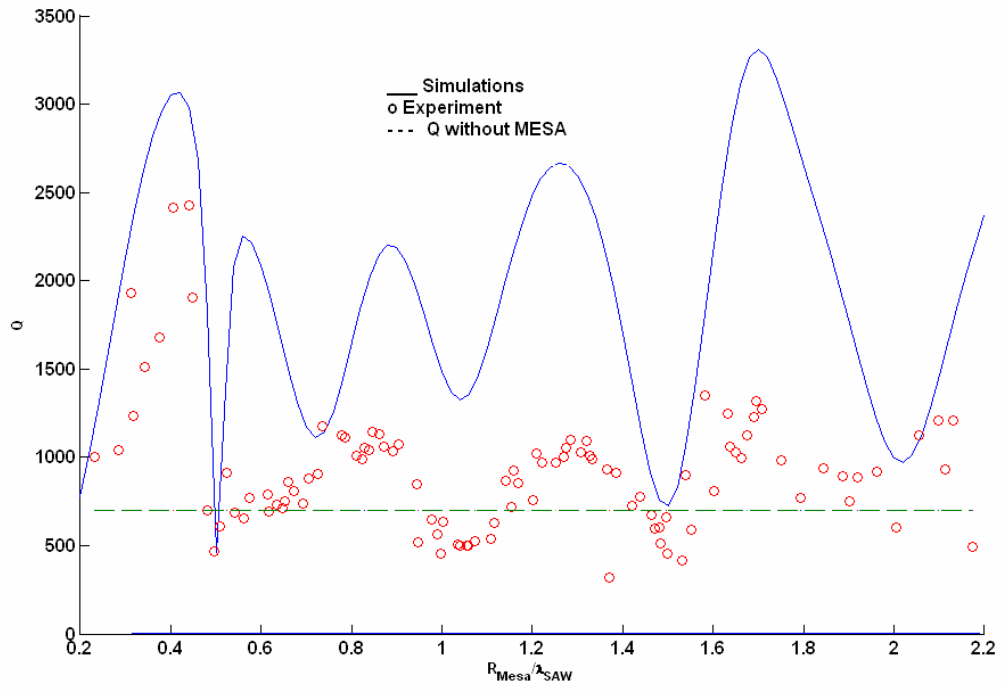


Figure 2-12: Simulation and experimental data from mesa dome.

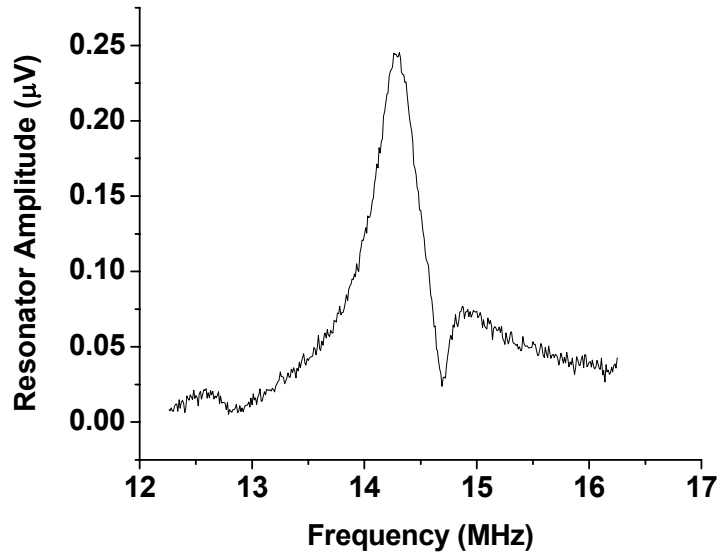


Figure 2-13: Resonance of 30 μm diameter dome resonator at atmospheric pressure.

3 Integrated Resistive Transduction

Transduction, the process of converting an electrical signal to mechanical motion and mechanical motion back to an electrical signal, is one of the most challenging aspects of RF MEMS. As previously discussed, thermal actuation is a highly effective energy conversion mechanism. This section focuses on the integration of thermal drive and piezoresistive detection into the dome shaped resonators, in essence, leading to resistive coupling into and out of the microresonator. Resistive coupling offers several advantages over electrostatic transduction: the actuators are broadband and can be impedance matched to the network, their performance does not depend on nanometer scaled gaps surrounding the resonator, and the impact on the resonator quality factor is minimized. Finally, both resistive transducers can be fabricated within the polysilicon membrane allowing a resonator to be implemented into a single plane of silicon and defined immediately next to a field effect transistor in a CMOS processes.

3.1 Resistive Actuation

Previous methods for performing high frequency thermal actuation made use of intensity modulated lasers that were focused onto the MEMS device. While this was an excellent tool for experimental analysis of any device on a wafer, it is hardly a compact method of transduction. Additionally, the long path distance (often several feet) between the laser source and the MEMS device translates any vibrational instability of the optics into frequency and amplitude noise in the resonator, complicating reproduction of sensitive measurements.

An alternative method for locally dissipating heat into a microresonator is to locate a microheater in direct proximity to the resonant membrane. Figure 3-1 pictures a thin film metallic resistor which has been lithographically defined on the surface of the resonator. By applying a voltage across the microheater, an electrical current is passed through a material and the material's resistivity causes power dissipation in the form of Joule heat. Since the metallic resistor is in direct thermal contact with the polysilicon film, heat is directly transferred into the microresonator. Through the thermal expansion of the polysilicon film, these local temperature variations produce local stress variations. The incremental film stress is then relieved by out-of-plane deformation of the membrane. Figure 3-2 illustrates a finite element analysis performed with ANSYS where $20 \mu\text{W}$ of heat is dissipated from the resistor into the film, producing a local change in temperature of less than 0.1 K and a vertical deflection of 0.0055 nm. As previously described in section 1.5.4, short thermal time constants in the MEMS system allow AC signals to be applied to the microheater that will excite standing waves in the resonator and thus enable a frequency selective response to the incident electrical signal.

The robust structure of the shell type resonator allows the resistor to be defined after the hydrofluoric acid etch, allowing metals to be used that are not compatible with HF acid. After the HF etch is used to define the cavity dimension of the resonator (figure 2-1 c), the wafer is again coated with photoresist for a second level of lithography. LOR 10-A is first spun on the wafer followed by a photosensitive layer of Shipley 1813. A second layer of optical lithography defines the areas that will be metalized. The resist is developed and the wafer is placed in an e-gun metal evaporator. First, an adhesion layer of 4.8 nm of titanium is evaporated followed by a layer of gold. A $70 \times 3 \mu\text{m}^2$ gold resistor that is 20 nm thick had a resistance of 95Ω , while a 40 nm thick resistor was 45Ω .

The location of the resistor on the resonator was carefully chosen for a number of reasons. First, the microheater can be positioned on the membrane to selectively excite a particular mode. This is advantageous for a multi-moded device causing the resonator to be preferential to a pre-determined mode of excitation. Secondly, locating the resistor at a point of maximum deflection induces significant damping in the structure due to viscous drag between free electrons and motions of the ions in the metal as they follow the mechanical oscillations (electron-phonon dissipation) [54]. Placing the resistor completely off the device (figure 3-3) allows the resonator to preserve its intrinsic quality factor. For example, in the 30 μm diameter domes, a resistor located immediately adjacent to the etch hole produced a 17 MHz peak with a Q of 2,000, a resistor located just touching the periphery produced a 17 MHz peak with a Q of 10,000 and a resistor in-between the previous, produced a 17 MHz resonance with a Q of 5,500. The ability to effectively drive the device with the resistor located completely off the resonator also demonstrates that this method of actuation is indeed thermally induced and not produced from a bimorph or capacitive effect. The disadvantage of locating the resistor off the device is that, by locating the point of maximum temperature variations off the device, the effectiveness of the drive is reduced. Thus, in resistive drive, there is a tradeoff between the Q and the drive efficiency.

To facilitate electrical testing, each end of the resistor is connected to 300 μm x 300 μm metal pads. The chip is mounted on a ceramic dual-inline pin (DIP) package (figure 3-5) and aluminum wirebonds are made between the bonding pads and the gold leads of the ceramic package. To allow sample interchanging, the ceramic package is mounted on a plastic DIP holder which is anchored to a Teflon plug sitting in a custom built vacuum chamber. Coax wire leads soldered to the DIP holder pass through the Teflon plug and are connected to a RF con-flat electrical feedthrough to allow

connections to 50 Ω driving electronics such as a spectrum/network analyzer or RF power amplifiers.

The electrical signal applied to the resistor can be described as:

$$V_{RF} = V_{DC} + V \sin(\omega t), \quad 3-1$$

where V magnitude of the RF voltage, and V_{DC} is the DC bias on the driving signal. The power dissipated by the resistor is

$$\begin{aligned} P &= \frac{(V_{RF})^2}{R} = \frac{(V_{DC} + V \sin(\omega t))^2}{R} \\ &= \left(V_{DC}^2 + 2V_{DC}V \sin(\omega t) + \frac{1}{2}V^2 - \frac{1}{2}V^2 \cos(2\omega t) \right) / R, \end{aligned} \quad 3-2$$

where R is the resistance of the microheater. Since the response of the resonator is frequency dependent, the higher frequencies are filtered out and the force from the resistive actuator driving at a particular mode of resonance (f_o) can be described as

$$F_{\omega_o} \propto \Delta \varepsilon \propto \Delta T \propto V_{DC} V_o \sin(\omega_o t), \quad 3-3$$

where V_o is the amplitude of the driving signal at (f_o), and ΔT and $\Delta \varepsilon$ is the local change in temperature and stress.

The dependence of Equation 3-3 on DC biasing is demonstrated experimentally in figure 3-4 where the relative S_{21} S-parameter (the magnitude of the photodetector output signal, divided by V_o from the network analyzer) is plotted versus V_o for several DC voltages. To make this measurement, the fundamental frequency was recorded at a particular DC bias and AC drive magnitude sufficiently low enough

to keep the resonator in the linear regime. The analyzer was then switched to network mode where a S_{21} power sweep could be performed at the previous CW frequency. Since DC bias shifts the frequency slightly, each curve is measured at a different center frequency. For low AC amplitudes, figure 3-4 shows the expected increase in the resonator vibrational amplitude in response to an increase of the DC bias of the driving signal. This dependence illustrates how DC bias can be used to control the gain of the MEMS system. S_{21} is seen to be constant for low AC amplitudes until the output no longer linearly follows the input and compression sets in due to nonlinearity. For high DC biases, compression is seen at lower RF drive amplitudes because the AC * DC drive force is larger. Thus, a wider input dynamic range can be obtained at lower DC biases, indicating the tradeoff between dynamic range and insertion loss.

In figure 3-4, a 200 mV DC bias translates to a S_{21} of -28 dB in the linear regime. This is of course only a relative measurement because S_{21} is a direct function of the incident HeNe laser power and the x-y position of the beam. By optimizing the position or changing the detection power, these curves can be vertically shifted in either direction.

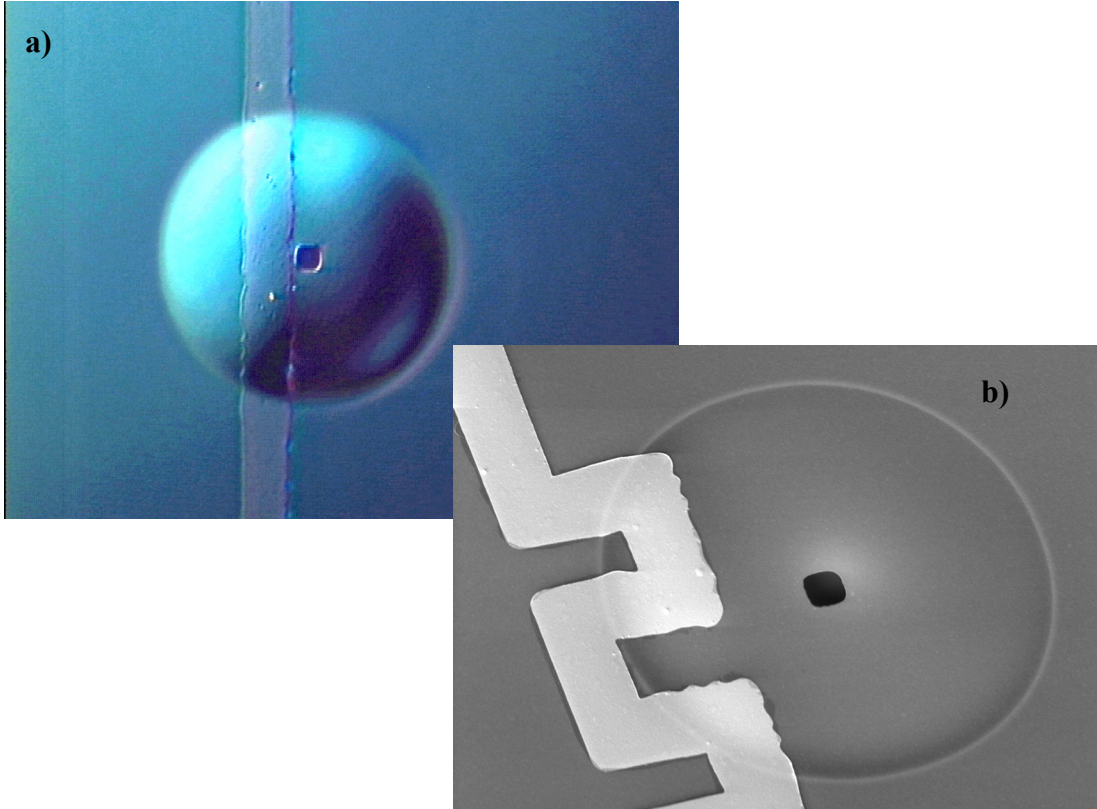


Figure 3-1: a) Optical DIC and b) SEM image of 30 μm dome resonator and gold heater.

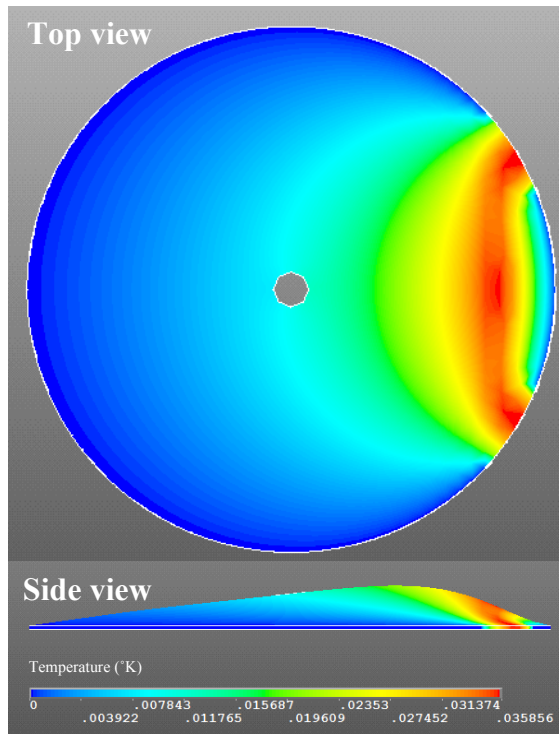


Figure 3-2: FEM simulation of temperature variations and static displacement induced by applying a thermal flux of $10 \mu\text{W}$ dissipated in a $3 \mu\text{m}$ wide strip on the polysilicon shell resonator. The periphery of the shell is constrained to be room temperature. A temperature increase of 0.036 K and DC vertical deflection (not pictured to scale) of 0.006 nm is produced in the membrane. $k = 150 \text{ W/mK}$, $\nu = 0.22$, $E = 165 \text{ GPa}$, $\rho = 2330 \text{ kg/m}^3$, and $\alpha = 2.6 \times 10^{-6} / \text{K}$.

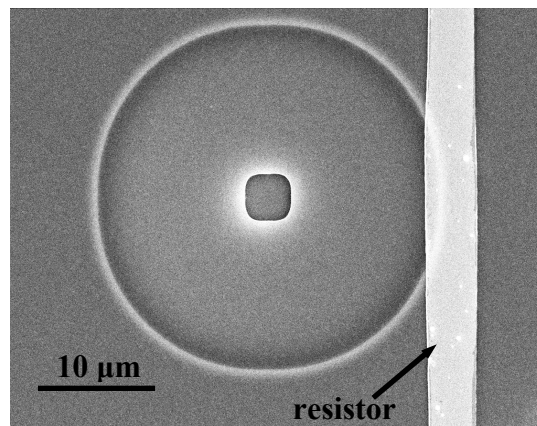


Figure 3-3: SEM image of dome and gold micro-heater located adjacent to resonator.

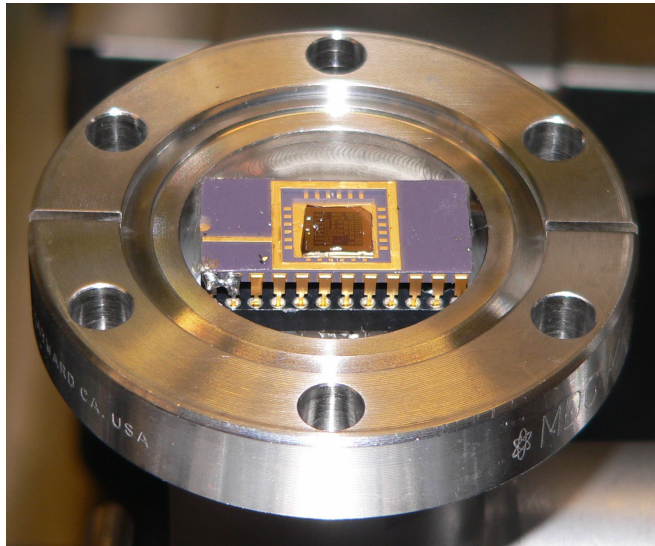


Figure 3-4: Dome substrate wirebonded to ceramic DIP holder and mounted in the vacuum chamber.

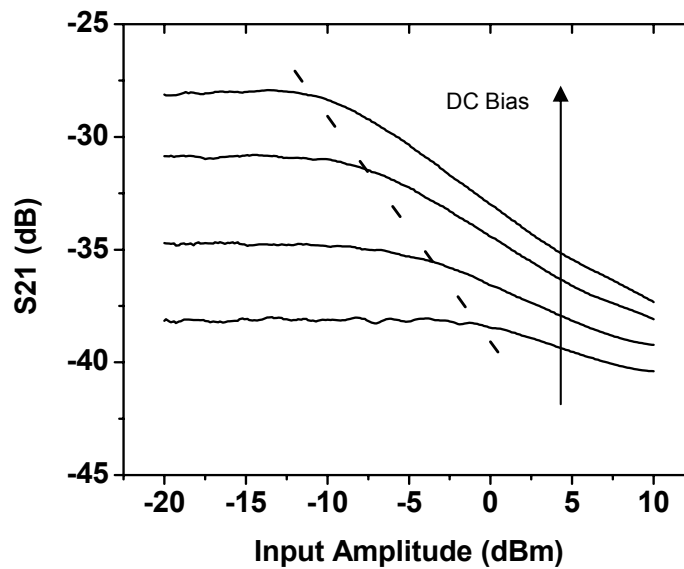


Figure 3-5: S_{21} S-parameter (which includes the efficiency of the photodetector and detection optics) of the thermal actuator + resonator sampled at the maximum amplitude of the 12.7 MHz resonant mode. DC bias on the network analyzer drive signal is (from lowest to highest) 75 mV, 100 mV, 150 mV, and 200 mV. Dashed line represents constant mechanical amplitude of 2.5 mV from the photodetector.

3.2 Resistive Detection

While most of the experiments in this work were carried out using interferometric detection due to its experimental ease of use, high signal to noise ratio, and near zero cross-talk, a much more compact and stable method of high frequency motion detection was needed for integration purposes. Detection of capacitive displacement current is a possible alternative; however, in order to be implemented with the dome resonator, top and bottom electrodes with nm size gap spacing would need to be implemented, significantly complicating fabrication. A second possibility, which would interface well with the system, is piezoresistive detection. Knowing that doped polysilicon has piezoresistive properties, we can implement a strain sensitive transducer directly into the polysilicon film resonator, yielding a stable and integrated transduction layout.

To define the piezoresistor, several additional microfabrication steps are inserted into the process described in figure 2-1. Following the definition of the etch hole, a second layer of photolithography is used to define the area of the polysilicon that will be doped to form the piezoresistive strip (figure 3-6). A $70 \times 3 \mu\text{m}^2$ area of implantation is positioned in the membrane to be sensitive to modes such as γ_{01} and γ_{11} described in figure 2-5. The implanted strip connects two $300 \times 300 \mu\text{m}^2$ implanted pads for probe access. Using a thick resist as a mask, the film stack was subjected to a boron ion implantation performed at Ion Implantation Services with a dose of $5 \times 10^{15} \text{ cm}^{-2}$ and an energy of 5keV. The resulting shallow implant creates an asymmetrical piezoresistive region through the polysilicon film thickness. After the resist mask is removed, subsequent rapid thermal annealing (RTA) at 900 °C for 30 seconds activates the boron and limits diffusion of the active species. A spreading resistance

profile (figure 3-8 a) shows active boron concentration varying between $1 \times 10^{20} \text{ cm}^{-3}$ and $1 \times 10^{17} \text{ cm}^{-3}$ through the 180 nm polysilicon film.

The asymmetrical profile allows for a change in resistance to develop in response to transverse vibrations, characterized by expansion in the top half and compression in the bottom half of the film, whereas uniform doping through the film would lead to cancellation of the net change in resistance in response to flexure. Since the gauge factor, $G = \left(\frac{\Delta R}{R} \right) \left(\frac{l}{\Delta l} \right)$ (where l is the length of the piezoresistor), of polysilicon varies with doping concentration (figure 3-7), the difference in the gauge factor between the top and bottom sections of the film determines the overall sensitivity to membrane stress.

The dose, energy, and activation anneal were critical to a successful piezoresistor sensor. To further understand the impact of these parameters, four doses 1×10^{13} , 1×10^{14} , 1×10^{14} and $5 \times 10^{14} \text{ cm}^{-2}$, all implanted at 5 keV, were tested. The first two doses were too low and produced very high value resistors with negligible voltage modulation. The 1×10^{14} and 5×10^{14} doses produced resistive values between 5 and 10 k Ω , which fell in the optimal piezoresistive region. The annealing time and temperature were critical as well. In using RTA, which heated the chip to activation temperatures in a few seconds, it was found that an anneal time of 10 seconds at 1100°C successfully activated the implanted region; however the process caused diffusion of the active species through the thickness of the film canceling the piezoresistive effect (figure 3-8 b). A more effective anneal was performed at 900 °C for 30 seconds, which activated the boron and reduced diffusion.

In future work, it is suggested that a sacrificial layer of oxide be deposited on top of the polysilicon resonator prior to the ion implantation. This additional step would reduce the need for an extremely low accelerating voltage by allowing the

majority of the implanted species to remain in the sacrificial material, while only a small profile would diffuse into the top part of the polysilicon film.

Following implantation and activation, the chip was placed in a HF bath to define the shell type resonator. To define the driving resistor, the previous metallization lift-off process was used, differing only in that the $300\ \mu\text{m} \times 300\ \mu\text{m}$ implanted pads were also covered with metal to allow the piezoresistor to be probed.

In the microresonator, the implanted polysilicon resistor monitors the high displacement resonant motion. Membrane deflection produces a corresponding strain in the shell membrane, which is converted by the piezoresistive effect of the doped polysilicon strip into a proportional fractional change in resistance. In a half-Wheatstone bridge configuration, a change in resistance in one of the two resistors will produce corresponding variations in the voltage at the center of the bridge. Strain developed in the resonator along the piezoresistive strip is on the order of 10^{-5} , which, for a differential gauge factor of ~ 10 , a bridge bias of 10V, and resistor value of 4 k Ω , should produce an AC output signal of about 1 mV.

Initial resonator testing was performed using DC probes (rated to 10 GHz) in a Desert Cryogenics vacuum probe station at room temperature and a pressure of 10^{-5} torr. The network analyzer RF drive was biased with 200 mV and applied to the 50 Ω microheater input (figure 3-11). The half bridge output transducer was biased with ± 5 V and a third probe connected the middle of the bridge to the 50 Ω input of a network analyzer. The resulting resonator spectrum of this configuration is shown in figure 3-9 a,b. In the polar plot (figure 3-9 b), the peak of the resonance has a magnitude of 10 μV and is offset from the origin due to coupling (crosstalk) between the drive and detection, producing a non-Lorentzian peak.

By subtracting the background crosstalk vector and thus shifting figure 3-9 b to the origin, we can reconstruct the Lorentzian shape (figure 3-10) from figure 3-9 a.

Crosstalk between the microheater and the piezoresistor was found to be on the order of -80 dB and was dominated by capacitive coupling rather than thermal coupling within the resonator itself. Since the resistivity of the piezoresistor is also influenced by the membrane temperature, it was expected that thermal drive would have significant coupling to the output transducer. The primary method of coupling was determined by changing the DC bias on the driving signal. By increasing the microheater bias, both the power dissipated and the thermal driving force were increased; thus if cross-talk was thermal in nature, both the noise floor and the resonator response should increase. However, a change in the DC voltage only produced a change in the resonator response, indicating that the local temperature field was small enough that coupling between the input and output transducers was not thermal in nature and was probably dominated by electrostatic fields between the large bonding pads or probes.

A disadvantage of directly coupling the Wheatstone bridge to the spectrum analyzer is the loss of signal due to voltage division between the implanted resistors and the $50\ \Omega$ spectrum analyzer input. For example, with a $10\ \text{k}\Omega$ piezoresistor, a 100x signal division takes place at the input of the spectrum analyzer. A high impedance buffer amplifier placed directly on the piezoresistive bridge output reduces voltage division and eliminates parasitic capacitances associated with probes and cabling. An Analog Devices AD8079 high-speed buffer with a gain of 2 and a $10\ \text{M}\Omega$ and $1.5\ \text{pF}$ input resistance and capacitance was used. The op-amp was soldered to an AD8079 prototyping board (figure 3-12, 3-13) and the resonator chip was then taped to the same PC board. Wirebonds were made to the bonding pads of the metal heater and piezoresistor. The opposite end of the wirebonds were then carefully attached to the prototyping board using indium solder. Gold ribbon wirebonds were used to avoid large capacitive effects caused by the native oxide present on aluminum wires.

Figure 3-10 overlays the Lorentzian waveform produced by the same resonator and -20 dBm RF drive, only now wirebonded to the amplifier prototyping board. It can be seen that the response is now almost 2 orders of magnitude larger than when the resonator was not coupled to the high impedance amplifier. The background noise vector is substantially larger, which is attributed to coupling between the unshielded gold ribbon wirebonds. The insertion loss is now approximately -30 dB, which can be further reduced by optimizing the gauge factor and the implantation depth, dose, energy, and activation anneal.

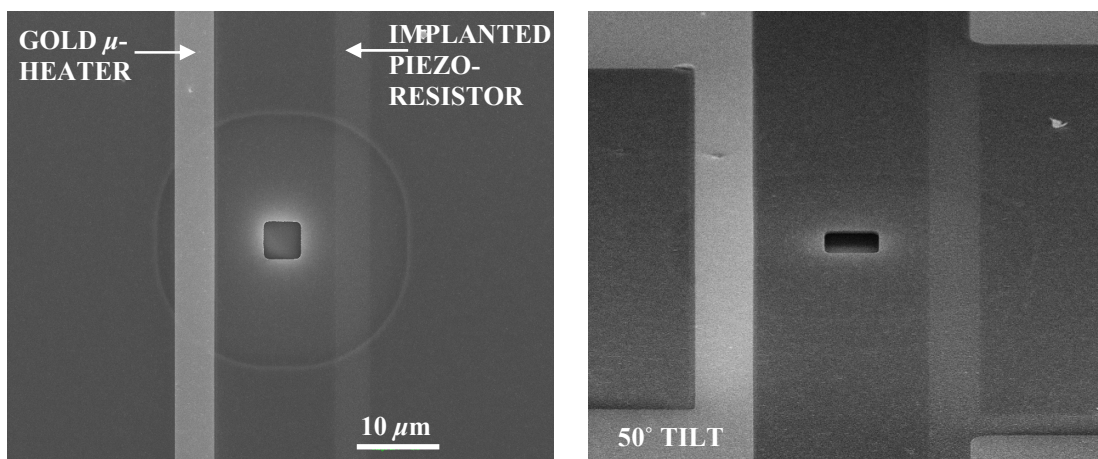


Figure 3-6: SEM image of a shell-type RF MEMS resonator with integrated resistive transducers. The white outer ring produced from secondary electron effects defines the circumference of the membrane. A 30 nm thick metal resistor and an implanted p-type resistor form the input/output transducers. Image obtained using a mix of in-lens secondary detector and in-lens energy selective backscatter detector on a Carl Zeiss Ultra 55.

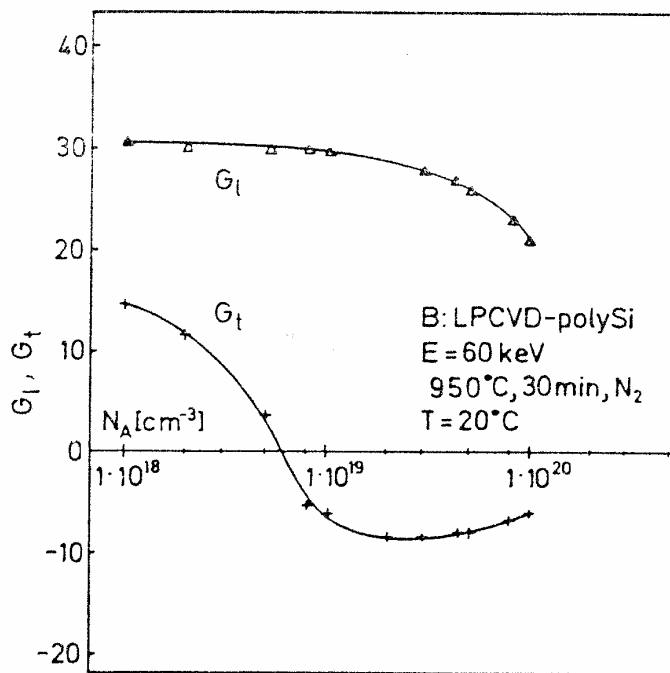


Figure 3-7: Gauge factor of polysilicon. Reproduced from reference [55]

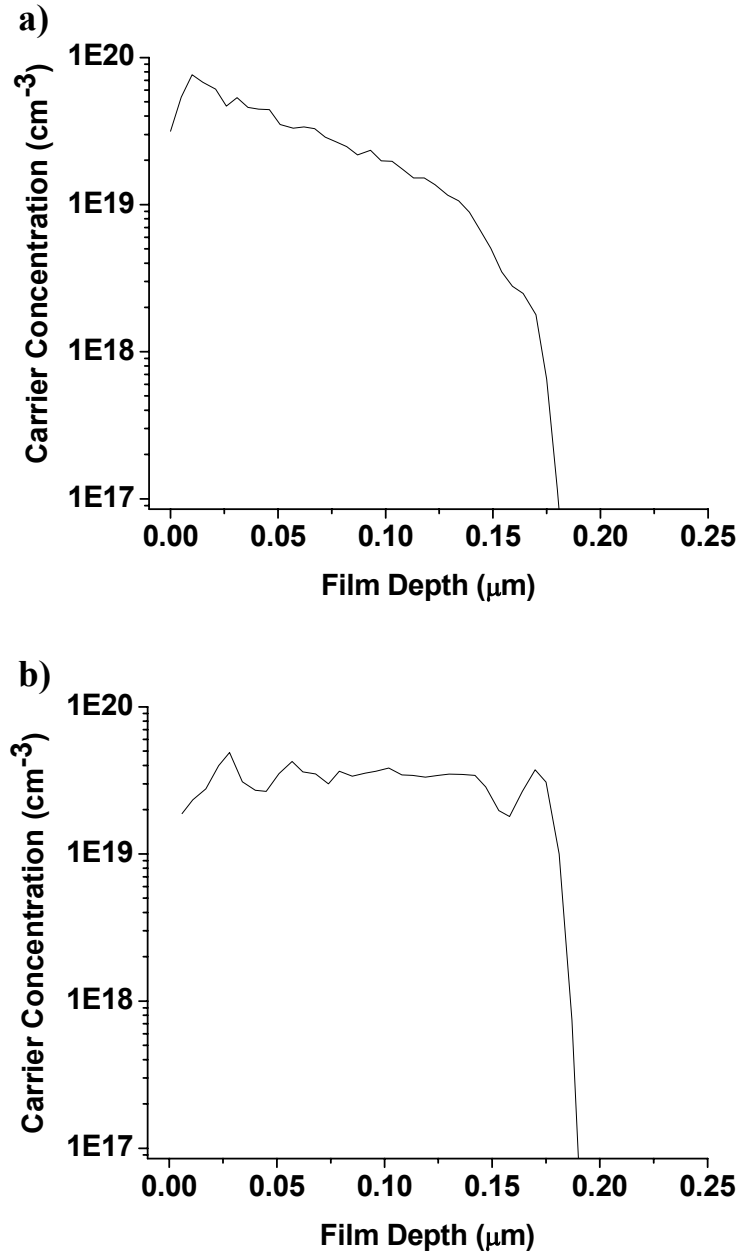


Figure 3-8: Carrier concentration profile of ion implanted polysilicon region, post RTA. Both are profiles are determined by a spreading resistance analysis performed by Solecon Laboratories. a) dose: $5 \times 10^{15} / \text{cm}^2$, energy: 5 keV, anneal: $900^\circ \text{C} @ 30 \text{ sec}$ b) dose: $5 \times 10^{15} / \text{cm}^2$, energy: 5 keV, anneal: $1100^\circ \text{C} @ 30 \text{ sec}$.

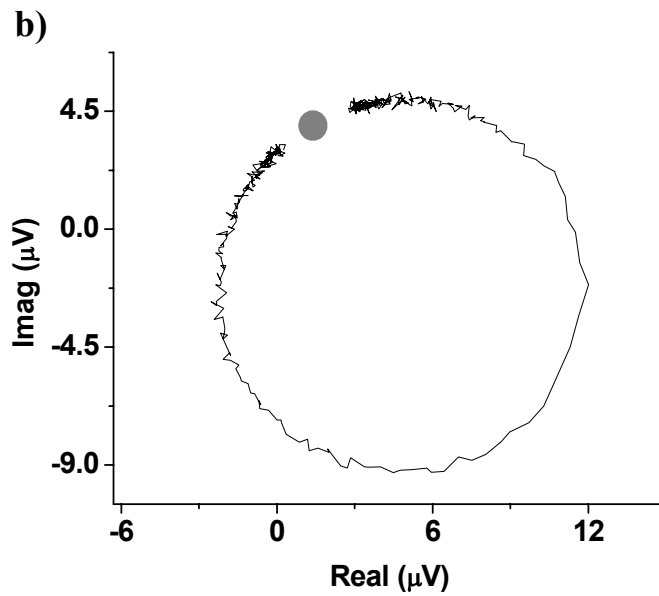
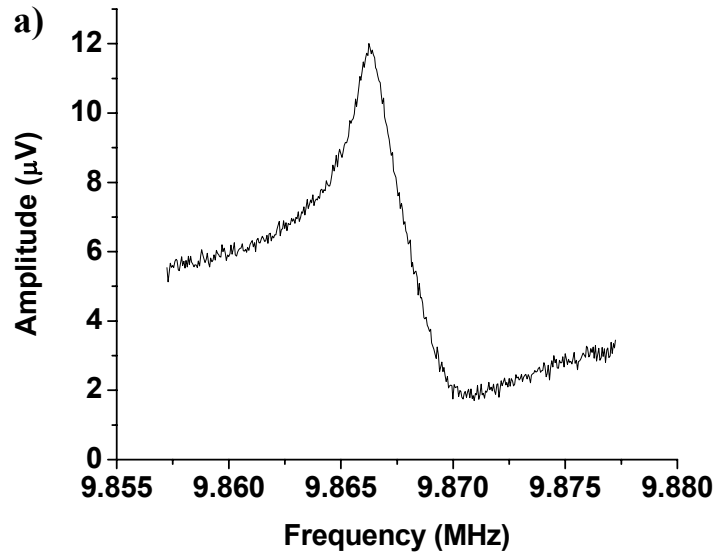


Figure 3-9: a) Square root magnitude of voltage detected by spectrum analyzer from piezoresistive half-Wheatstone bridge. b) Real and imaginary component of voltage over corresponding frequency range.

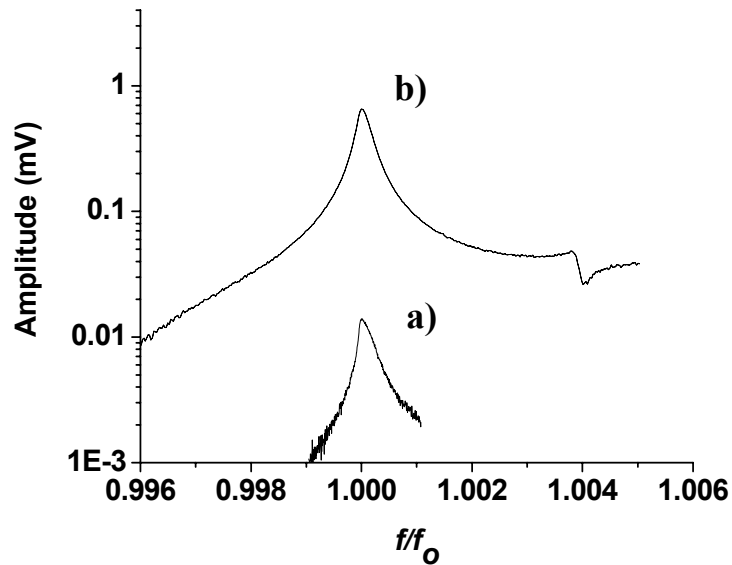


Figure 3-10: The Lorentzian response of one membrane mode preferentially excited and detected by resistive transducers both uncoupled (a) and coupled (b) to an operational amplifier. The background cross-talk vector indicated by the gray dot in figure 3-9. b is subtracted out of both data sets. Microheater drive signal: -20 dB with 250 mV bias, 10 V piezoresistor bridge bias.

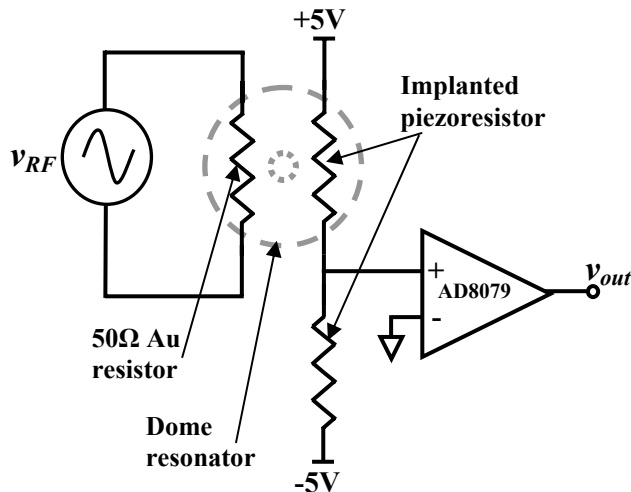


Figure 3-11: Electrical signal path of the resistively transduced MEMS resonator.

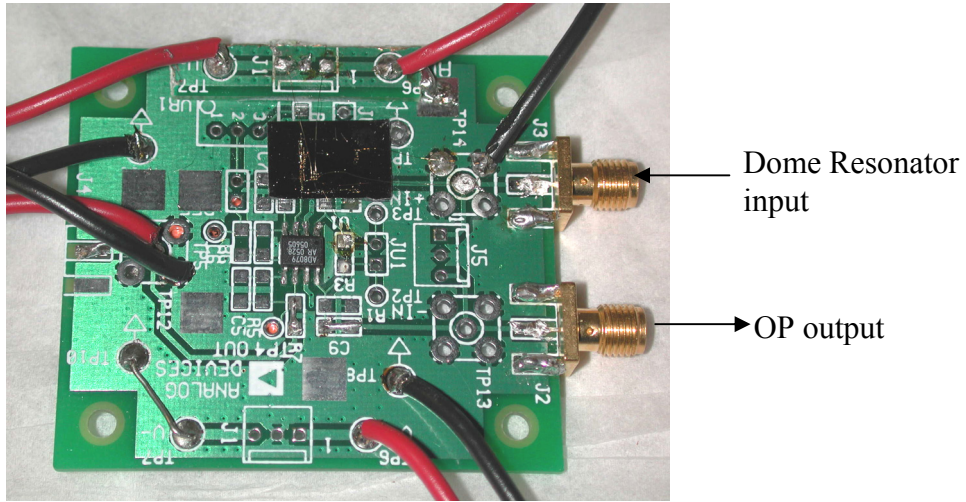


Figure 3-12: Prototyping board for AD8079 amplifier with dome substrate taped to board and electrically inserted between the SMA input and the amplifier input pin. Red and Black wires are BNC connectors for biasing, ± 5 V for piezo bridge, and ± 5 V for AD8079. Gold ribbon wires are wirebonded to resonator bonding pads for ± 5 V, gnd, v_{in} , and v_{out} and then soldered to prototype board. Board is then placed in a vacuum probe station and connected to SMA connectors within the vacuum environment.

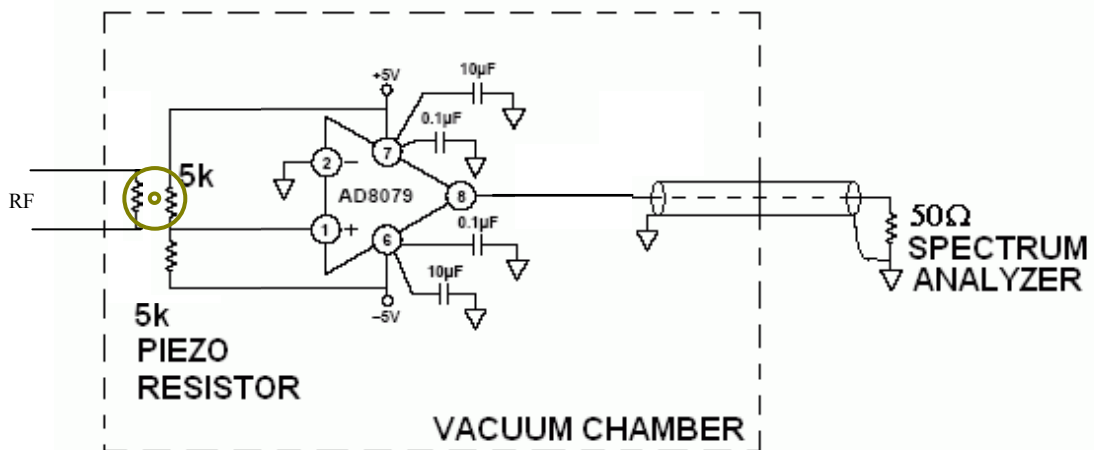


Figure 3-13: Electrical schematic of AC and DC network for amplifier and resonator.

3.3 DC Heating Frequency Control and Temperature Effects

Similar to the process by which electrostatic drive can provide for frequency tunability of a resonator through a DC bias (equation 1-15), thermal drive can change the resonator spring constant with the DC level of the driving signal. We previously observed that heat, incident on a slightly curved structure, will change the local stress of the structure. Slow varying or steady state power dissipation (i.e. that produced from the DC bias on the driving resistor) affects the average spring constant in the resonator, effectively tuning the natural frequency. Depending on the location of the resistor and the mode of oscillation, DC effects either increased or decreased (through stiffening and softening the spring constant, respectively) the resonant frequency of the device. The aforementioned 30 μm dome exhibited up to a 2 Hz/ μW dependence on the incident power. Such sensitivity to static or low frequency thermal effects is one of the primary disadvantages associated with optical transduction and a significant benefit of resistive transduction. Since most flexural resonators have a finite degree of curvature from residual stress in the film, interference effects produced by the resonator, the varying gap, and the substrate make these membranes position sensitive to incident light. Movement of the laser focal spot across the surface of the membrane causes changes in the amount of absorbed heat, thus altering the vibrational spectrum and illustrating how instabilities in the optical path translate to frequency and amplitude instability in the resonator. Since resistive coupling is integrated into the device, the thermo-vibration instability associated with the transduction elements is eliminated.

Ambient temperature was shown to have a significant effect on the membrane and transduction elements. Temperature similarly impacts the frequency of the resonator by changing the overall film stress or by changing the transducer resistivity

and affecting power dissipation into the device. For the resistively transduced resonator, a temperature coefficient of approximately 2 kHz/°C was measured. The tools necessary to measure the coefficient of the membrane or the membrane + heater independently were not available at the time; however, speculation suggests that the implanted piezoresistor is responsible for the large temperature coefficient since the semiconductor's free carrier density depends exponentially on temperature. A temperature coefficient in piezoresistive sensors is ordinarily compensated for by implementing the sensor into a Wheatstone bridge, where all resistors have the same thermal coefficient, thus the current through the bridge will change without affecting the output voltage. However, a change in current will alter the power dissipated by the resistor leading to a frequency shift in the resonator. Thus a balanced bridge will not be able to compensate for any change in temperature. To compensate for temperature, a proportional to absolute temperature (PTAT) circuit could be used to bias the driving signal of the resonator and compensate for the temperature coefficient of the system.

4 CMOS Integration of MEMS Resonators

4.1 Introduction

In the previous sections, it was demonstrated how a micromechanical resonator can be inserted into an electrical signal path to allow the resonator to perform frequency dependent operations on the incident signal. Resistive coupling was also successfully implemented as an actuation and detection method that can be completely integrated into the plane of a MEMS resonator, enabling compact and stable transduction with minimal geometrical restrictions. This integrated design proves to be a valuable step towards merging solid-state electronics with micromechanical resonators.

The ability to integrate MEMS – capable of high fidelity signal processing – with CMOS amplifiers and digital logic, offers significant advantages. Integrating MEMS as filters, mixers, and oscillators alongside solid-state field effect devices will allow a complete radio architecture to be implemented into a single silicon chip less than $1 \times 1 \text{ mm}^2$, dramatically down scaling the dimension of wireless communication hardware, permitting new applications, and reducing manufacturing costs. Applications which would benefit from MEMS and CMOS electronics in a single chip package include cell-phone transceiver architectures, wireless medical sensors [56], smart dust sensors [57], radio frequency identification (RFID) tags [58], and phased array radar.

There are several fabrication processes currently commercially available for MEMS integration. Polymumps is a 3 layer polysilicon micromachining process where all three layers are 500 nm thick (too thick for most flexural resonators) with no option for on chip field effect devices. The SUMMiT fabrication process from Sandia

National Lab is a similar process with structural films ranging between 0.8 μm and 2.25 μm , also with no CMOS integration.

This next section presents research focused on the integration of micromechanical resonators and their corresponding detection electronics into a standard CMOS fabrication processes that makes no compromises for incorporating free standing MEMS structures into a layout. While many groups have claimed that their devices are “CMOS compatible,” this claim is most often derived from the fact that their geometries are silicon or polysilicon based and thus “must” be able to be integrated into a conventional process. However, little thought is actually placed on how the device and corresponding transducers will actually fit into a CMOS process flow and the effects of standard fabrication steps on device performance.

4.2 3D-SOI

To substantiate the claim of CMOS compatibility, two different fabrication technologies that are or will be available to digital and RF integrated circuit designers are used to integrate CMOS and MEMS. All CAD was designed within the Cadence Design System environment and all circuit simulations were performed using documented specifications provided by the design house for the Cadence Spectre or SpectreS environment. The first process described is a three dimensional silicon-on-insulator (3D SOI) run geared toward increasing the density of standard planar CMOS. The 3D SOI process, available from MIT Lincoln Labs, is unique in that it combines three independent SOI CMOS levels into a single wafer stack. Figure 4-1 illustrates the cross-sectional view, where SOI wafer 1 is the structural base and tier 1 of electronics. To form tier 2, the handle of SOI wafer 2 is removed and the wafer is inverted and oxide bonded to wafer 1. Tier 3 is created in a similar method, by again

removing the silicon handle, inverting the remaining wafer and bonding it to tier 2. Tungsten plugs then electrically connect tier 1 to tier 2, and tier 2 to tier 3.

This process is particularly advantageous to us because it facilitates easy post processing by leaving the active parts of tier 3, which will form the suspended membrane, very close to the surface. Figure 4-2 illustrates how the basic structure of an inverted SOI transistor is used to integrate a circular resonator into the 3D SOI process. In the SOI transistor, a 40 nm thick silicon island forms the active part of the field effect device, containing the doped source and drain as well as the channel region. The channel is controlled by a 200 nm thick doped polysilicon gate which is isolated from the silicon island by a 4.8 nm gate oxide. If we extend the polysilicon gate layer (Poly_C) over the island (figure 4-2 b) we begin to see how a resonator may be implemented. By predefining an etch hole (figure 4-2 c) into the poly membrane, a subsequent wet etch can be used to remove the overlaying and underlying oxide surrounding the poly. After receiving the die from MIT-LL, the membrane area is exposed by performing lithography on the 3D SOI die to define the resonator circumference in a layer of resist or chrome. A subsequent wet oxide etch will start from the top of the cap oxide, expose the top surface of the resonator, and continue through the etch hole to allow undercutting of the resonator. The resist or chrome mask prevents the wet etch from releasing any part of the wafer other than the bondpads and the resonator. Poly_B (on tier 2) is defined below the resonator to provide a wet etch stop and a reflective surface to make possible interferometric detection. The resonant spectrum of a 40 μm flat membrane, integrated into the 3D SOI process and then released with the aforementioned process, is shown in figure 4-3.

To implement an integrated resistive actuator, a 6.876 x 75.8 μm^2 strip of silicon island, doped with either CBN n-channel body implant or CAPN $1 \times 10^{19} \text{ cm}^{-3}$

n-type island implant, is defined across the surface of the resonator (figure 4-4). It is standard practice to form a polysilicon silicide to improve ohmic contact between the first metal layer and the gate electrode. Since all areas of polysilicon will be shorted together due to the thin metallic layer on the bottom surface, the silicon island resistor is particularly advantageous because it is electrically isolated from the polysilicon membrane via the gate oxide. In the design rules, it is prohibited to dope the silicon island without doping the above polysilicon (with NSD n+ degenerate implant); however we ignore the rule and leave the polysilicon undoped in case there is a gate oxide short, which is highly probable in such a large area. The fact that there is no polysilicon silicide block in this fabrication process eliminates the idea of using a NSD doped strip of polysilicon as an implanted resistor; however a silicide block will be available in the next generation of 3D SOI. Metal 1 contacts to the active island resistors, which must run through a via in the poly membrane, are located at more than twice the membrane radius away from the etch hole to prevent any contact with the HF etchant. Bonding pads, which interface to the resonator driving and detection electronics are implemented as large doped Si-island sheets. This allows the wet etchant to expose the bonding pads when the resonator is released, without affecting the conductivity. If conventional metallic pads were used, the HF would most likely react with the exposed metal and create unreliable and unpredictable contacts.

Piezoresistive displacement sensors are implemented in similar fashion to the resistive actuator. On the opposite side of the resonator, a silicon island resistor is defined across the surface of the resonator and a second, equal dimension, resistor is placed adjacent to the dome. Since the doped silicon is piezoresistive, we can implement a full Wheatstone bridge and generate a voltage signal at the center of the bridge proportional to the membrane displacement. The silicon island is particularly advantageous for piezoresistive detection, because it is located in the top half of the

resonator film, thus experiencing only net compression or expansion in response to resonant motion, maximizing the output signal.

A SOI CMOS based differential amplifier is located on tier 1 to provide maximum isolation between the mechanical resonator and the detection electronics. The three-tier system could allow us to minimize the overall footprint of the resonator and amplifier by allowing vertical integration; however for simplicity we chose to locate the amplifier away from under the resonator. A basic differential amplifier and voltage follower (figure 4-5) are used to boost the signal directly from the Wheatstone bridge. M0, the n-type SOI transistor, is the non-inverting input and is connected to two 11 k Ω static silicon island resistors. The gate of M1 is the inverting input and is connected to the middle of the bridge between the 11 k Ω static resistor and the variable piezoresistor on the membrane. P-type SOI transistors M2 and M3 complete the design of the active current mirror differential amplifier. These transistors are optimized to provide maximum gain when the DC bias on the input of M0 and M1 is $V_{dd}/2$, allowing the bottom Wheatstone bridge to be at ground. M6 is an active current source whose current is defined by the biasing network of M9 and M4. Finally, M5 and M10 form a voltage buffer reducing the output voltage and impedance. A Cadence Spectre simulation of the differential amplifier is pictured in figure 4-6 showing about 40 dB of gain with a 3 dB gain roll-off point at 70 MHz.

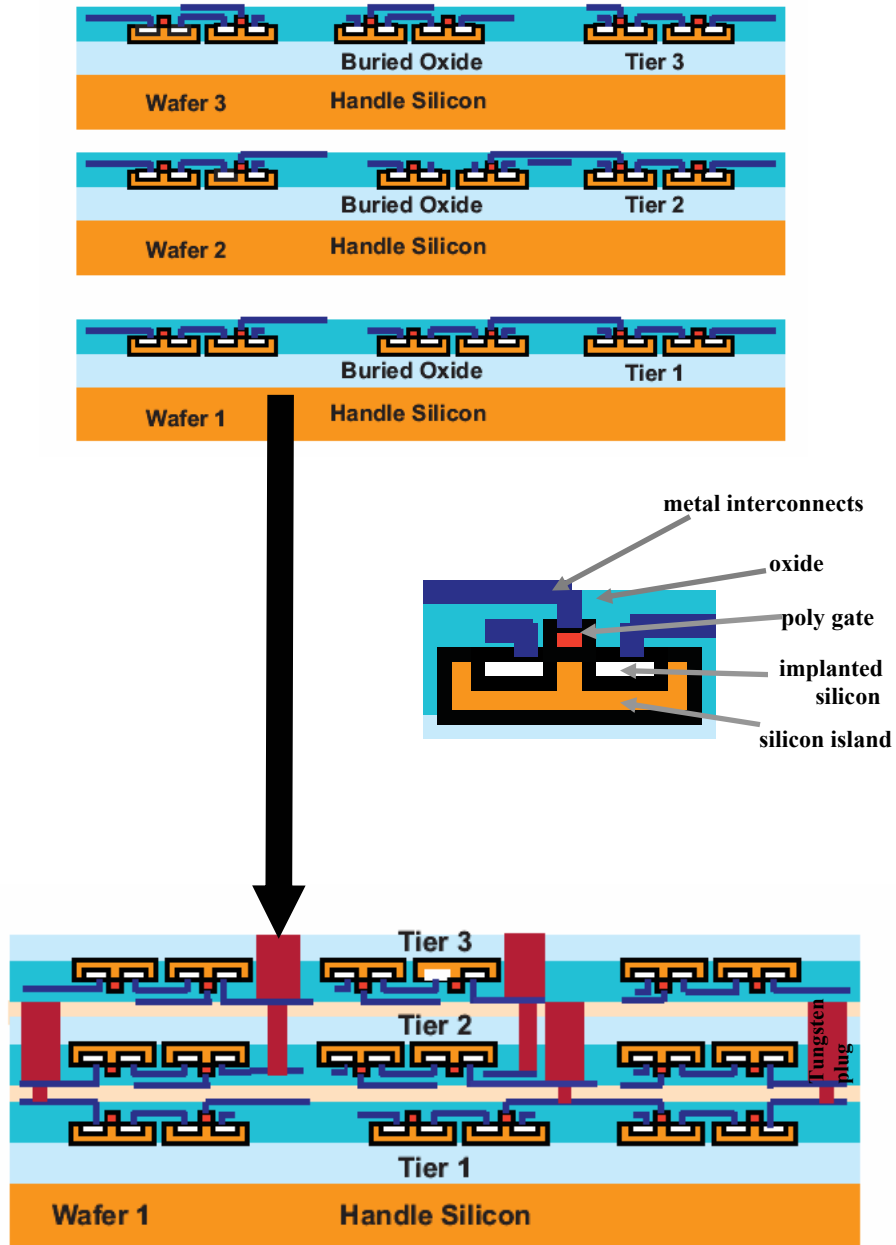
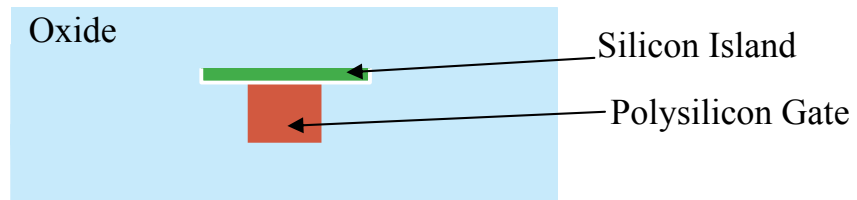


Figure 4-1: Cross-sectional view of wafer stack in 3D-SOI process.

Step 1 – Use inverted tier3 SOI transistor



Step 2 – Define a large plain of gate level polysilicon.



Step 3 – Pre-define etch hole within poly geometry. Post processing uses HF to release polysilicon membrane. Silicon island remains as resistive transducer.



Figure 4-2: Method for using film structure for standard SOI-FET transistor to implement a MEMS membrane and transducer.

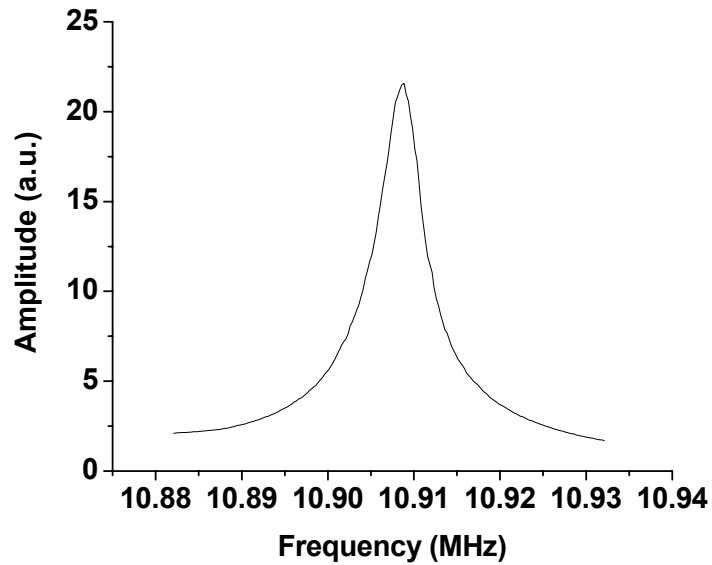


Figure 4-3: Resonant vibration of a laser driven, laser detected 40 μm diameter membrane resonator predefined in the 3D SOI process. Two types of membranes were released and tested. Membranes composed of just the polysilicon gate layer produced Q 's ranging between 5000 and 8000 depending on the mode of vibration. "Sandwich" membranes with a large sheet of thin silicon island separated from the poly gate by the gate oxide had more heavily damped vibrations with Q 's between 1500 and 2500.

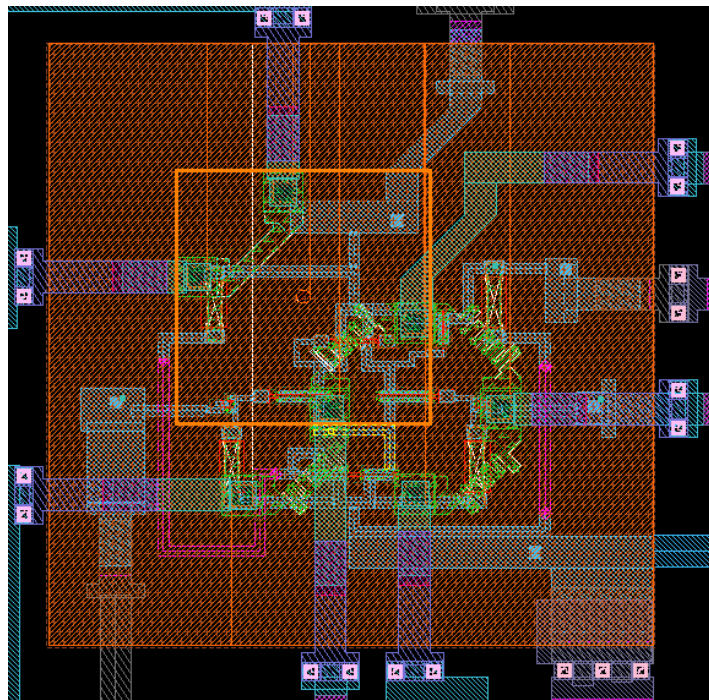
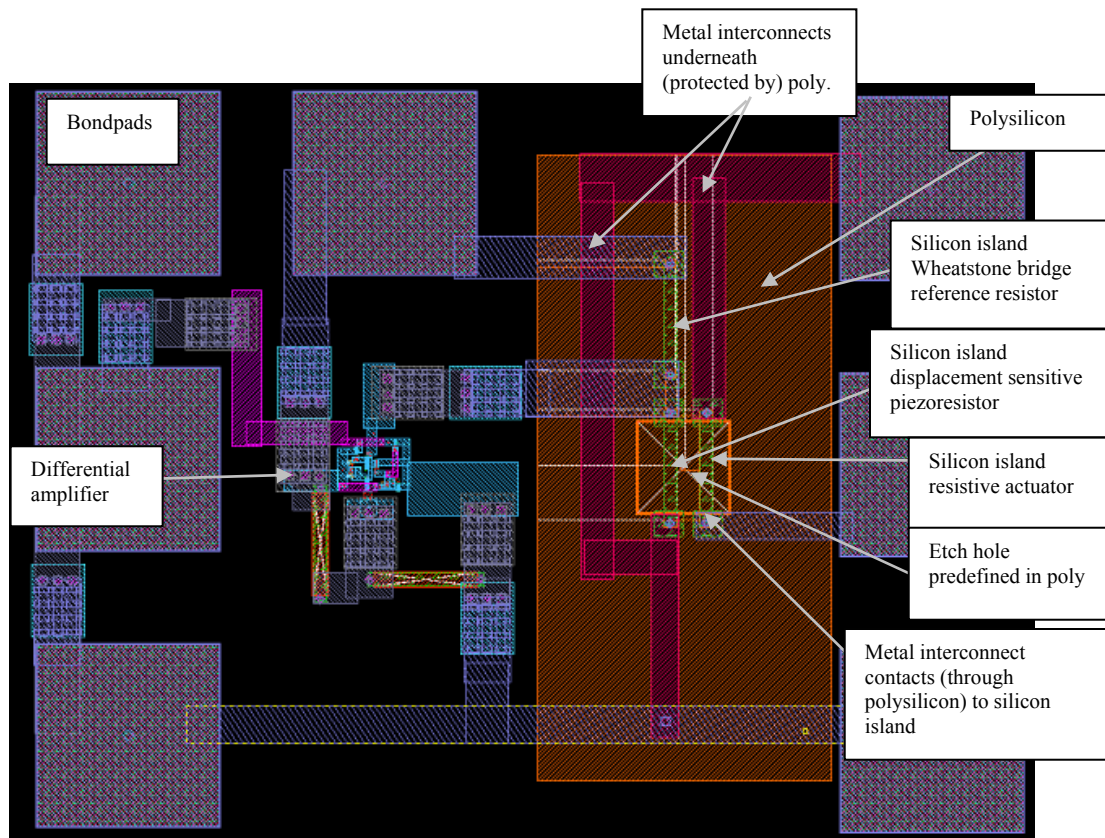


Figure 4-4: Two layouts for incorporating a dome membrane into 3D SOI process

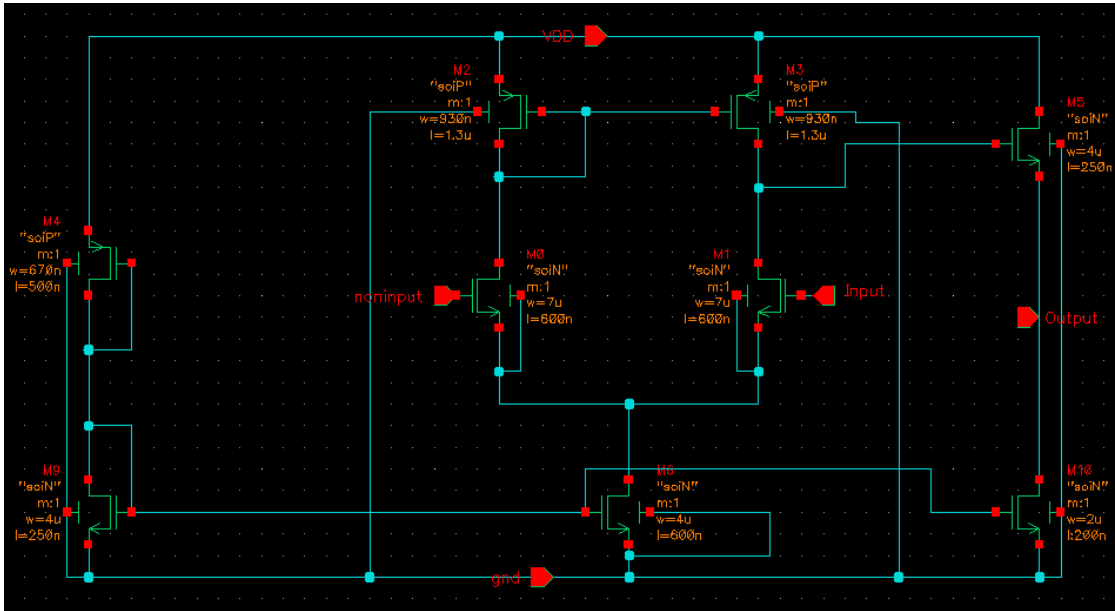


Figure 4-5: Differential to single ended SOI FET electronics to amplify signal out of Wheatstone bridge.

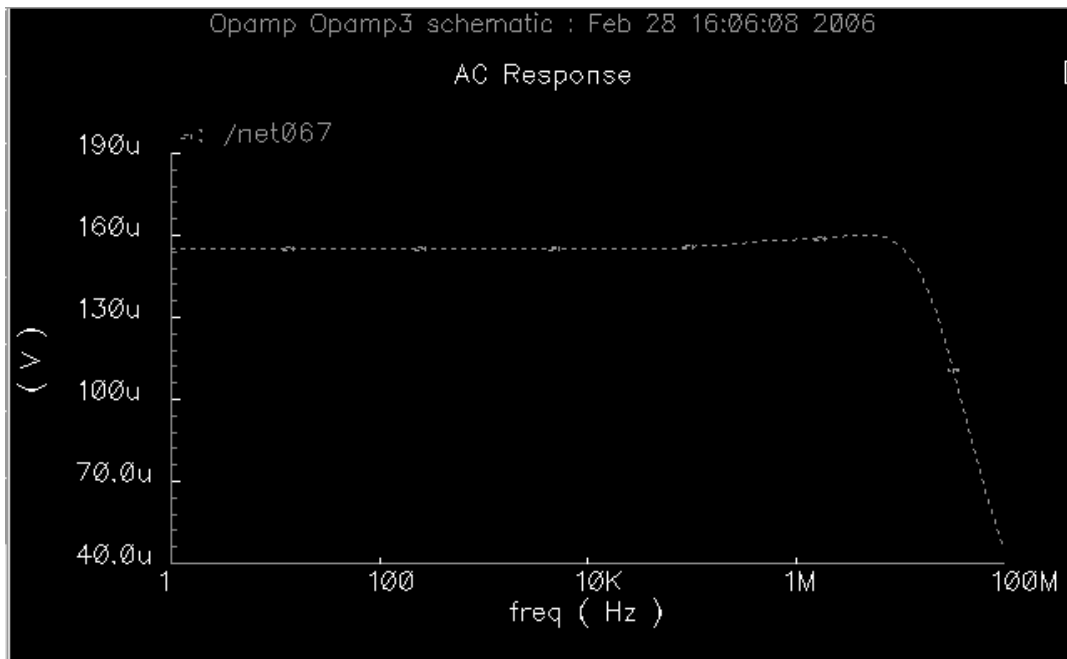


Figure 4-6: Simulated response from amplifier in figure 4-5. $1 \mu\text{V}$ input signal biased with $V_{dd}/2$ DC bias.

4.3 IBM BICMOS

The second fabrication process which was utilized to combine resonant structures with solid state electronics was an IBM 0.18 micron SiGe BiCMOS 7WL fabrication run geared toward high frequency ($f_i = 40$ GHz) RF electronics. Although this run was never fabricated, the design techniques to incorporate a resonator into this process could be applied to a wide variety of CMOS runs.

Like the 3D-SOI process, the gate layer polysilicon film of the IBM process was used to form the structural layer of the MEMS resonator. In the Cadence layout (figure 4-7) a large area of polysilicon (PC) with a predefined etch-hole can be observed. The field of poly is defined over an isolation trench of 300 nm of thermally grown SiO₂ (LOCOS), which provides lateral isolation between the source and drain of adjacent transistors. From figure 4-8 it is also noticed that 600 nm of oxide above the polysilicon isolates the gate from the above interconnect layers. This allows a 200 nm poly structural layer to be defined and suspended when the surrounding oxide layers are removed.

Gaining access to the resonator is particularly challenging, since there are 7 layers of metal in this process, and about 12 μm of low temperature oxide to provide interconnect isolation. We use a 4 μm thick top metal layer (MA), normally designated for bonding pads, to serve as a mask for post processing. Additionally we refrain from placing M1 – M6 above the resonator (figure 4-8). This way, MA can be used to mask a RIE etch which will remove the oxide only above the poly membrane. The thick MA layer will prevent the RIE etch from removing any other parts of the chip which contain interconnects and active devices. A disk of M1 metal is placed above the resonator to provide a RIE etch stop. The M1 metal can then be removed

with a wet etch, and a subsequent HF etch will free the resonator from the surrounding oxide.

Implementing the resonator transduction electronics is relatively straightforward since the PC gate layer can be doped and is thus inherently resistive. The poly gate in this process also has a silicide covering the top surface that will make the entire membrane electrically connected unless we define a silicide prevention mask. Layer OP is used to prevent silicide formation on a doped section of polysilicon membrane creating a resistive strip located on the periphery of the resonator. This resistive strip forms the integrated microheater actuator. In this process, capacitive displacement detection was used although, in retrospect, piezoresistive detection may have been easier to implement. A ground plane was inserted through the middle of the resonator by placing two areas of silicide protection with a grounded strip between them. The half of the circular resonator not occupied by the resistive actuator is left coated with silicide, forming the conductive top half of the output capacitor. The bottom half of the capacitor is formed by the doped n-well region. Both capacitor plates are then directly connected to the M1 interconnect layer which has a short lead to the first transistor in the transimpedance amplifier (figure 4-10). The significance of this distance is illustrated in figure 4-9. Any parasitic capacitance the output may experience serves to form a voltage divider at high frequencies and will thus dramatically decrease the output signal. This is part of the justification for integrating the MEMS resonator within the CMOS process immediately adjacent to the input transistor, rather than placing a separate microfabricated MEMS wafer mounted on top of the CMOS package. All of the critical parts of the design – the isolation oxide, doped polysilicon, metal mask etc. – are standard within a CMOS process; thus this design is a template for implementing suspended resonators into a wide variety of integrated circuit processes.

A transimpedance amplifier is used to convert the displacement current (equation 1-21) from the output capacitor into a voltage. The overall schematic is shown in figure 4-11. A basic differential amplifier with an output voltage buffer and positive feedback is used. Transistors TP330, TP331, TN332, TN333 make up the differential amplifier while TP331 is the active current source. RPC2 controls the current through TN330 which regulates V_{gs} of both TN330 and TP331, setting the current through the differential amplifier. TN337 and TN334 form a voltage follower amplifying stage which reduces the high impedance of the differential amplifier and the DC voltage on the output, increasing the head room of the amplifier while additionally providing Miller compensation. RRR0 is the feedback resistor setting the gain of the amplifier. The resistive network RPC0 and RPC1 correctly balances the left differential input. The output from the amplifier and the input to the resonator are directly routed to a set of bond pads on the top of the wafer enabling wafer level probing of the integrated MEMS and CMOS electronics.

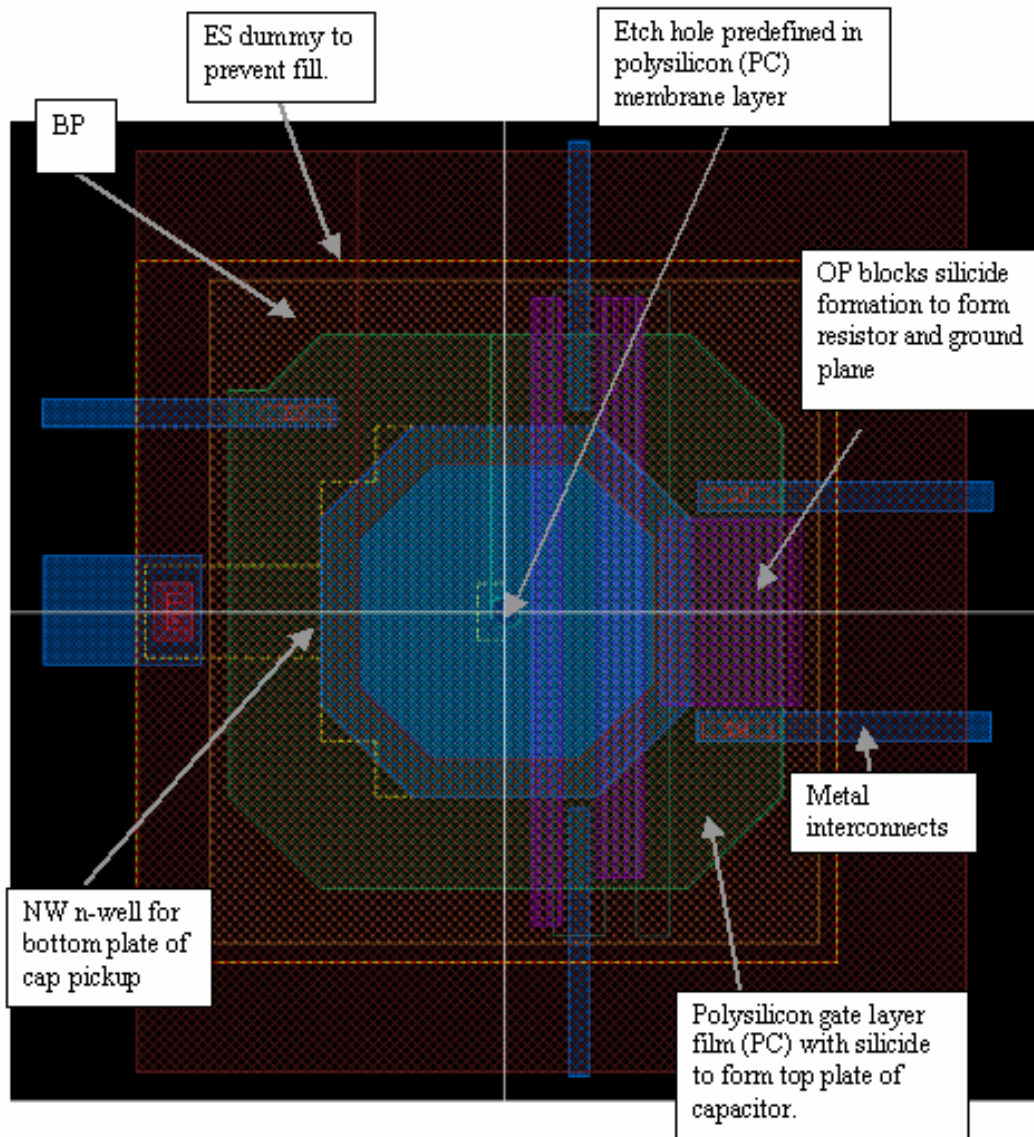


Figure 4-7: Method for integrating MEMS resonator and transducers into IBM BiCMOS process flow.

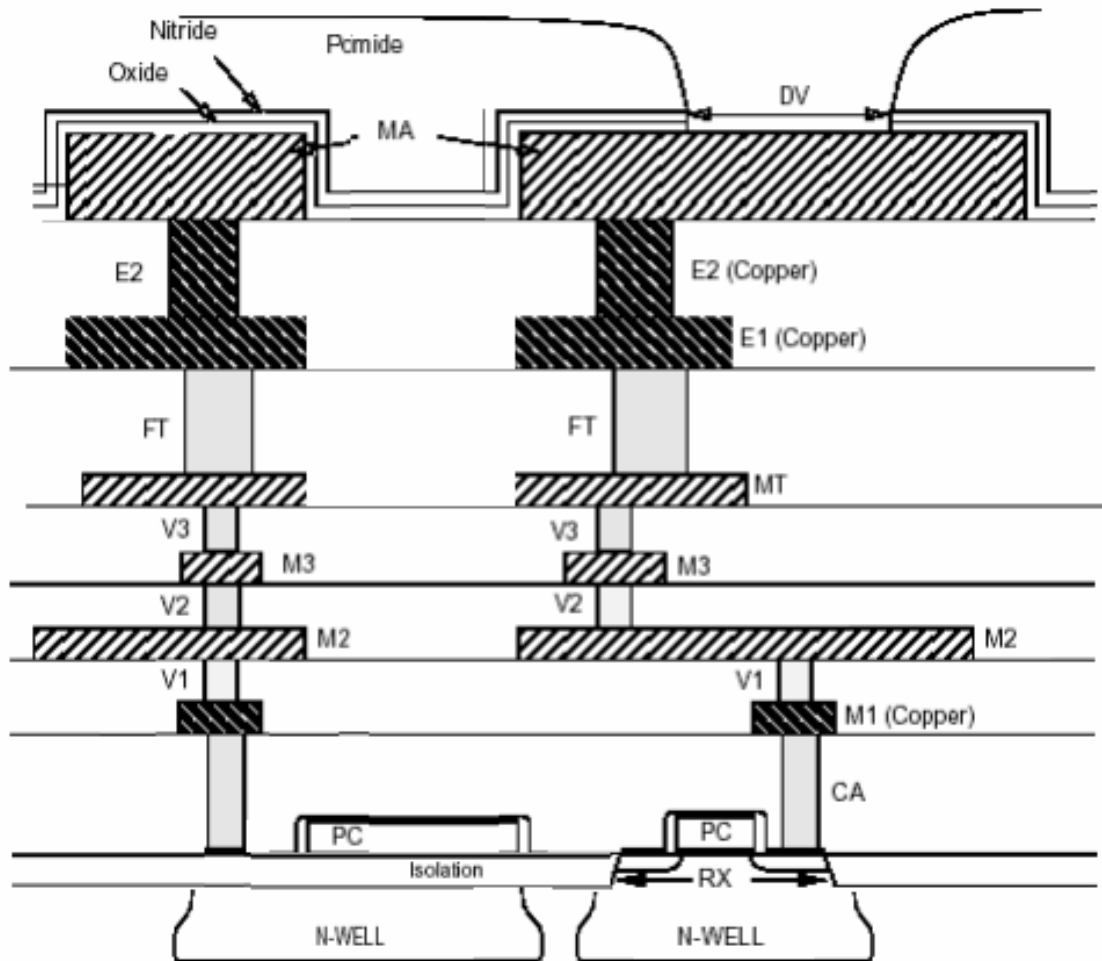


Figure 4-8: Cross sectional view of IBM BiCMOS process configured to implement resonator. Metal interconnect layers are configured to allow post processing access to the membrane.

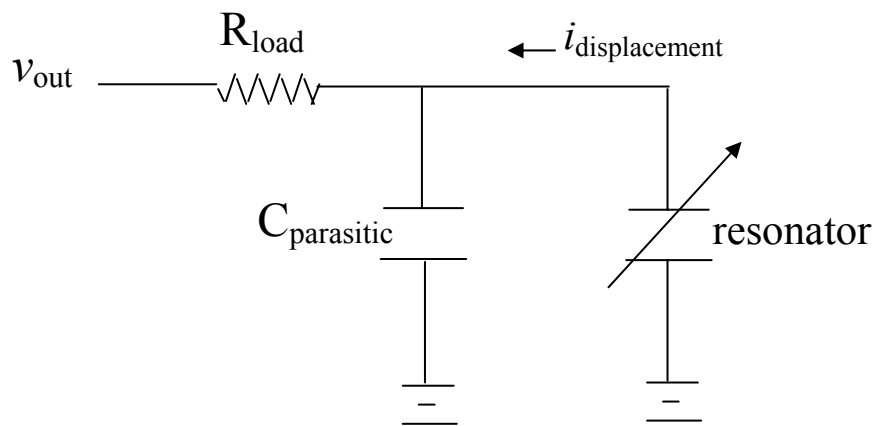


Figure 4-9: At RF frequencies, any parasitic capacitance between the resonator and the load resistance forms a path to ground and causes signal loss. By locating the first transistor of the transimpedance amplifier immediately next to the resonator, this voltage division is minimized.

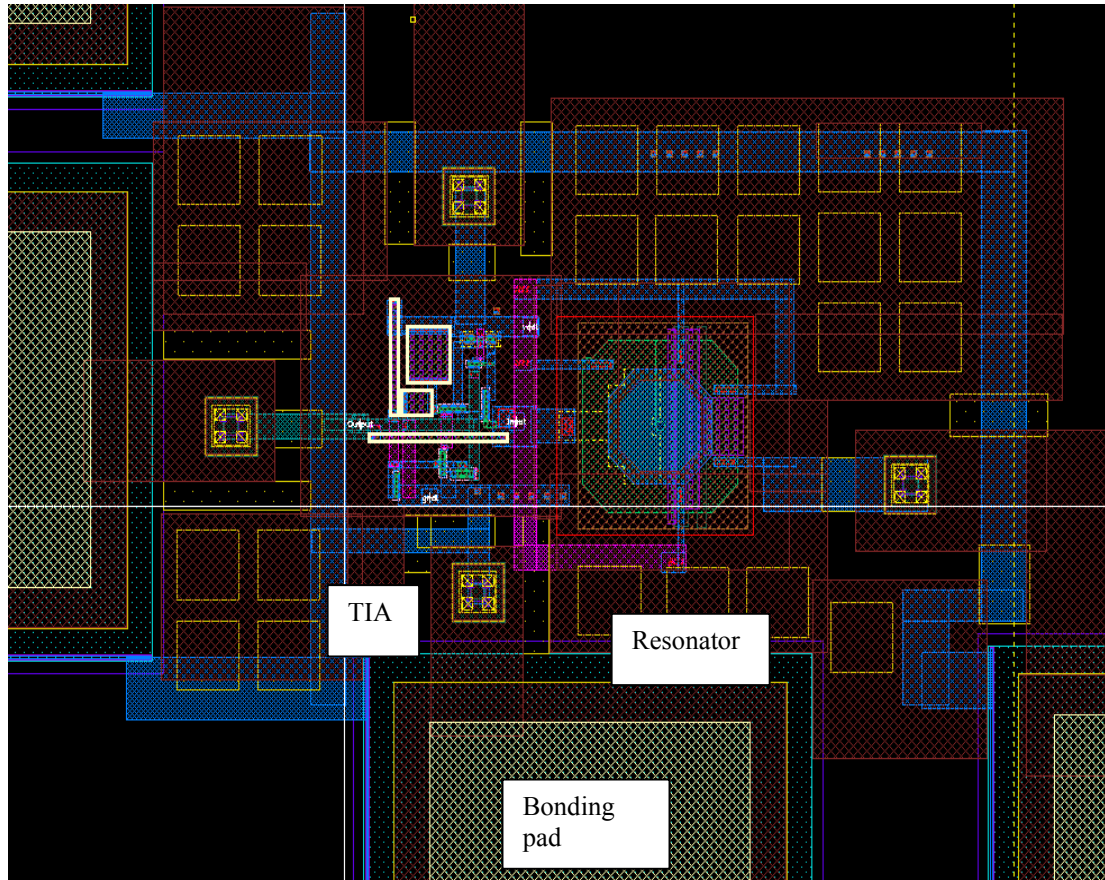


Figure 4-10: Overall layout of resonator and TIA in BiCMOS process.

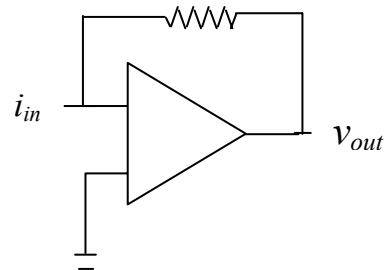
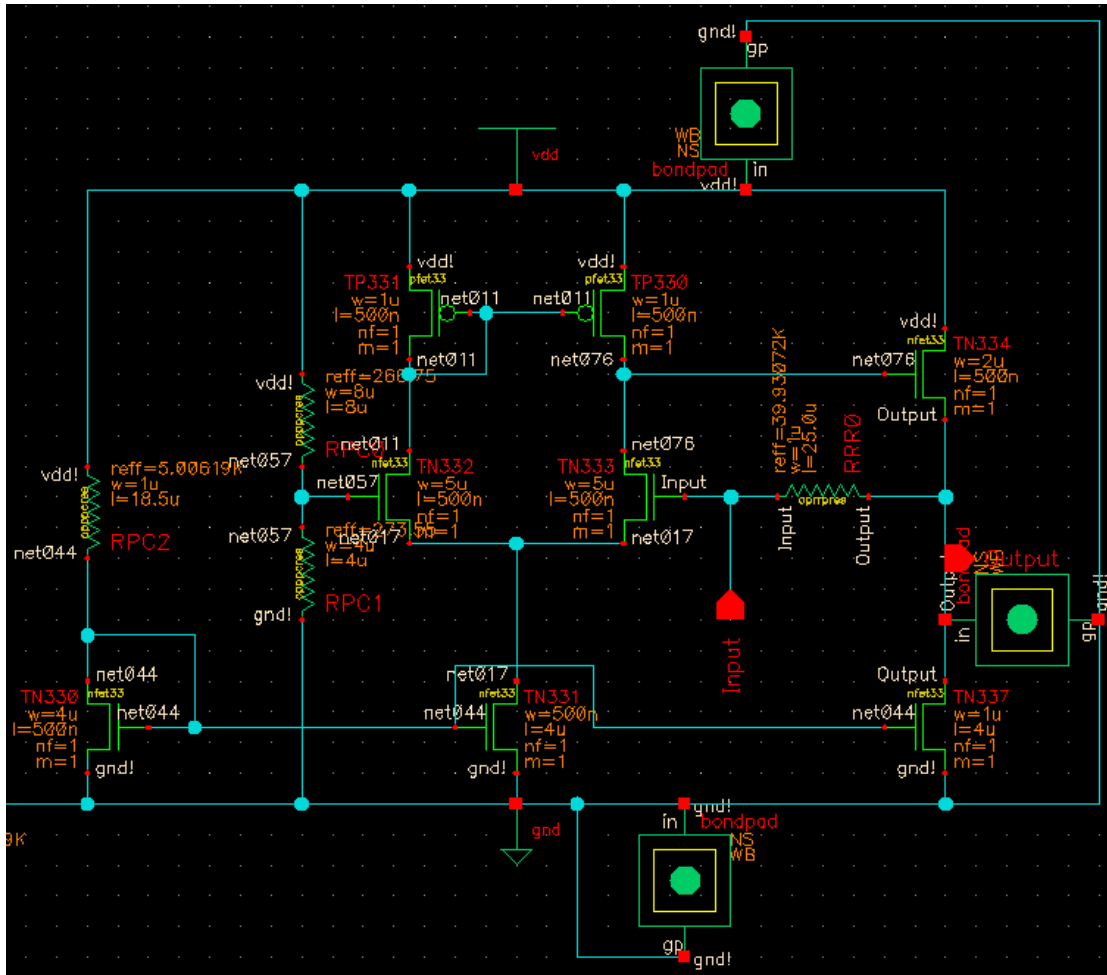


Figure 4-11: IBM BiCMOS TIA amplifier schematic with device critical dimensions.

5 Micromechanical Radio Frequency Signal Processing

Up to this point we have discussed the characteristics of the frequency dependent response of the shell type oscillator as well as how the collective transducers and resonator may be inserted into an electrical signal path to perform frequency dependent operations. We now discuss how signal operations enabled by the MEMS resonator system can work to benefit a RF communication system.

5.1 The Basic RF Communication Architecture

The fundamental attribute of a communication system is the ability to selectively sample a certain frequency bandwidth and then to demodulate the information that is received within the channel. In principle, this can be accomplished with a filter to select the frequency range of interest from the antenna signal, followed by a demodulation circuit operating at the frequency of the communication band. This architecture is seldom used for three reasons. First, the requirement for the selectivity (Q) of the front-end filter is unrealistically high. Second, demodulation at high frequencies is power consuming, expensive, and sometimes altogether impossible. Last, it is cumbersome for this architecture to change the frequency band of interest.

In 1918, Edwin Armstrong proposed the heterodyne receiver, which now forms the basis of the majority of modern RF communication architectures. The basic principle of a heterodyne receiver is to use one or more frequency translation stages to ease component specification requirements, allow band tuning, and permit demodulation to operate at lower frequencies. A basic heterodyne setup is shown in figure 5-1. The antenna converts electromagnetic energy to an electrical signal. The front end filter selects the particular communication band (i.e. from 88 to 108 MHz for

FM radio) and the signal is subsequently amplified by a LNA. A nonlinear element then multiplies the RF spectrum with a signal from a local oscillator, producing a signal at combinatorial frequencies of $\omega_{RF} \pm \omega_{LO}$. A second band pass filter is used to select the downconverted frequency, $\omega_{IF} = \omega_{RF} - \omega_{LO}$. The fact that this filter is centered at a much lower frequency allows it to have a much higher Q and thus be able to select a narrow band channel within the broader communication band. In this configuration, the frequency of the local oscillator can be tuned to choose the particular channel within the band. The heterodyne process can then be performed a second time to further refine channel selection.

A more detailed example of a CDMA PCS cellular phone heterodyne transceiver architecture is shown in figure 5-2. A single stage heterodyne architecture is used and frequency division duplexing separates the broadcast and receive signals. This figure illustrates some of the difficulties associated with this architecture, namely the large number of discrete components required. Numerous channel selecting band-pass filters must be separated from silicon electronics because the required high quality factors can only be provided by SAW or ceramic filters rather than on-chip inductor-capacitor tuned circuits. The quartz crystal is again a discrete package because of its large size and CMOS incompatibility. Finally, even mixers, which need to operate in the GHz (or multi-GHz for 3G networks), need to be on separate chips that use expensive GaAs or InP HBT technologies to operate at high frequencies. In fact, just the mixer in figure 5-3 costs \$1.21. The final package with all the components can be seen in the circuitry of a PCS cellular phone in figure 5-3. The area circled in red is the RF transceiver section of the phone, while the area in blue is mostly CMOS circuitry for electronics. In red, we can see several quartz crystals, SAW filters, a ceramic filter and several chips - altogether taking up around half of the space - presenting significant barriers in terms of manufacturing costs and

miniaturization. CMOS integrated MEMS resonators offer the possibility to integrate the functionality of these low- Q , discrete components as part of a high- Q based radio-on-chip implementation. In this section we will discuss how the micromechanical resonator with resistive transduction can serve as a filter, mixer, and oscillator for use in a heterodyne architecture.

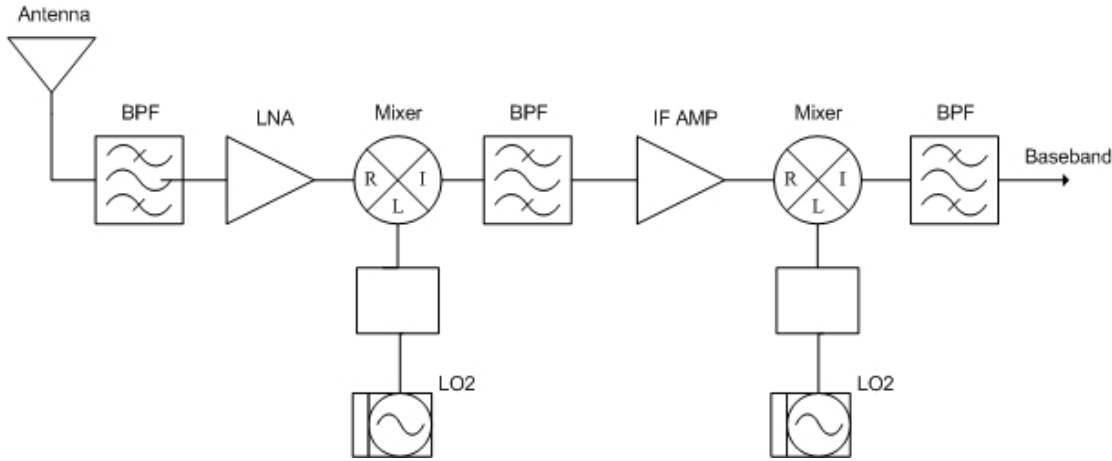


Figure 5-1: Block diagram of heterodyne receiver used for conversion between high-frequency and baseband signals.

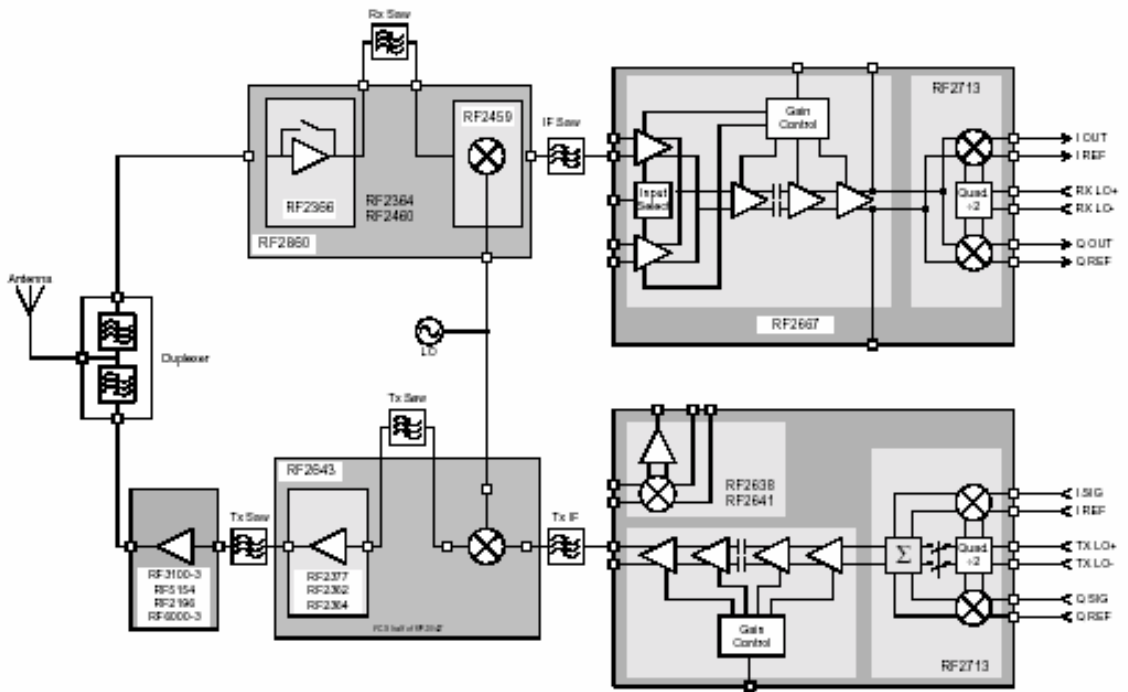


Figure 5-2: A commercial version of a CDMA PCS heterodyne architecture. Regions in gray represent single chip integrated circuits which can be purchased from manufacturers. Reproduced from www.rfmd.com.

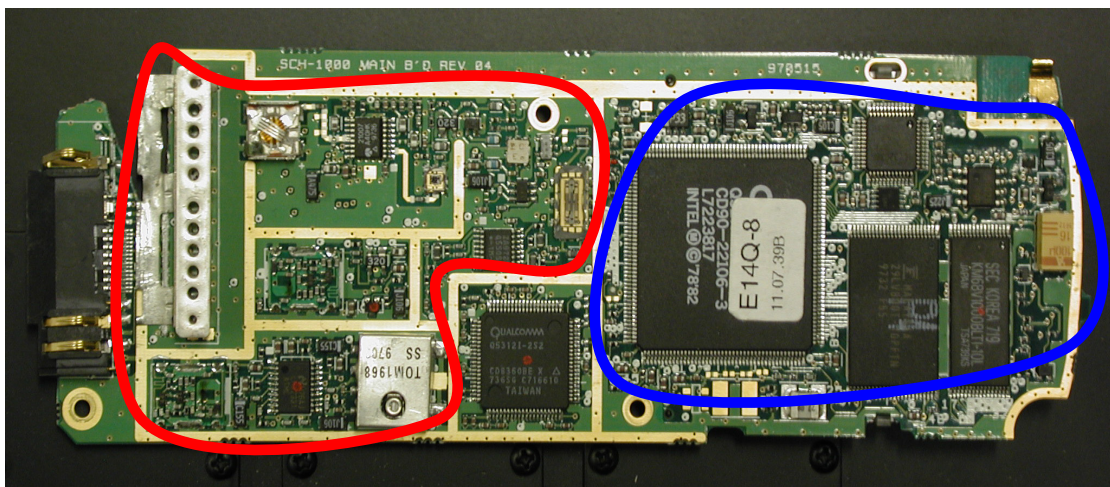


Figure 5-3: Electronics in an actual CDMA PCS cellular phone. Red circle illustrates RF communication section. Blue circle includes logic and memory electronics.

5.2 MEMS Filter

To first order, the mechanical resonator acts as a RF pass-band filter, responding with high amplitude motion on resonance and low deflection off resonance. As opposed to their low- Q electrical equivalents, the high- Q mechanical passband offers steep filter skirts, which enable rejection of close lying signals. MEMS resonators in this research are perfectly suited for IF channel selection because of their relatively low frequency and their very high Q or frequency selectivity. Scaling the mass and curvature may enable flexural resonators to reach frequencies suitable for front end filters for GHz communication bands; however, most likely, this regime will be serviced by BAW MEMS resonators.

In certain cases, the bandwidth of the mechanical passband may be too low for the application. For example, in the FM spectrum, each radio channel has a width of about 30 kHz, but a $Q = 5,000$, 100 MHz resonator has a bandwidth of 20 kHz and a $Q = 10,000$ IF MEMS filter at 10 MHz has a bandwidth of only 1 kHz. Since the mechanical passband is narrower than the data bandwidth, information is lost. This problem can be remedied in two ways. First, the metallic driving resistor, when located on the resonator, will decrease the resonator Q and open up the bandwidth. However, this reduces the slope of the filter side skirts and diminishes the attenuation of close lying neighboring signals. Furthermore, as discussed in section 3.1, adding metallic damping increases the insertion loss of the system.

A second way to increase the bandwidth is to stitch multiple resonators together to form an effective band. This process preserves the steep slope of the side skirt while extending the bandwidth. Resistive transduction is very conducive to overlapping multiple resonator bands as illustrated in Figure 5-4. An incident RF signal can be applied to a set of resonators and each resonator can be either fabricated

or controlled by the DC bias to be tuned to a slightly different frequency and overlap Lorentzian responses. The mechanical response would be detected by a piezoresistor and the individual response voltages would be summed together with an OP amplifier. This concept will hopefully be the subject of future work. An alternative approach taken by Zalalutidnov et. al.[12] is to couple resonators together in a large array, which will form a large acoustic passband when excited because of small differences in a large number of coupling structures.

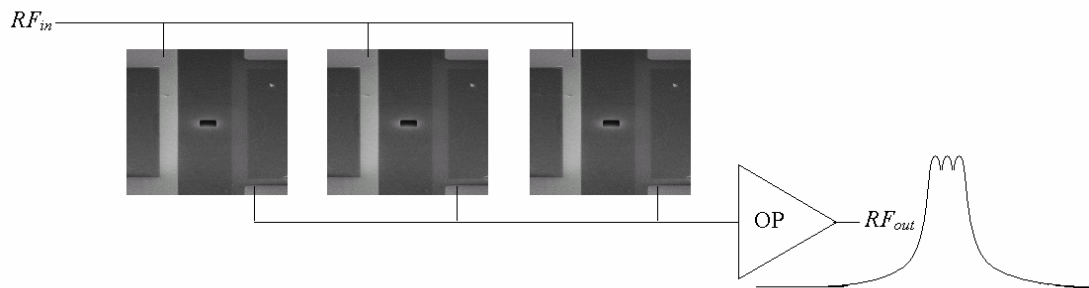


Figure 5-4: Concept for multiple order MEMS bandpass filter.

5.3 MEMS Mixer

The thermal representation of the transduction mechanism offers several inherent advantages. It reduces parasitic cross-talk between input and output signal paths and requires only microwatts of an input signal power to produce detectable mechanical motion. Additionally, signal processing based on intrinsic nonlinearity of the thermal response is possible. The fact that the range of the mechanical motion is proportional to the local temperature increase, ΔT , and hence to the square of the applied RF signal, provides the possibility for implementation as a broadband mixer.

When two voltage signals are linearly superimposed on the microheater, the resistor inherently acts as a signal multiplier, analogous to a RF mixer in a heterodyne receiver. The driving signal, V_{RF} , to the resistor can be represented as the sum of two sinusoids:

$$V_{RF} = V_{DC} + V_1 \sin(\omega_1 t) + V_2 \sin(\omega_2 t). \quad 5-1$$

Since the metal strip is in direct thermal contact with the microresonator film, the local temperature around the strip is directly proportional to the power dissipated by the resistor. We may say that temperature, and thus the driving force, follow the square of the voltage:

$$\begin{aligned} F_{MIX} &\propto \Delta T \propto V_{RF}^2 / R \\ &= (V_{DC} + V_1 \sin(\omega_1 t) + V_2 \sin(\omega_2 t))^2 / R. \end{aligned} \quad 5-2$$

Expanding (5-2) reveals, among others terms, sum and difference driving frequency components at, $\omega_1 \pm \omega_2$.

$$F_{MIX} \propto V_1 V_2 \cos[(\omega_1 \pm \omega_2)t]/R \quad 5-3$$

If the frequencies of the applied signals are chosen such that $f_1 - f_2$ matches the fundamental frequency (f_o) of the dome then appreciable mechanical motion can be observed. This enables the combinatory component to be detected through the amplitude of the mechanical vibrations while other frequency terms in the expansion, which satisfy $1/f \ll \tau_{resonator}$ and $1/f \gg \tau_{resonator}$, are filtered out. In this way, the microheater acts as a frequency converter while the resonator performs intermediate frequency (IF) filtering. Equation 5-3 illustrates that the driving force provided by the resistive mixer is DC bias independent and thus can produce an IF response in the resonator with no DC voltage on the RF or local oscillator (LO) drive signal.

Figure 5-5 a shows the experimental schematic used to study the micromechanical mixer-filter. Two CW signals from laboratory signal generators are applied to a highly linear power combiner. In the mixer setup, f_1 is the RF carrier frequency (f_c) in the GHz range, and f_2 is the LO frequency, f_{LO} , specifically chosen such that $f_c - f_{LO} = f_o$. The subsequent superposition is applied to the microresistor, which heterodynes f_c through the aforementioned process. The now translated RF energy thermally excites a 12.7 MHz resonant mode in the dome resonator and can be detected through the high- Q mechanical passband.

An ideal RF mixer has a broadband input frequency response, exhibiting a zero reflection coefficient to any input signal. From the frequency dependent input impedance for an electrostatically actuated parallel plate resonator (equation 1-22 and figure 1-6) we can see that the expression is minimized at the resonant frequency of the mechanical oscillator; however, the input impedance can be very large for off-resonance driving signals. This presents a problem from two standpoints. First, due

to the large out-of-band reflection coefficients, the input frequency range is strictly limited to that of the resonator frequency, eliminating the possibility of down-conversion from a high carrier frequency. Secondly, in order to interface with a RF 50 Ω network, an impedance matching network is needed to transform the high resonator input impedance to that of the input network. This addition causes unwanted power consumption in the low Q passive components and again limits the range of the frequency response of the actuator.

The resistive thermal actuator has the advantage that the dimensions of the resistor can be tailored such that its purely resistive impedance matches that of the input network (50 Ω); a maximum signal transfer match will then occur for any frequency of interest. As a result, input carrier frequencies may encompass a large range, not limited to the bandpass range of an input tuned network or resonator response. The microresistor used in this study is configured to be 70 μm x 3 μm x 20 nm, which presents a 45 Ω input impedance. Figure 5-6 gives the S_{11} reflection coefficient of the thermal actuator. Over a 3 GHz range, a nearly constant S_{11} amplitude of -25 dB is maintained, which translates into equal driving magnitudes over the span. Figure 5-7 demonstrates an input mixing range up to 1.5 GHz [23]. In our test setup the upper range was limited by parasitic capacitance and inductance associated with the vacuum test chamber and chipset.

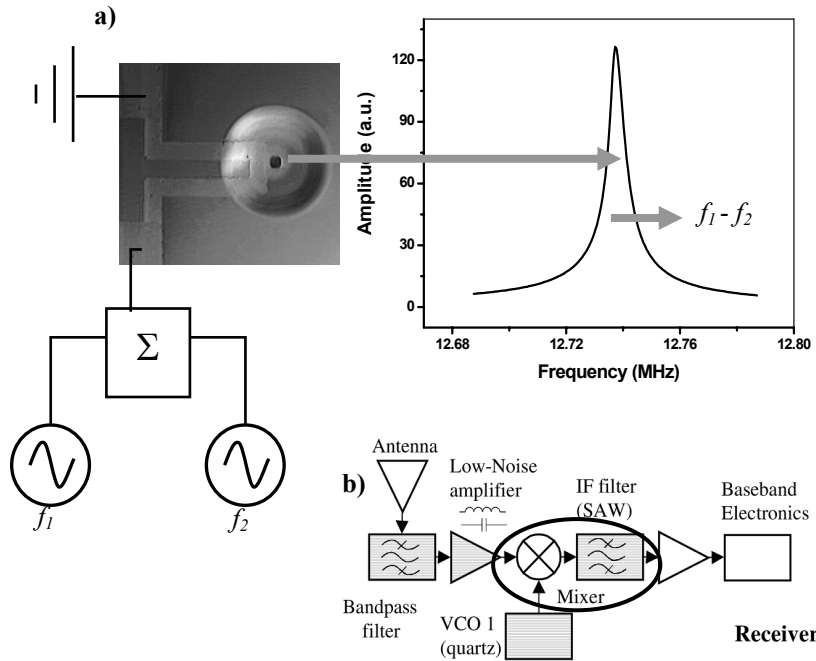


Figure 5-5: Diagram of the micromechanical mixer-filter setup where two tones at f_1 and f_2 are applied to the resistor to generate a mechanical response in the resonator at the combinatorial frequency $f_1 - f_2$. b) Schematic of a heterodyne receiver. Circled area indicates the circuit analogy of the MEMS mixer-filter presented in (a).

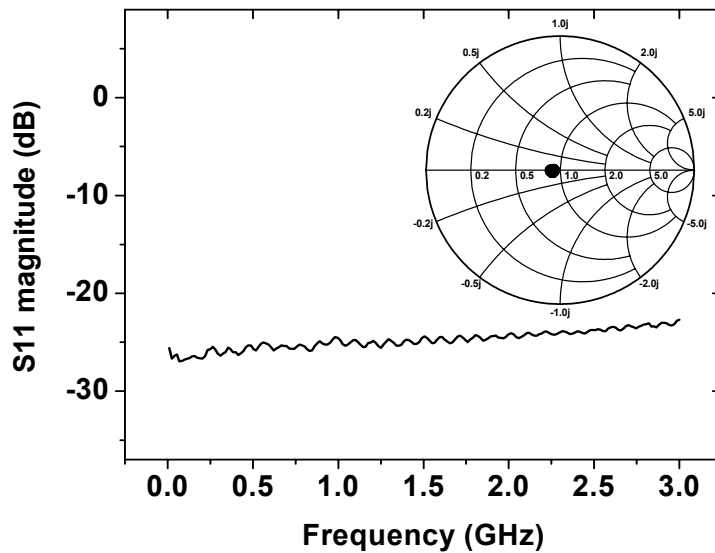


Figure 5-6: S₁₁ reflection coefficient of the 45 Ω resistive actuator.

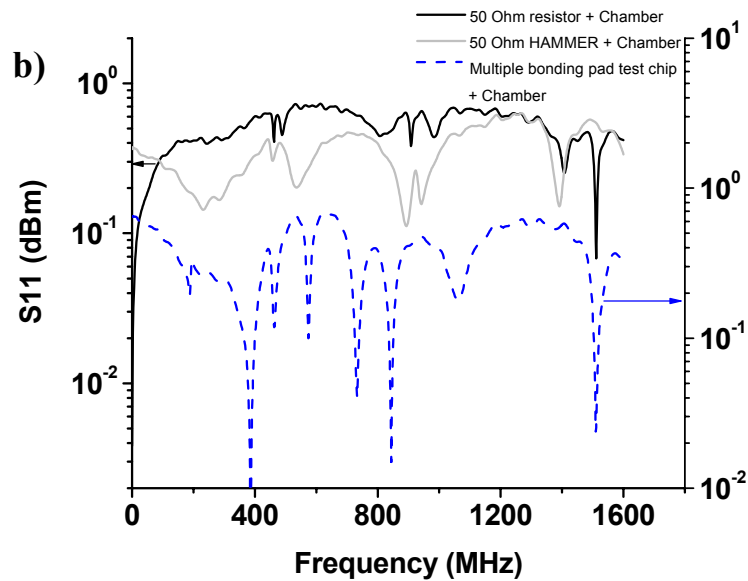
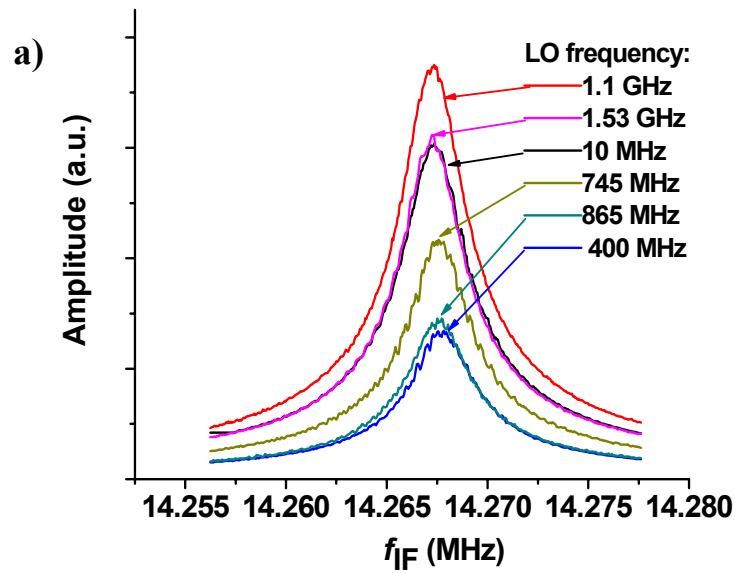


Figure 5-7: a) Output response of MEMS mixer at the intermediate frequency $f_{LO} - f_{RF} = f_o$ over a 1.5 GHz range of input LO and RF frequencies. Variations in the peak amplitude are the result of an attenuated RF drive signal caused by partial reflection from test chamber and bonding pad paracitics in the multiple resonator and bonding pad test chip. Good agreement is found between the S_{11} input reflection measurement of a single 50 Ω MEMS and a 50 Ω resistor.

5.4 MEMS RF Radio Receiver

To demonstrate the potential of the resistor/dome transduction method, a heterodyne FM receiver was built and tested using the MEMS device as a one-step down conversion mixer and IF filter. The setup is described in figure 5-8. The local FM station spectrum was received by an antenna and amplified. Using a linear power splitter, the FM spectrum was superimposed on a tunable reference local oscillator and applied to the microheater. In order to listen to 91.7 MHz (Ithaca WICB) we chose the local oscillator to be

$$f_{LO} = 91.7\text{MHz} - 2\pi\omega_o = 77.48\text{MHz} \quad 5-4$$

centering the 100 kHz bandwidth of the FM radio station in the vicinity of the resonance of the dome. The mechanical response of the dome resonator (the IF signal) was detected interferometrically and the photodetector signal was applied to a spectrum analyzer for demodulation. Demodulation of the FM signal can be performed in one of two ways. First, direct frequency demodulation can be used; however, since the passband ($Q=3,000$) of the dome resonator is much narrower than the bandwidth of the radio station, considerable information is lost, and only distorted audio can be discerned, even with fine tuning of the LO. To overcome this problem, the LO is slightly detuned and the slope of the mechanical resonance passband is used to convert FM modulation to AM modulation, which is subsequently demodulated. The mechanical passband could also be widened by placing the actuation resistor in a position where larger dissipation in the metal would occur, deliberately decreasing the device Q .

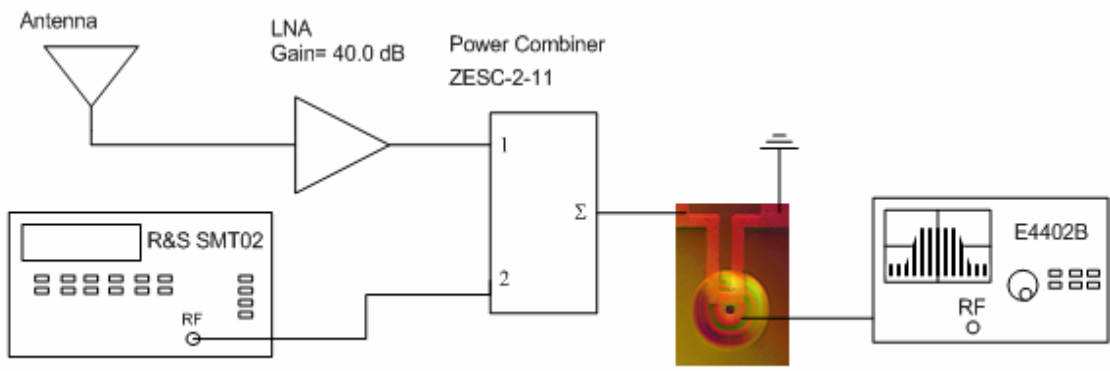


Figure 5-8: Block diagram of the MEMS FM radio receiver.

5.5 MEMS Oscillator

By applying the signal that is proportional to displacement signal from the output transducer as feedback onto the input transducer, the micromechanical dome resonator can function as a stable frequency source. Figure 5-9 shows a schematic for this mode of operation, which was employed with both laser detection and piezoresistive detection. In the interferometer case, the photodetector signal, representing the mechanical motion of the resonator, is first amplified by about 50 dB, depending on the intensity of the detection laser. To select one of the resonator modes of vibration and to provide adjustable in-loop phase, the feedback signal is filtered by either a Telonic Berkeley Inc. or a Lorch Microwave, low- Q , tunable band pass element. By inserting these filters into the feedback loop, they contribute their own frequency dependent phase shift (i.e. figure 1-5), thus allowing the phase at a particular frequency to be varied by changing the filter center frequency. A DC bias less than 1 V is superimposed on the feedback signal and subsequently applied to the driving resistor. Limit-cycle oscillations at the free-running frequency, f_{FR} , will grow out of the unstable equilibrium point of the system when the feedback network is tuned to provide a gain greater than 1 with a phase shift of an integer multiple of 2π (called the Barkhausen Criterion). The feedback phase does not necessarily need to be an integer multiple; however the in-phase component must be larger than the out-of-phase component.

Feedback in the harmonic oscillator can be modeled with a non-conservative coupled set of equations:

$$d^2x/dt^2 + \frac{\omega_o}{Q} dx/dt + \omega_o^2 x = dy \quad 5-5$$

$$\frac{dy}{dt} + ky = \Gamma x \quad 5-6$$

where d/Γ is the feedback gain, and the differential equation in (5-6) accommodates for phase tuning in the controller. Since we know the solution will be of the form

$$x = R \cos(\omega t) \quad 5-7$$

$$y = A \cos(\omega t) + B \sin(\omega t) \quad 5-8$$

we can use the harmonic balance method and disregard the higher order harmonics, to solve for the frequency, ω , the amplitude, R , of the limit cycle oscillation.

$$\omega^2 = -k^2 - \frac{d\Gamma Q}{\omega_o} \quad 5-9$$

$$R^2 = -\frac{4Q}{3\omega_o\beta} \left(\frac{\omega_o}{Q} k^2 + \left(\frac{\omega_o}{Q} \right)^2 k + d\Gamma + \frac{\omega_o^3}{Q} \right) \quad 5-10$$

And the coefficients A and B are given by

$$A = -\frac{k\omega_o}{Qd} R \quad B = -\frac{\omega_o}{Qd} R \omega \quad 5-11$$

The amplitude of the limit cycle oscillation is either determined by the nonlinearity of the mechanical resonator or limited by the voltage range of the sustaining amplifier. To achieve the best performance, we saturate the output of the

amplifiers with a feedback driving signal that will keep the resonator out of the strongly non-linear vibration regime.

The highest frequency resonator that was successfully placed in a laser detection feedback loop was a 5 μm radius plate with a mode at 115 MHz (figure 5-10). To measure the temporal stability of the frequency generator, a frequency counter was connected to the output of the resonator and the standard deviation δf of the center frequency variations was measured. Short-term stability, $\delta f/f \sim 1.5$ ppm (figure 5-11 a), was demonstrated at 14.5 MHz for the 30 μm resonator. Phase noise (figure 5-11 b) of the same mode was measured to be -80 dBc/Hz at a 1 kHz offset. Our measurements indicate that the value of the phase noise was determined by the high noise floor of the detection and sustaining circuitry. Phase noise measurements performed using interferometric detection are extremely difficult due to the DC heating effects which cause frequency instability which will artificially increase the phase noise of the resonator.

Feedback was also placed between piezoresistive detection and resistive drive to achieve self-sustaining oscillations. Long-term frequency stability was much more reliable in this case because DC heating effects, usually present from the HeNe laser, were removed from the system. Since the Wheatstone Bridge and integrated amplifier provide a sufficient signal to noise ratio of the resonator at 10 MHz, we can detect the mechanical motion at the frequency of vibration, as opposed to heterodyne detection [44], which allows the resonator to lock onto its own mechanical motion via the feedback loop. Feedback is provided outside the vacuum chamber by means of a MATEC tuned receiver, again allowing control of loop phase and amplitude. Mechanical oscillation at 9.8 MHz was achieved with approximately 20 dB of loop gain (not including the preamplifier gain) and is pictured in figure 5-12. The spectrum was measured with a 10 Hz resolution bandwidth using an Agilent 4396B spectrum

analyzer after the feedback gain. To convert this to a 1 Hz resolution bandwidth (to conform with measurement standards) 10 dB was subtracted from each point to compensate for averaging across a 10 Hz bandwidth, except for the peak point where an average power measurement would not apply. With a 1 Hz bandwidth, the phase noise at 5 kHz away from the carrier is about -70 dB below the carrier (dBc), much higher than standard quartz crystal oscillators at 10 MHz that routinely achieve better than -120 dBc/Hz phase noise at a similar frequency offset. However, when we turn off the resonator (by decreasing the bridge bias point to 0 V) the noise floor remains at the -70 dB figure. Evidently, the unshielded gold bonding wires used to connect the resonator to the OP amplifier and power supplies are particularly susceptible to electrostatic coupling effects that define the noise floor of the system. Thus, since the noise floor was determined by the feedback loop, phase noise measurements of the MEMS oscillator could not be carried out until further integration is completed.

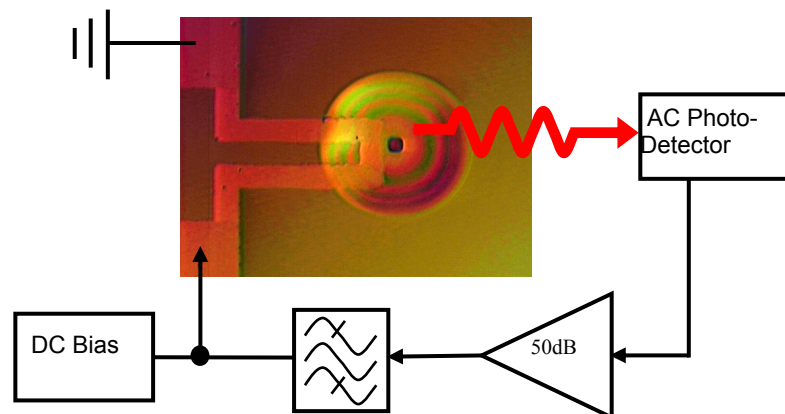


Figure 5-9: Schematic of feedback network of the dome oscillator

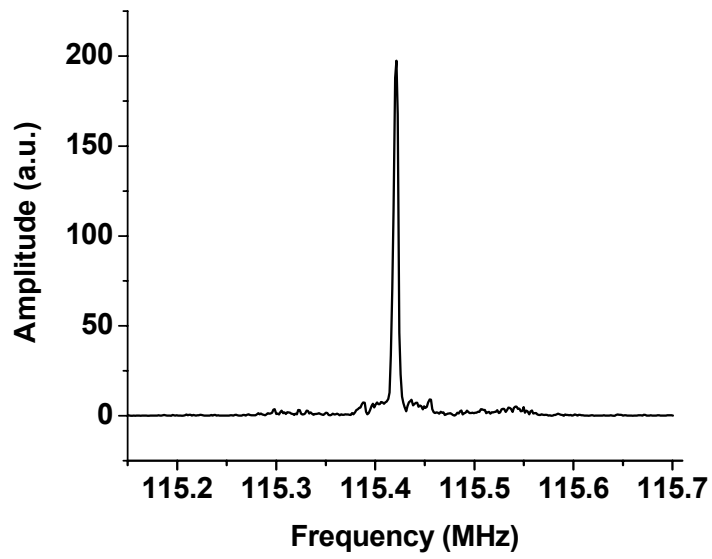


Figure 5-10: Experimental spectrum of dome oscillations with interferometer detected feedback.

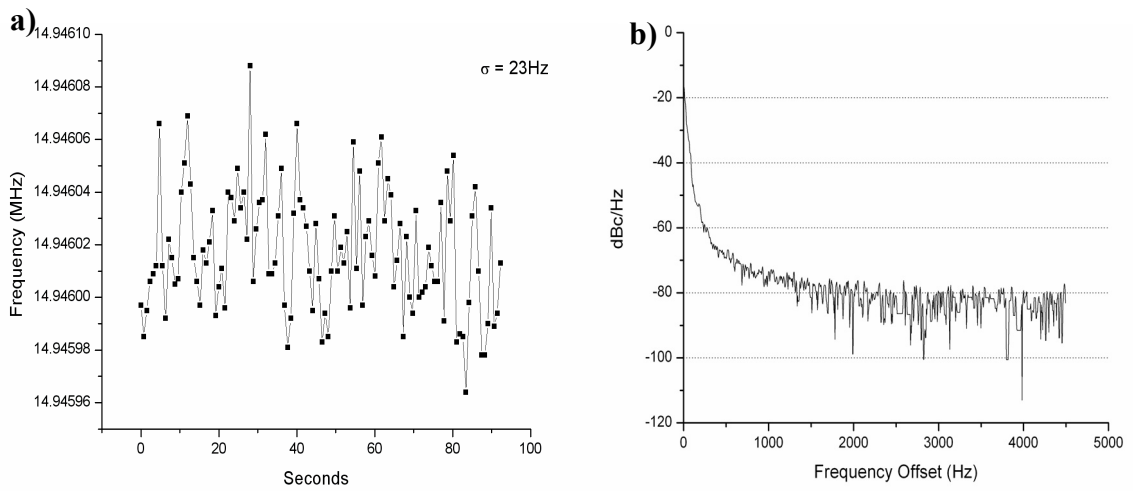


Figure 5-11: Short term stability (a) and phase noise (b) in a $30 \mu\text{m}$ dome oscillator.

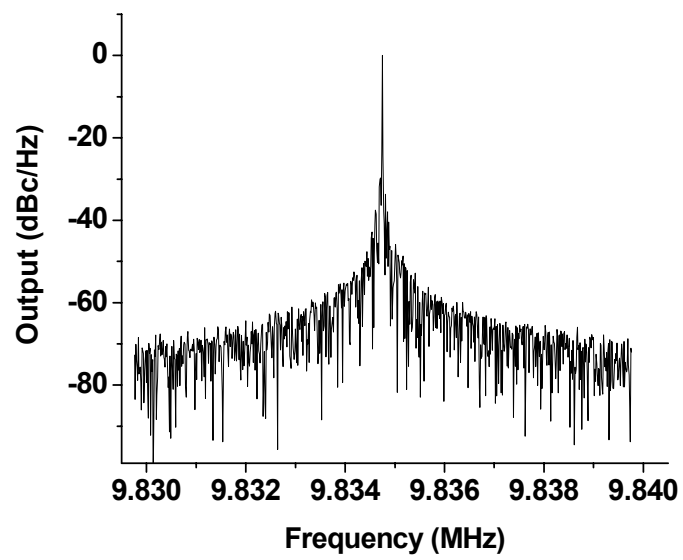


Figure 5-12: Feedback spectrum from piezoresistive oscillator sampled after the tuned feedback amplifier.

5.6 Voltage Controlled MEMS Oscillator

The resonant frequency, f_o , of the dome oscillator can be tuned by changing the amount of heat dissipated into the polysilicon film. As discussed in section 3.3, steady-state heat, imposed either by the HeNe detection laser or by a DC bias on the thermal actuator, will cause a change in resonator stiffness, changing the natural frequency of the shell resonator. Depending on the location of the heat source and the sensitivity of the effective spring constant of a shell resonant mode to thermal expansion, the frequency of oscillation can be tuned. In (Figure 5-13) a tuning range of 0.35% over a 1V change in DC bias is shown for a dome resonator placed in a feedback loop.

Frequency modulation of the oscillator's free running frequency can be achieved by applying a baseband AC signal that, with its proportional slow varying heat dissipation, will alter the resonator's fundamental frequency. The low-frequency bias causes f_o to change, creating a carrier frequency, f_{FR} , which is modulated at the rate of the baseband signal on the heating mechanism. The depth of the modulation superimposed on the carrier is defined by the Hz/Volt transfer function of the actuator and resonator mode. To eliminate adder circuitry and achieve better isolation between the baseband signal and the carrier signal, the baseband signal can be applied to a second resistive actuator (figure 5-14). Using this setup, frequency modulation of a 26 MHz carrier by a 30 kHz baseband signal was demonstrated with a modulation depth of 15 kHz. A spectrum analyzer with a high video bandwidth, centered on the carrier frequency, was used to demodulate the carrier.

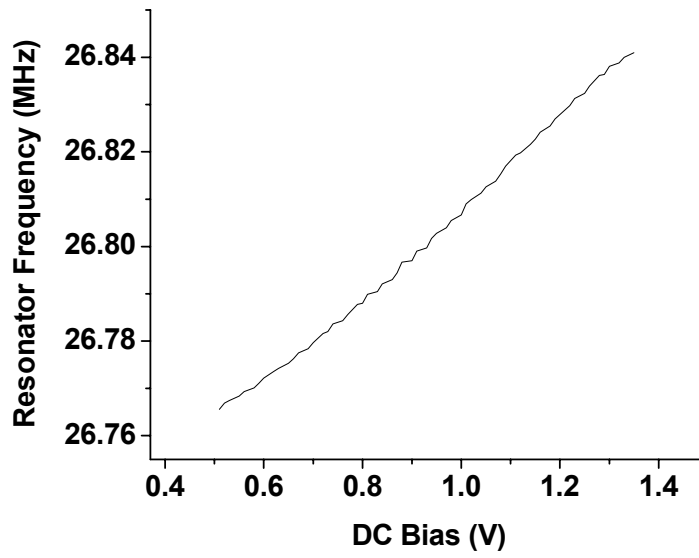


Figure 5-13: Frequency tuning of a dome oscillator (feedback amplitude = 380mV). One resistor is used to close the feedback loop while a 2nd resistor alters stress in the shell through an applied DC bias, changing f_o .

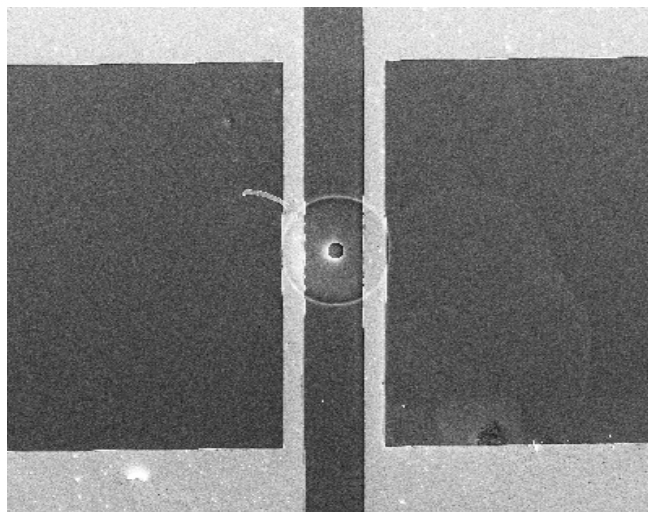


Figure 5-14: SEM image of the dome resonator and actuator. Circular charged ring shows the lateral dimension of the 30 μm diameter shell-type resonator. Two gold resistors are defined vertically along the periphery of the resonator, forming two electrically isolated actuators.

5.7 Phase Tunable MEMS Emitter

It is well known that a weakly non-linear self-oscillatory system can be synchronized to a periodic force superimposed on the system, provided that the natural frequency and the perturbation frequency are not far apart [59]. In the 17th century, the Dutch scientist Huygens, while bed-ridden by an illness, noticed that the periodic motion of pendulums in two wall mounted clocks became synchronized if the clocks were hung close to each other. He postulated that mechanical vibrations were coupled through the wall which drove the clocks into synchronization. In the early 1920s and 30s the Dutch engineer, Van der Pol, found that vacuum tube circuits had stable limit cycle oscillations due to their nonlinear negative resistance. When these circuits were driven with a signal whose frequency is near that of the limit cycle, the resulting periodic response shifts its frequency to that of the driving signal. That is to say, the circuit becomes entrained or locked to the driving signal.

Previous research by Zalalutdinov et. al. [60] demonstrated that limit cycle oscillations (in the absence of external forcing) in a micromechanical resonator could be locked in frequency and phase to a small perturbation or pilot signal, f_{pilot} , which was superimposed on the resonator via a modulated laser. Following this work, this section demonstrates injection locking of the MEMS oscillator with a thermally induced pilot signal applied to the microheater (figure 5-16). A map showing the regions of capture and loss of entrainment of the dome oscillator is shown in figure 5-15. To create this plot, positive feedback is applied to one resistor, causing self-generation at frequency f_{FR} . A pilot signal, used to entrain the oscillator, is then applied to a second resistor on a completely isolated signal path. The pilot signal is swept in frequency to establish the region where the mechanical oscillator is entrained. Within the region of entrainment, the resonator oscillations take on the frequency

stability of the pilot signal. Hysteretic behavior can be seen between the points where lock is lost (the pull out frequency) on the upward pilot sweep and where lock is resumed on the downward sweep. The perturbation is then incremented in amplitude, which serves to broaden the entrainment region.

Following Van der Pol, Adler [61] developed a theory in a similar resonating electrical circuit that has been extensively used [62, 63] to study non-linear behavior. Adler considered a LCR tank circuit under feedback to which an injected signal could be added. He found that the behavior of the system under feedback and injection could be described by

$$\frac{d\alpha}{dt} = -\frac{V_{pilot}}{V_{feedback}} \frac{\omega_o}{2Q} \sin \alpha + \omega_0 - \omega_{pilot} \quad 5-12$$

where α is the phase difference between the injected signal and the free-running signal, and thus $d\alpha/dt$ is the beat frequency between f_{pilot} and f_{FR} . Since we are interested in the case where the resonator is locked to the pilot, $d\alpha/dt=0$, the phase difference under synchronization is

$$\alpha = \sin^{-1} \left(\frac{2Q \cdot V_{feedback}}{\omega_o \cdot V_{pilot}} (\omega_0 - \omega_{pilot}) \right). \quad 5-13$$

This can be qualitatively seen in figure 5-17 where the amplitude and phase response of a conceptual oscillator from equation 1-1 is illustrated. When the resonator is oscillating at its fundamental frequency ($f_{FR} = f_o$)(the red line) the mechanical response will be phase shifted by $\alpha = -90^\circ$ with respect to the pilot signal. When an injected signal is detuned by some amount (the green line) and the system is

still in lock, the phase of the mechanical vibrations is now going to be either lagging or leading the phase of the impressed signal.

Phase tuning was also demonstrated in the MEMS resonator. By detuning the pilot signal superimposed on a resonator away from the unperturbed membrane resonant frequency, a phase difference is produced between the tank feedback and the pilot signal that, just as in Adler's case, is related to the difference between f_o and f_{pilot} . This is interesting; however, phase lag is produced at the expense of changing the pilot frequency, which is a cumbersome requirement. Alternatively, phase lag in the entrained MEMS resonator is induced by detuning the fundamental frequency of the resonator, f_o , with a DC bias. Changing f_o moves the entrainment "V" relative to the pilot signal instead of the opposite situation that was used to measure the entrainment map. As illustrated in figure 5-17 b, to maintain frequency synchronization, the phase of the mechanical vibrations changes according to the phase-frequency function of the resonator. This phase change can be measured between the pilot signal and the self-generation feedback signal. Thus, a phase difference can be obtained by simply changing the magnitude of the voltage impressed on the oscillator rather than by requiring a complex method of changing the pilot signal frequency. Furthermore, by changing f_o and not f_{pilot} , the output phase can be tuned while f_{FR} remains unchanged. Figure 5-18 demonstrates that the total phase shift between f_{FR} and f_{pilot} was controlled by as much as 200° . Beyond this region of DC bias tuning, the region of the entrainment V is shifted to the extent that the oscillator will lose the lock on the pilot signal, and the entrained condition required to produce the phase differential will collapse, producing quasiperiodic motion. Higher phase differentials could be produced with stronger pilot signals; however, more robust actuators will be needed since gold resistors of this dimension will melt when subjected to much more than 1 V DC.

A voltage controlled phase tunable emitter would be valuable for several applications. Since there is tunable phase lag between the input (pilot signal) and the output (oscillator output), the system can be used to delay incoming signals. MEMS have been employed for such a purpose before [64]; however, these operate on the principle of using MEMS switches to insert delay producing transmission lines, which offers only discrete phase adjustments and can be very space consuming.

The entrained oscillator can also produce a phase modulated carrier signal for use in communication systems. Phase modulation is demonstrated by superimposing a baseband AC signal onto the pilot resistor while the resonator is self-generating and entrained by the pilot signal. Figure 5-19 demonstrates the experimental schematic. The right microheater applies positive feedback from the photodetector while the left microheater is used to entrain the resonator with the pilot as well as supply an AC baseband signal. The time varying baseband signal, through the additional heat dissipated in the resistive actuator, pulls the natural mechanical frequency across the pilot frequency. Detuning the resonator causes a time varying phase difference between the pilot signal and the feedback signal that is proportional to the time varying baseband amplitude. The phase modulated carrier signal can be sampled from the oscillator feedback with an I/Q demodulator. Phase modulation of a 26 MHz carrier by a 20 kHz baseband signal was demonstrated with a modulation depth of 160° (figure 5-20).

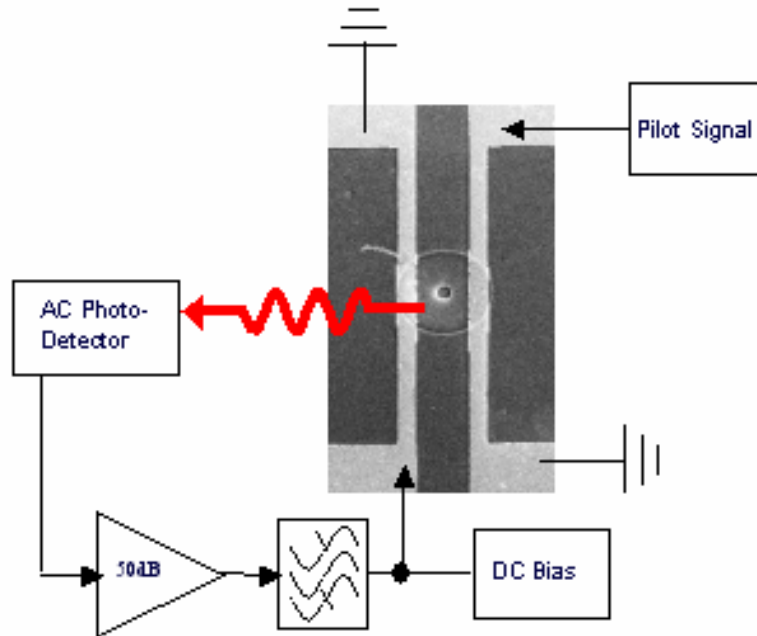


Figure 5-15: Setup to demonstrate entrainment in MEMS oscillator. Left resistor is used for the feedback loop and right resistor is used to provide the coupling mechanism in the form of an electrical signal from a pilot oscillator.

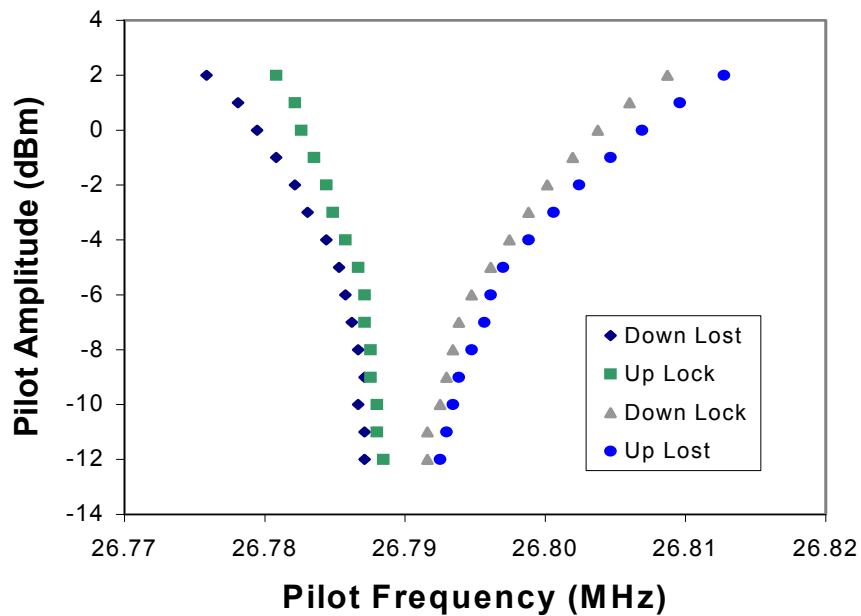


Figure 5-16: Region of entrainment of a self-generating mechanical oscillator (feedback = 380mV RMS, pilot DC bias = 700mV). Hysteresis is shown between the upward and downward sweeps of the pilot signal.

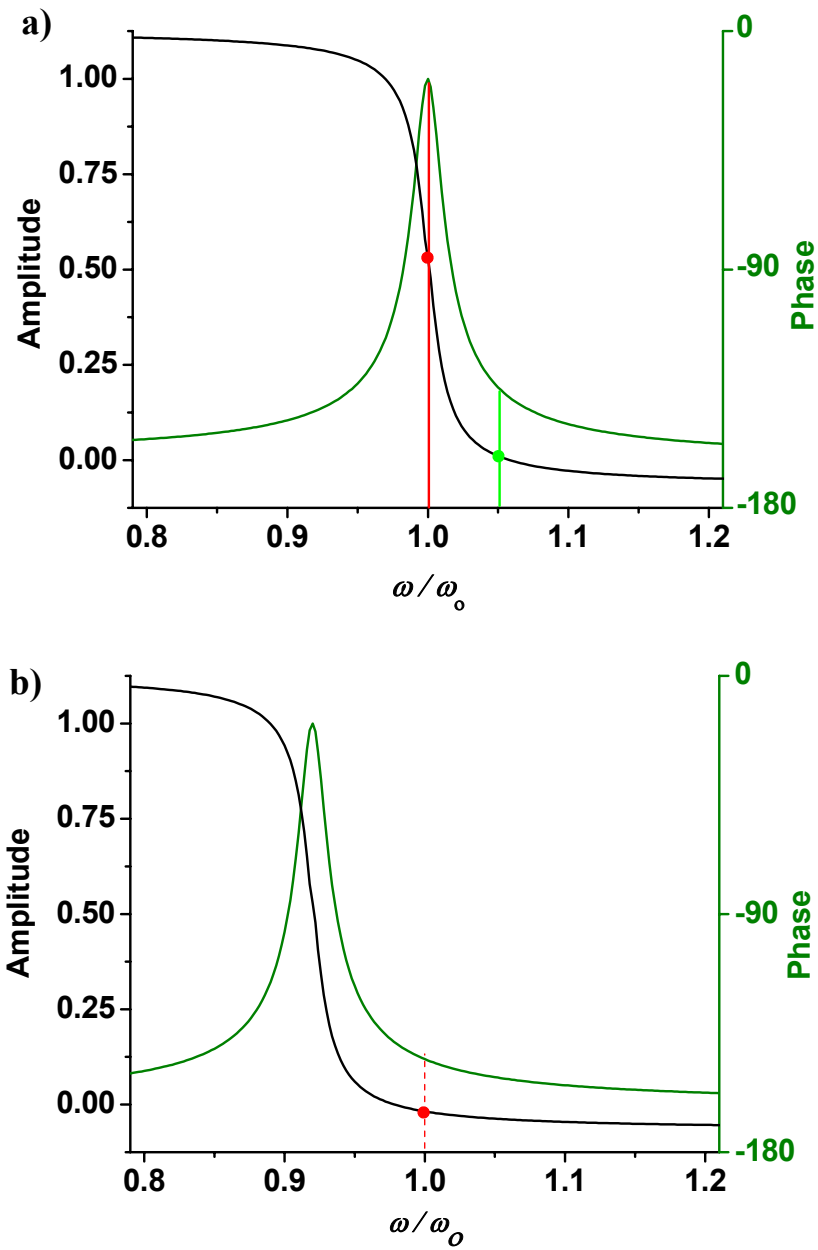


Figure 5-17: a) Phase lag corresponding to pilot signals at two separate frequencies. b) Phase lag produced from fixed pilot and tuning the natural frequency of resonance.

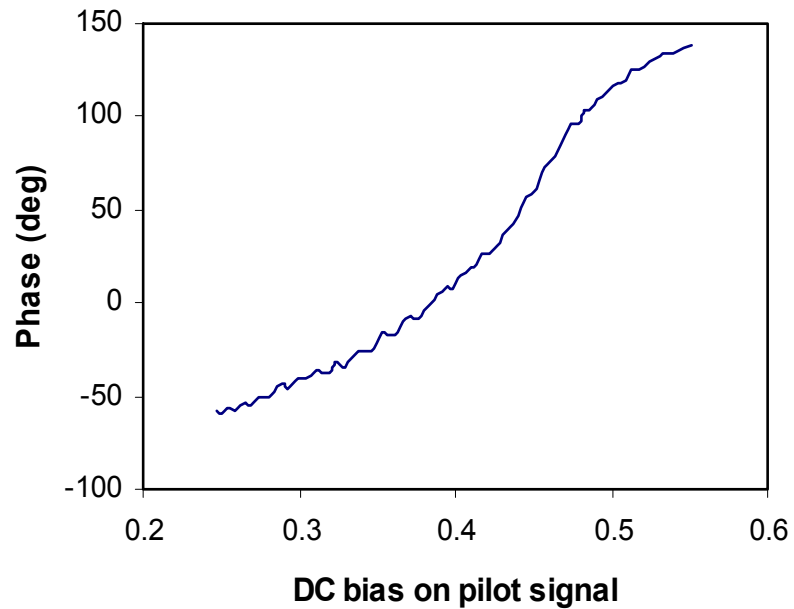


Figure 5-18: Phase difference between f_{FR} and f_{pilot} in an entrained oscillator as f_o is detuned by DC bias (feedback = 380mV RMS, pilot = -10dBm, $f_{pilot} = f_{FR} = 26.79$ MHz).

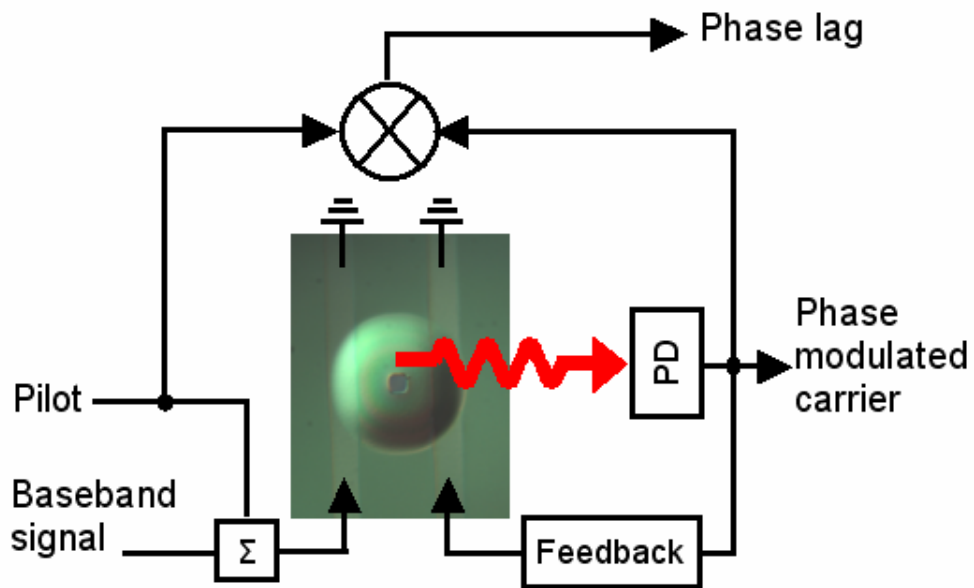


Figure 5-19: Setup for MEMS phase shifter and modulator. The right resistor is used in the feedback loop and the left resistor is used for the pilot signal and baseband signal.

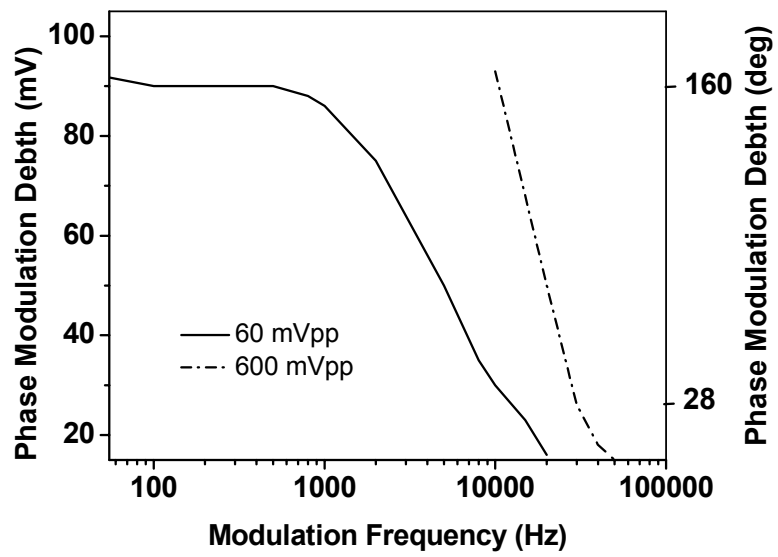


Figure 5-20: PM speed versus PM depth for a 26 MHz, injection locked MEMS resonator. Red and Black lines illustrate different baseband signal strengths.

6 Nonlinear Dynamics of MEMS Resonators

6.1 Non-Linear Effects in Communications

We have studied applications of the MEMS resonator in both the linear and non-linear regime, but it is also necessary to understand how the mechanical resonator behaves under strong excitation and what effect this will have on our mechanical circuit elements. By adopting a “black box” approach, the nonlinearity of any device can be expressed in terms of a polynomial dependence [65]:

$$U_{OUT} = \alpha_0 + \alpha_1 U_{IN} + \alpha_2 U_{IN}^2 + \alpha_3 U_{IN}^3 + \dots, \quad 6-1$$

where U_{IN} and U_{OUT} are input and output signals respectively. RF devices that exhibit a substantial cubic term, α_3 , are prone to a phenomenon known as 3rd order intermodulation (IM₃). When two strong out-of-band interferers are applied to the input of such a device at frequencies $f_1=f_c+\Delta f$ and $f_2=f_c+2\Delta f$, the cubic power component, α_3 , will produce a term, U_{IM3} , overlapping with U_{IN} . Substituting $U_{IN} = U_i(\sin(\omega+\Delta\omega)+\sin(\omega+2\Delta\omega))$ into (6-1), we find, among other terms, a third order term:

$$U_{IM3} = \alpha_3 U_i^3 \sin[(2\omega_1 - \omega_2)t] = \alpha_3 U_i^3 \sin(\omega_c t) \quad 6-2$$

The presence of IM₃ can greatly deteriorate the performance of the device by folding strong out-of-band interferers into the band, which is a primary concern in the design of RF mixers, filters, and amplifiers.

6.2 Resonator Non-Linear Effects

We will show that our thermal mixer can be viewed, in terms of (6-1), as ideal since its output signal—a temperature, further converted into a force—is an exactly quadratic function of the applied voltage. In other words, for realistic input power ranges, the nonlinearities of the metal-film resistor are negligible; however under the presence of large excitation forces, the mechanical mixer-filter (the dome resonator) can exhibit nonlinear behavior.

The response of a mechanical resonator to a strong sinusoidal excitation can be calculated using Duffing's equation [66],

$$\frac{d^2x}{dt^2} + \frac{\omega_o}{Q} \frac{dx}{dt} + (\omega_o^2 - \beta x^2)x = F \sin(\omega t), \quad 6-3$$

which takes into account a nonlinear term β in the resonator spring constant and where x is the displacement around the equilibrium position of the membrane. The presence of β distorts the resonance curve of the dome at large driving amplitudes (figure 6-1, 6-2) and thus can produce a significant α_3 term in (6-1). Since our mixer and filter are inseparable, we must characterize the nonlinearity of the entire device, i.e., mixer-filter combination.

Typically, the magnitude of β is quantified by solving (6-3) to determine the relationship between the amplitude of oscillation and the deviation from the resonant frequency in the linear regime. However, in the case of MEMS, we do not have a precise method for determining the absolute amplitude of the mechanical vibrations. To estimate the displacement of the resonator, the modulation of the reflectivity of the built-in Fabry-Perot interferometer, as a function of the gap, can be calibrated to the mechanical motion by using large displacement MEMS structures [67]. For

displacements larger than $\lambda/4$, the reflectance signal will depart from its sinusoidal shape and take on a frequency-doubling characteristic due to movement through interferometric fringes. This allows a fit of the photodetector signal to obtain the value of the mechanical motion. We can use the calibrated laser power (2.25 mW) to measure the modulation of the reflectivity at the apex of the shell resonator and estimate a mechanical amplitude of 1 nm produced by a -10 dBm resistive driving signal. The shallow curvature of the device enables us to ensure that the linear portion of the sinusoidal interferometric reflectance pattern (also the region of deepest modulation) occurs at the unperturbed gap distance by scanning the detection laser ($\lambda = 633\text{nm}$) across the resonator to optimize for the largest magnitude AC signal. The peak-to-peak range of motion is less than 1 % of the $\lambda/2$ reflection pattern period; therefore the photodetector representation of the mechanical motion can be approximated as linear.

An alternate method to quantify the severity of nonlinearities, which does not require information about mechanical amplitude, is to analyze effects, such as IM_3 , produced by the presence of a 3rd order term. To quantify IM_3 , a special parameter, the third order intercept point (IIP_3), is widely used. IIP_3 is essentially an input power, P_{IIP_3} , that interfering signals at frequencies f_1 and f_2 would have to impose in order to produce an output signal at a carrier frequency, f_c , that would be as large as the result of applying the same P_{IIP_3} power input directly at a carrier frequency. Later we will show that IM_3 caused by the resonator can be predicted by solving a modified version of (6-3).

IM_3 in micromechanical structures has been previously measured for electrostatic force based resonators. Navid et. al. [68], find an IIP_3 at $\Delta f = 200$ kHz of -3 dBm for a $f_o = 10$ MHz clamped-clamped beam micromechanical resonator implemented as a frequency filter. They find that the electrostatic actuator is the

primary source of intermodulation distortion due to the inverse relationship between the parallel plate capacitance and the gap spacing and is limited by the trade-off between linearity and series motion resistance. To reduce the motional resistance of the capacitive actuator without impacting the linearity of the device, the electrode gaps could be filled with a high- κ dielectric material [69] but this would affect the mechanical quality factor. Kaajakari et. al. [70] also examine capacitively induced non-linearities and similarly conclude that, due to distortion in the motional current in an electrostatic MEMS actuator, even linear vibrations can result in harmonic distortion.

Figure 6-3 demonstrates the experimental setup for measuring IIP_3 in our MEMS mixer-filter. Three signals (f_{LO} , f_1 , and f_2) from external signal sources are linearly superimposed with a power combiner ($IIP_3 > 50$ dB). The local oscillator (f_{LO}) in the mixer implementation is a 60 MHz, 0 dB signal. The carrier frequency, f_c , in the setup is $f_o + f_{LO}$, which, for a 12.7 MHz mode in the dome resonator, is chosen to be 72.7 MHz. The test signals (f_1 and f_2) are located at $f_c + \Delta f$ and $f_c + 2\Delta f$ respectively. The signal is then applied to the microheater and IM_3 products are produced at f_o .

Intermodulation was measured at offsets (Δf) between 20 kHz and 500 kHz. Beyond 500 kHz, mechanical attenuation outside the passband of the resonator reduces the magnitude of the interferers and produces very little intermodulation. Figure 6-4 plots the output response of the fundamental driving signal, as well as the 3rd order effects of the two-tone test in relation to the input power. Since the laser interferometer is used to detect the mechanical motion, and these measurements are very sensitive to any frequency changes, great care is taken to ensure measurement accuracy. First the x-y position of the laser is optimized for the largest signal on the resonator. Second, the fundamental frequency measurement is performed, followed

immediately by the interferer measurements. To check for consistency, the fundamental frequency measurement is repeated to ensure that the data lie on the same points, ensuring that the resonant frequency has not changed during the course of the experiment.

Output power, which is defined by the measurement system, is given in units of dB where the reference level is arbitrary. As expected from the bandpass nature of the mechanical response, the IM_3 strength is greater for in-band interferers than for out-of-band interferers. A Δf of 20 kHz produced an IIP_3 of +22 dBm while a Δf of 200 kHz produced a +35 dBm IIP_3 .

In order to determine the origin of the nonlinearity, the dome resonators were thermally driven into the nonlinear regime using a 415 nm wavelength modulated diode laser as well as through the electrical resistor. Figure 6-5 shows the output response of the dome resonator as a function of the input drive power for the same 12.7 MHz dome resonator mode. A network analyzer directly measures the driving power to the resistor; however, the dissipated power of the laser drive is determined by the gain in the diode laser controller, and thus the response can be arbitrarily translated along the horizontal axis in figure 6-5. In general, the laser drive generates larger resonator amplitudes for a given dissipated power because the beam is focused directly on the dome and the position of the laser focus spot is optimized to obtain the largest signal. The resistor is located off the resonator, which minimizes damping due to the metallic film on the resonator but reduces the coupling of the thermal drive. At an output power of -57 dB, the mechanical amplitude produced by both the resistor drive and the laser drive starts to compress, indicating that the onset of nonlinearity is due to large mechanical displacement in the resonator, while higher order nonlinearities in the resistive drive are negligible.

Data from figure 3-4 also suggest that nonlinearities are determined by the

resonator. For a constant V_o , the system response may be in either the linear or nonlinear regime, depending on the DC bias. A given V_o that produces a linear response in the resistor + resonator may result in a driving force, $V_o * V_{DC}$, which generates a nonlinear output signal, indicating mechanically determined nonlinearities. In addition, for each DC bias curve in figure 3-4, the 1 dB compression point occurs at the same output amplitude of approximately 2.5 mV from the photodetector as well as at the same $V_o * V_{DC}$ driving force of ~ 0.25 mW.

For vertical mechanical amplitude of 10 nm at the dome apex (corresponding to 0 dBm resistive drive in figure 6-5) we calculate an in-plane strain of 0.003% in the membrane. This deformation in the resonator is well within the linear elastic regime of the polysilicon film [71] and is unlikely to contribute to nonlinear behavior. Instead, nonlinearities are most likely geometrically produced through displacement-induced changes in the spring constant of the resonator. Figure 6-6 qualitatively illustrates how geometrical nonlinearities are induced in the resonator. Vibrations due to low excitation forces will only see one regime, where the spring constant is determined primarily by the one type of material spring constant. Geometrical nonlinearities are produced when high amplitude vibrations experience multiple displacement regimes where the spring constant is determined by either bending resistance or flexural rigidity, illustrating the spring constant's x dependence in equation 6-3.

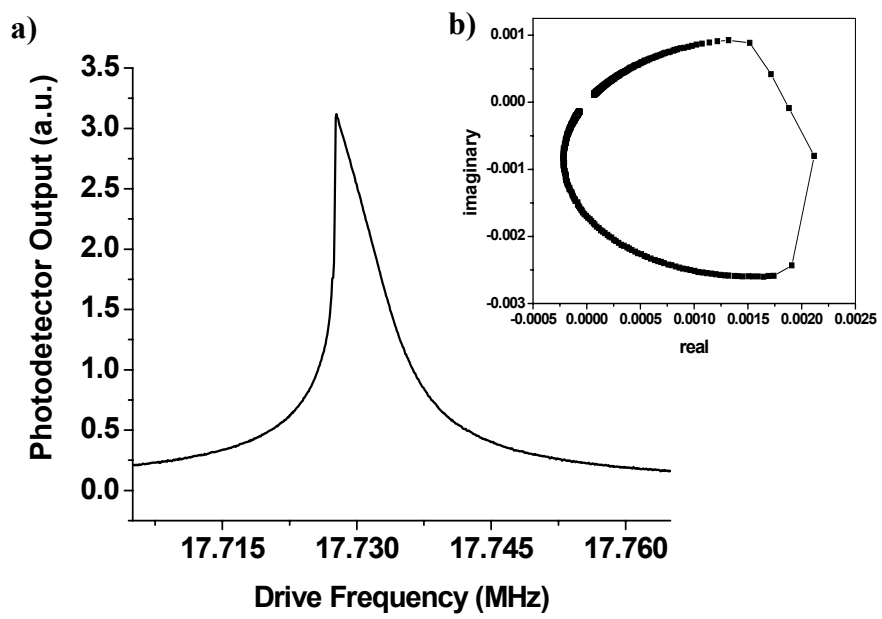


Figure 6-1: Nonlinear amplitude response (a) and nyquist plot (b) of a 30 μm resistively driven dome resonator.

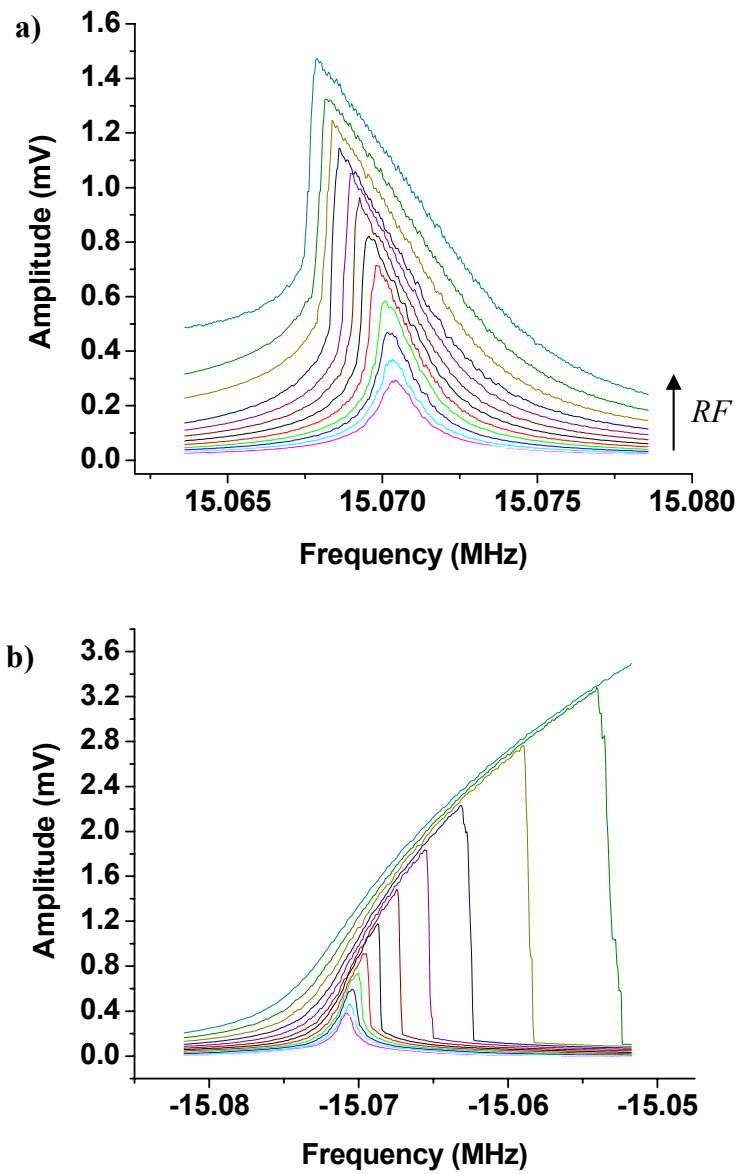


Figure 6-2: Experimental response curves from 30 μm dome resonator in response to varying RF power levels. As excitation voltage is increased, the response becomes more nonlinear – apparent in the backbending curvature. The 15 MHz softening curve in a) is measured by sweeping driving frequency from low to high. The same device is measured in b) but where the stimulus is swept from high to low.

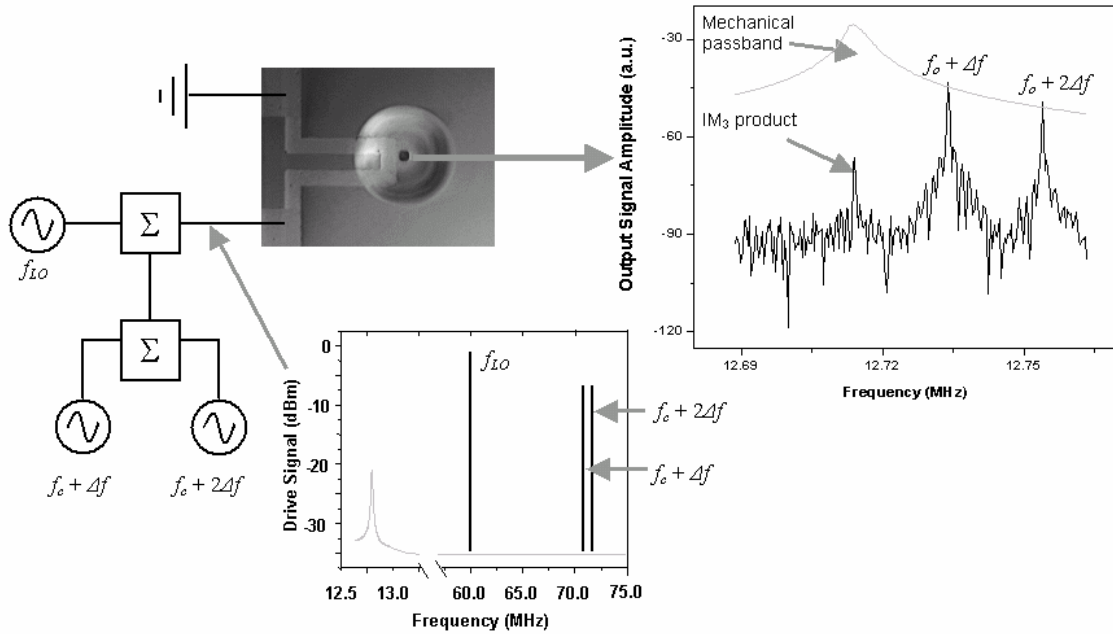


Figure 6-3: IM₃ experimental setup for the micromechanical mixer-filter. Two tones, offset from the carrier frequency by Δf and $2\Delta f$, along with a local oscillator signal, are superimposed on the resonator. A 3rd order intermodulation product at the resonant frequency of the dome, $f_o = 12.7$ MHz is subsequently produced in the mechanical vibrations.

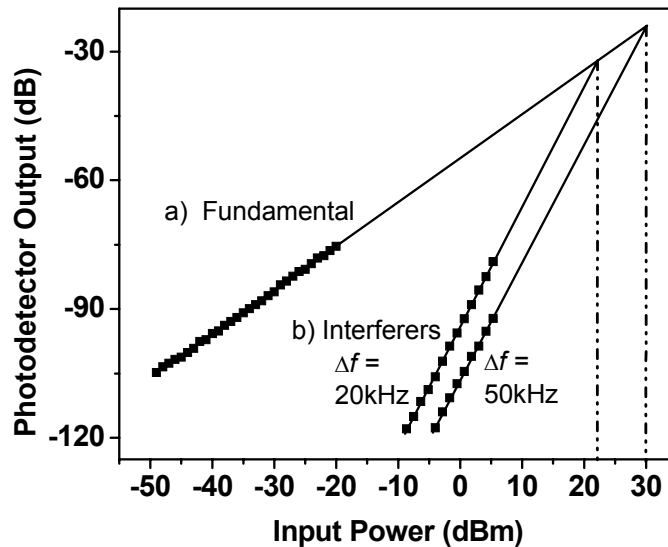


Figure 6-4: IM₃ experimental data from the MEMS mixer-filter showing the output response (with an arbitrary reference level) of the resonator at $f_o = 12.7$ MHz in response to a fundamental tone (a) and two off resonance tones spaced from the carrier frequency (72.7 MHz) by $\Delta f = 20$ kHz & 50 kHz (b).

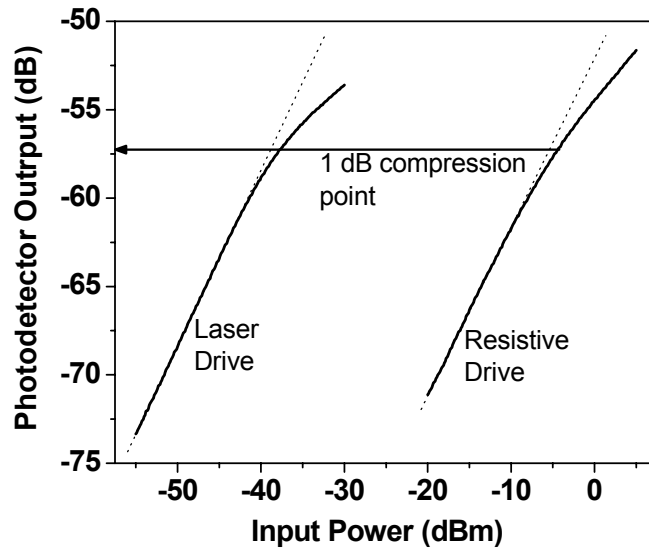


Figure 6-5: Curves showing the onset of nonlinearity for a $f_o = 12.7$ MHz resonator in response to a drive signal at f_o (resistor DC bias = 200 mV). The 1 dB compression point occurs at a -57 dB output amplitude for both laser thermal drive and resistive thermal drive.

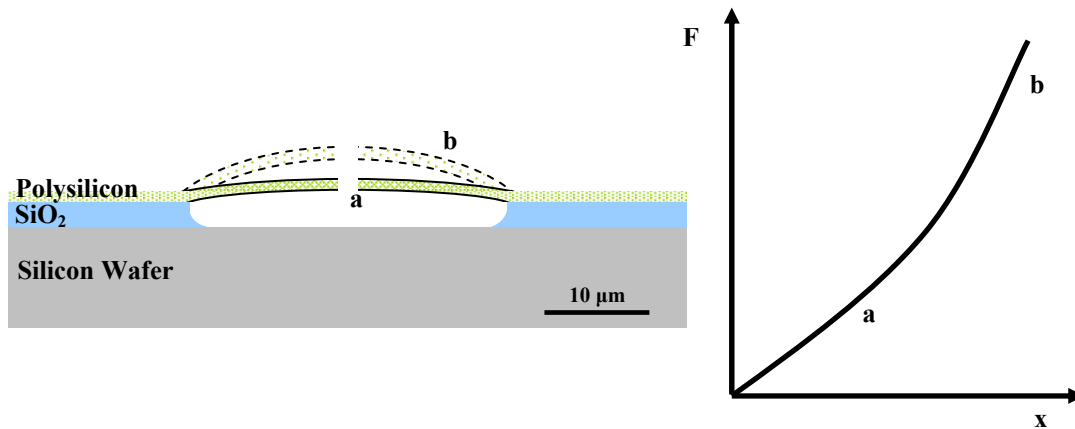


Figure 6-6: Conceptual diagram illustrating the spring constant's dependence on displacement for a nonlinear hardening mode of vibration. Resonator stiffness at displacement (a) is primarily determined by the bending resistance where as (b) is determined more by the flexural rigidity.

6.3 Analytical Model for Intermodulation

Because the nonlinearities in transduction are due to the mechanical resonator, we seek to understand how the dynamics of the resonator can produce the IM₃ product. We start by modeling the micromechanical filter under out-of-band interferer excitation with a variant of the weakly nonlinear Duffing equation:

$$\frac{d^2x}{dt^2} + \varepsilon \frac{\omega_o}{Q} \frac{dx}{dt} + (\omega_o^2 - \varepsilon\beta x^2)x = F_1 \sin[(\omega_o + \Delta\omega)t] + F_2 \sin[(\omega_o + 2\Delta\omega)t]. \quad 6-4$$

The right hand side of (6-4) is the forcing function provided by the resistive drive after frequency translation has been performed in the resistor, ε scales damping and nonlinearity as small perturbations to the linear oscillator, and $\beta > 0$ for a softening spring. We need to take the nonlinear term to be small so that, when the perturbation method is used, the system will be easy to solve in closed form when $\varepsilon = 0$. If the nonlinear term was not $O(\varepsilon)$, the starting solution would involve elliptic functions which would be much harder to work with. We also take the damping term to be small so that when $\varepsilon = 0$, the system is structurally unstable and the perturbation term can have a significant effect on the dynamics. Similarly, if the damping term was not $O(\varepsilon)$, then our starting solution would be of the form $e^{-kt} \sin(\omega t)$, and the decay term would stop forcing terms from being resonance terms, thus preventing the isolation of secular terms and rendering the solution method useless.

Perturbation theory is applied to (6-4) in order to gain insight into how the driving terms interact with the βx^3 nonlinear restoring force to produce a response at frequency ω_o . First, we expand the solution to (6-1) in the form of a power series in ε ,

$$x(t, \varepsilon) = x_0(t) + \varepsilon x_1(t) \quad 6-5$$

Substituting (6-5) into (6-4) and grouping terms according to powers of ε , while neglecting terms of order ε^2 and higher, we obtain:

$$O(0): \quad \frac{d^2 x_0}{dt^2} + \omega_o^2 x_0 = F_1 \sin(\omega_o + \Delta\omega)t + F_2 \sin(\omega_o + 2\Delta\omega)t \quad 6-6$$

$$O(1): \quad \frac{d^2 x_1}{dt^2} + \omega_o^2 x_1 = -\frac{\omega_o}{Q} \frac{dx_0}{dt} + \beta x_0^3 \quad 6-7$$

The solution to (6-6) is:

$$x_0 = R \cos(\omega_o t - \theta) + F_1 \frac{\sin(\omega_o + \Delta\omega)t}{\omega_o^2 - (\omega_o + \Delta\omega)^2} + F_2 \frac{\sin(\omega_o + 2\Delta\omega)t}{\omega_o^2 - (\omega_o + 2\Delta\omega)^2} \quad 6-8$$

where R and θ are constants to be determined. Substituting (6-8) into (6-7) results in a myriad of resonant and non-resonant terms. To eliminate secular terms, we set the coefficients of the resonant terms, $\sin(\omega_o t)$ and $\cos(\omega_o t)$, to be zero. Eliminating θ through use of the identity $\sin^2 \theta + \cos^2 \theta = 1$, we obtain a relation between R , the magnitude of the resonator response at ω_o , and the various parameters. This expression may be simplified by first solving for β and then neglecting all but the

lowest order terms in $\Delta\omega$ (since $\Delta\omega$ is assumed to be small compared to ω_o). Solving for R , the expression becomes:

$$R = \frac{3\beta F_1^2 F_2 Q}{64\omega_o^5 \Delta\omega^3} \quad 6-9$$

The full Macsyma command set to reach this solution is included in Appendix B. From the approximate solution (6-9) we see that through 3rd order nonlinearities present in the mechanical resonator, two appropriately spaced interfering signals will produce an interfering tone on resonance that will grow at a cubic rate, $F_1^2 F_2$, when compared to a tone at the fundamental frequency. Equation 6-9 also implies that intermodulation will substantially decrease as the interfering tones are offset from ω_o , which is experimentally demonstrated in figure 6-7. Finally, R is a decreasing function of the fundamental frequency, indicating that as we move to higher resonator frequencies, the magnitude of the intermodulation will decrease.

To further substantiate (6-9), we specifically examine the relationship between F_1 and R as well as between F_2 and R . Figure 6-7 shows two sets of experimental data from the IM₃ setup measuring the magnitude of the 3rd order intermodulation at ω_o . In the first set (figure 6-7 a) the power of the 1st interferer, $F_1 \sin(\omega_o + \Delta\omega)t$, is held constant, while sweeping the power of the 2nd interferer, $F_2 \sin(\omega_o + 2\Delta\omega)t$. As expected from (6-9), figure 6-7 indicates that $\log(R)/\log(F_2)=1$. The second experiment (figure 6-7 b) sweeps the power of the 1st interferer (F_1) and maintains a constant amplitude 2nd interferer. Again, following (6-9), $\log(R)/\log(F_1)=2$.

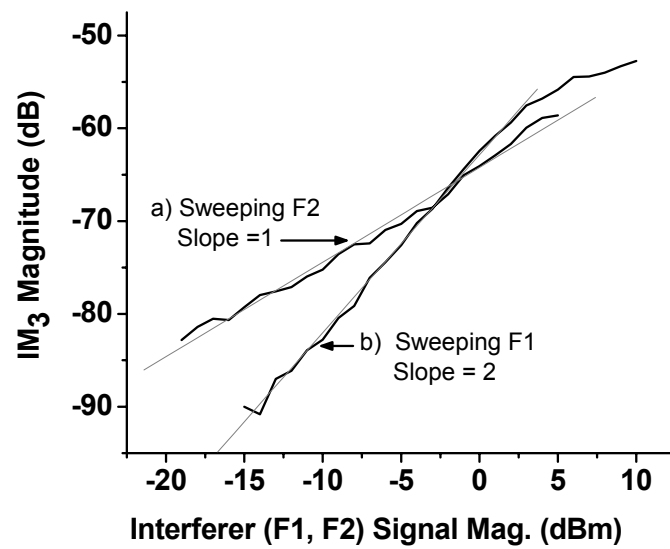


Figure 6-7: Magnitude of the resonator amplitude measured at the fundamental frequency, $f_o = 12.7$ MHz, in response to two interferers, where a) the magnitude of F_1 is 0 dBm and the magnitude of F_1 is indicated by the x-axis.

7 Conclusion

High frequency MEMS resonators have demonstrated outstanding performance as frequency-determining elements for communication systems. Featuring quality factors of $Q > 10,000$ and occupying real estate less than $50 \times 50 \mu\text{m}^2$, micromechanical devices are capable of revolutionizing radio frequency signal processing by replacing off-chip components with MEMS filters, oscillators, and mixers. Microminiaturized mechanical components offer significant advantages over macro-scaled electrical components in terms of linearity, cost, size, and power consumption; however they commonly suffer from the need for highly specialized fabrication steps to realize their physical form. Critically defined gaps, novel materials, and non-planar geometries represent significant barriers for integrating micromechanical resonant structures and their transduction elements into a CMOS environment.

This thesis presents a high frequency, shell-type, micromechanical resonator with integrated electrical-mechanical transduction, which is demonstrated to perform RF signal processing within the MHz and GHz range. Mechanical motion of a polysilicon thin-film plate or shell-type resonator is produced by the effects of heat transferred by a resistive microheater to the suspended structure. Detection of the resonant motion is enabled through an implanted piezoresistive active region. Thus, microresistors couple energy into and out-of the microresonator. Resistive coupling offers several advantages over electrostatic transduction: the actuators are broadband and can be impedance matched to the network, and their performance does not depend on nanometer scaled gaps surrounding the resonator. Thermal transduction is demonstrated to consume very low power as well as to preserve the intrinsic high quality factor of the micromechanical resonator. The high Q -factor allows narrow

frequency band selectivity and highly linear signal manipulation to be performed within the mechanical domain.

Since both the resonator and the resistive transducers can be fabricated within a polysilicon membrane, it is demonstrated how MEMS systems can be implemented into a single plane of silicon and defined immediately next to a field effect transistor in two CMOS processes. This thesis lays the groundwork for how a CMOS process can be designed to accommodate MEMS systems. It will be the subject of future research to determine how processing intricacies will affect the performance of the integrated MEMS resonator and CMOS electronics and to arrive at an optimized design for MEMS resonators in an IC environment.

Appendix A: Autostep 200 Setup Parameters

The following is a description of a setup program on the Autostep 200 5x stepper which will control the parameters of exposure for a program named “demo”

To perform a first level lithography process, only pass P1 would be run (i.e., exec p1).

To perform a second level lithography process, one would use the mapping pass to perform fine wafer alignment and then apply the corrections to the p1 pass. The command to expose the second level would be: map demo\map, p1

Program name:	demo	
Tolerance:	3	
Scale Corrections:	none	
Orthogonality:	none	
Leveler Batch Size:	1	
Wafer Diameter:	100	
x step size:	12.7	
count:	8	allows you to input # of columns
y step size:	12.7	
count:	8	
Translate origin:	none	
Standard keys:	y	
Right Key offset:	None	Ideally, the GCA keys should be located in the center of the die; if they are not, you will need to calculate the key offset.
Epi Shift:	None	
Pass Name	P1	
Use Local Alignment:	N	Exposure pass does not monitor DFAS keys
Exposure:	0.7	
Exposure Scale Factor:	1	
Focus Offset:	0	Sometimes needed for thick resist or film
Microscope offset:	0	
Enable Match:	Y	Uses DFAS marks on mask to fine align mask to stepper column. Only works if DFAS marks are on CAD (and on mask)
AWA Param File Name:	ORNL4	Only input if Match is Enabled
Pass Shift:	None	
Reticule Bar Code:	-	Automatically loads proper mask

Masking Aperture Setting:
 FX=FY=RX=RY: 12.5
 Reticle Alignment Offset: None
 Reticle Alignment Mark Phase: N
 Reticle Transmission: N
 A-RRAY or P-LUG A
 R: 1-8
 C: 8
 P
 D

Reduces mask field exposure

Allows you to subtract column and row
 eliminate row 1-8
 eliminate row 1-8 in column 8
 Inserts die into blank exposure field
 enter anytime to see die map on screen

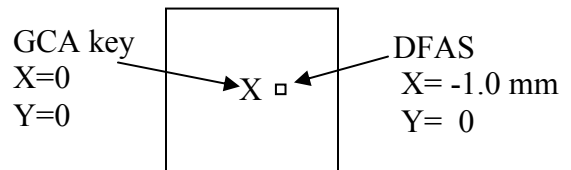
Pass Name **Map**
 Use Local Alignment: Y

Local alignment process uses map pass to
 look at DFAS marks on wafer to perform
 fine registration to the first level of
 lithography

Expose mapping pass: N
 Use two point align: Y
 rot tol: 2
 cont with map: Y
 # align/die: 1
 Local Align mark offset: --

Want to monitor die first before exposing

Where DFAS mark is on wafer (in mm)



Monitor Mapping Corr: Y
 Map every Nth wafer: 1
 A-RRAY or P-LUG P

Enter in 5 die on wafer at different
 locations

Save changes: Y
 Purge: Y

Appendix B: Macsyma code to solve ODE (6-4)

```

(c1)          foo(any):=any$
dummy function to zap abs value signs in sqrt later on
(c2)          depends([x,x0,x1],t)$
(c3) diff(x,t,2)+w0^2*x+e*c*diff(x,t)+e*beta*x^3=f1*sin((w0+dw)*t)+f2*sin((w0+2*dw)*t)$
(c4)          %,x=x0+e*x1,diff$
(c5)          taylor(%,e,0,1)$
C:\Macsyma2\library1\combin.fas being loaded.
(c6)          for i:0 thru 1 do eq[i]:coeff(%,e,i)$
(c7)          eq[0]$
(c8)          eq[1]$
(c9)          ode(eq[0],x0,t)$
C:\Macsyma2\ode\ode.fas being loaded.
C:\Macsyma2\ode\odeaux.fas being loaded.
C:\Macsyma2\ode\ode2.fas being loaded.
Is w0 zero or nonzero? N;
C:\Macsyma2\library1\trgred.fas being loaded.
C:\Macsyma2\library1\binoml.fas being loaded.
(c10)         x0soln:%,%k1=b,%k2=a$
(c11)         eq[1],%,diff$
(c12)         expand(trigreduce(expand(%)))$
(c13)         [coeff(%,sin(w0*t),coeff(%,cos(w0*t)))]$
(c14)         ratsimp(%)$
(c15)         [num(part(%,1,1)),num(part(%,2,1))]]$
(c16)         temp1:%,a=r*cos(h),b=r*sin(h)$
(c17)         part(%,1)*cos(h)-part(%,2)*sin(h)*dw$
(c18)         expand(%)$
(c19)         trigsimp(%)$
C:\Macsyma2\share\trigsimp.fas being loaded.
(c20)         temp2:solve(%,r)$
(c21)         factor(%)$
(c22)         part(temp1,1)*sin(h)+part(temp1,2)*cos(h)*dw$
(c23)         expand(%)$
(c24)         temp3:trigsimp(%)$
(c25)         factor(%)$
(c26)         temp4:solve(temp2,cos(h))$
(c27)         temp5:solve(temp3,sin(h))$
(c28)         sin(h)^2+cos(h)^2-1,%,temp4$
(c29)         RATSIMP(%)$
(c30)         NUM(%)$
(c31)         EXPAND(%)$
(c32)         temp6: FACTOR(%)$
(c33)         solve(%,beta^2)$
(c34)         taylor(%,r,0,2)$
(c35)         solve(%,r^2)$
(c36)         factor(%)$
(c37)         sqrt(%)$
(c38)         subst(foo,abs,%)$
(c39)         ev(%)$
(c40)         subst(w0,w0+dw,%)$
(c41)         subst(w0,2*w0+dw,%)$

```

(c42) D41;

$$(d42) \quad \begin{array}{l} 2 \\ 3 \text{ beta f1 f2} \\ [r = \text{-----}] \\ 3 \ 4 \\ 16 \text{ c dw w0} \end{array}$$

References

1. R. B. Reichenbach, M. Zalalutdinov, K. L. Aubin, R. Rand, B. Houston, J. M. Parpia, and H. G. Craighead, "Third-Order Intermodulation in a Micromechanical Thermal Mixer," *J. Microelectromech. Syst.*, vol. 14, no. 6, pp. 1244-1252, Dec. 2005.
2. R. B. Reichenbach, K. L. Aubin, M. Zalalutdinov, J. M. Parpia, and H. G. Craighead, "A MEMS RF Phase and Frequency Modulator," in *Proc. 13th International Conference on Solid-State Sensors, Actuators and Microsystems*, Seoul, Korea, June 2005. pp. 1059-1062.
3. R. B. Reichenbach, M. Zalalutdinov, J. M. Parpia, and H. G. Craighead, "A RF MEMS Oscillator with Integrated Resistive Transduction," Accepted to *Electron Device Lett.*, 2006.
4. H. C. Nathanson, W. E. Newell, R. A. Wickstrom, and J. R. Davis, Jr., "The resonant gate transistor," *IEEE Trans. Electron Devices*, vol. ED-14, pp. 117 – 133, 1967.
5. K. E. Peterson, "Micromechanical membrane switches on silicon," *IBM J. Res. Dev.*, 23, (4), pp. 376 – 385, 1979.
6. L. E. Larson, R.H. Hackett, M.A. Melendes, and R.F. Lohr, "Micromachined microwave actuator (MIMAC) technology - a new tuning approach for microwave integrated circuits," in *Microwave and Millimeter-Wave Monolithic Circuits Symposium Digest*, Boston, MA, June 1991, pp. 27 – 30.
7. C. T.-C. Nguyen, "Micromechanical devices for wireless communications," in *Proc. 1998 IEEE International Work shop on Micro Electro Mechanical Systems*, Heidelberg, Germany, Jan. 25 – 29, 1998, pp. 1 – 7.

8. M. Zalalutdinov, A. Zehnder, A. Olkhovets, S. Turner, L. Sekaric, B. Ilic, D. Czaplewski, J. M. Parpia, and H. G. Craighead, "Autoparametric optical drive for micromechanical oscillators," *Appl. Phys. Lett.*, vol. 79, pp. 695, 2001.
9. D. W. Carr and H. G. Craighead, "Fabrication of nanoelectromechanical systems in single crystal silicon using SOI substrates and electron beam lithograph," *J. Vac. Sci. Technol. B*, vol. 15, no. 6, pp. 2760 – 2763, 1997.
10. L. Sekaric, D. W. Carr, S. Evoy, J. Paria and H. G. Craighead, "Nanomechanical Resonant Structures in Silicon Nitride: Fabrication, Operation and Dissipation Issues," *Sens. Actuators, A*, vol. 101, no. 1 – 2, pp. 215 – 219, 2002.
11. K. L. Aubin, M. Zalalutdinov, Tuncay Alan, R. B. Reichenbach R. Rand, A. Zehnder, J. Parpia, and H. Craighead, "Limit Cycle Oscillations in CW Laser Driven NEMS," *J. Microelectromech. Syst.*, vol. 13, no. 6, pp. 1018 – 1026, Dec. 2004.
12. M. Zalalutdinov, J. W. Baldwin, M. H. Marcus, R. B. Reichenbach, J. M. Parpia, B. Houston, "Two-Dimensional Array of Coupled Nanomechanical Resonators," *Appl. Phys. Lett.*, vol. 88, no. 14, pp. 143504, Apr. 2006.
13. K. L. Aubin, M. Zalalutdinov, R. B. Reichenbach *et. al.* , "Laser annealing for high-Q MEMS resonators", in *Proc. of SPIE - Microtechnologies for the New Millennium*, vol. 5116 II, 2003, pp 531 – 535.
14. S. Verbridge, L. Bellan, R. B. Reichenbach, J. M. Parpia, H. G. Craighead, "High quality factor resonance at room temperature with nanostrings under high tensile stress," *J. Appl. Phys.*, vol. 99, no. 12, pp. 124304, 2006.
15. B. Ilic, Y. Yang, K. Aubin, R. Reichenbach, S. Krylov, H. G. Craighead; "Enumeration of DNA Molecules Bound to a Nanomechanical Oscillator," *Nano Lett.*, vol. 5, no. 5, pp. 925 – 929, May, 2005.

16. K. L. Aubin, B. R. Ilic, J. Huang, S. Park, Y. Yang, M. Kondratovich, and H. G. Craighead, "Microfluidic Encapsulated NEMS Resonators", submitted *J. Vac. Sci. Technol.*, 2005.
17. V. Kaajakari, T. Mattila, A. Oja, J. Kiihamaki, H. Kattelus, M. Koskenvuori, P. Rantakari, I. Tittonen, and H. Seppa, "Square-extensional mode single-crystal silicon micromechanical RF-resonator," in *Proc. Transducers, Solid-State Sensors, Actuators and Microsystems, the 12th International Conference on*, vol. 2, June 2003, pp. 951 – 954.
18. M. A. Abdelmoneum, M. U. Demirci, and C. T.-C. Nguyen, "Stemless wine-glass-mode disk micromechanical resonators," in *Proc. 16th Int. IEEE Micro Electro Mechanical Systems Conf.*, Kyoto, Japan, Jan. 19 – 23, 2003, pp. 698 – 701.
19. S. A. Bhave and R. T. Howe, "Silicon nitride-on-silicon bar resonator using internal electrostatic transduction," in *Proc. Transducers, Solid-State Sensors, Actuators and Microsystems, the 13th International Conference on*, vol. 2, June 2005, pp. 2139 – 2142.
20. R. C. Ruby, A. Barfknecht, C. Han, Y. Desai, F. Geefay, G. Gan, M. Gat, and T. Verhoeven, "High-Q FBAR filters in a wafer-level chip-scale package," in *Proc. of IEEE International Solid-State Circuits Conference*, 2002, pp. 184 – 185.
21. J. Bouchaud, H. Wicht, "RF MEMS: status of the industry and roadmaps," in *Proc. Radio Frequency integrated Circuits (RFIC) Symposium*, 12-14 June 2005, pp. 379 – 384.
22. B. Pillans, G. Rebeiz, J. B. Lee, "Advances in RF MEMS technology," in *25th Annual Technical Digest of Gallium Arsenide Integrated Circuit (GaAs IC) Symposium*, 2003, pp. 17 – 20.

23. R. B. Reichenbach, M. Zalalutdinov, K. L. Aubin, D. A. Czaplewski, B. Ilic, B. H. Houston, H. G. Craighead, and J. M. Parpia, "Resistively actuated micromechanical dome resonators," *Proceedings of SPIE, MEMS/MOEMS Components and Their Applications*, vol. 5344, San Jose, California, Jan. 26 – 27, 2004, pp. 51 – 58.
24. J. Cao and C. T.-C. Nguyen, "Drive amplitude dependence of micromechanical resonator series motional resistance," in *Digest of Technical Papers, 10th International Conference on Solid-State Sensors and Actuators*, Sendai, Japan, June 7 – 10, 1999, pp. 1826 – 1829.
25. Lecture notes from ECE 598, prepared by Prof. Amit Lal, 2004.
26. C.T.-C. Nguyen and R.T. Howe, "CMOS micromechanical resonator oscillator,"
in *Technical Digest – International Electron Devices Meeting*, 5 – 8 Dec. 1993
pp. 199 – 202.
27. S. Evoy, D. W. Carr, L. Sekaric, A. Olkhovets, J. M. Parpia, and H. G. Craighead, "Nanofabrication and electrostatic operation of single crystal silicon paddle oscillators," *J. Appl. Phys.* 86, pp. 6072, 1999.
28. P. Rantakari, V. Kaajakari, T. Mattila, J. Kiihamaki, A. Oja, I. Tittonen, and H. Seppä, "Low noise, low power micromechanical oscillator," in *Digest of Technical Papers The 13th International Conference on Solid-State Sensors, Actuators and Microsystems, TRANSDUCERS '05*, vol. 2, 5 – 9 June 2005, pp. 2135 – 2138.
29. T. Mattila, O. Jaakkola, J. Kiihamaki, J. Karttunen, T. Lamminmaki, P. Rantakari, A. Oja, H. Seppä, H. Kattelus, and I. Tittonen, "14 MHz micromechanical oscillator," *Sens. Actuators, A*, vol. A, pp. 497 – 502, April 2002.

30. A. N. Cleland, M. L. Roukes, "Fabrication of high frequency nanometer scale mechanical resonators from bulk Si crystals" *Appl. Phys. Lett.*, vol. 69, no. 18, Oct. 1996, pp. 2653 – 2655.
31. W.-C. Chen, J. Hsieh, and W. Fang, "A novel single-layer bi-directional out-of-plane electrothermal microactuator," in *Proc. The 15th International Conference on Micro Electro Mechanical Systems, MEMS2002*, 2002, pp. 693 – 697.
32. A. Tuantranont, V. M. Bright, L.-A. Liew, W. Zhang, and Y. Lee, "Smart phase-only micromirror array fabricated by standard CMOS process," in *Proc. The 13th Annual International Conference on Micro Electromechanical Systems, MEMS2000*, 2000, pp. 455 – 460.
33. A. Geisberger, M. Ellis, and G. Skidmore, "Toward micro system assembly," in *Proc. 5th International Conference on Integrated Nano/Micro/Biotechnology for Space and Medical and Commercial Applications*, 2002.
34. D. Girbau, A. Lazaro, and L. Pradell, "RF MEMS switches based on the buckle-beam thermal actuator," in *33rd European Microwave Conference*, vol. 2, 7 – 9 Oct. 2003, pp. 651 – 654.
35. H.D. Wu, K.F. Harsh, R.S. Irwin, W. Zhang, A.R. Mickelson, Y.C. Lee, J.B. Dobsa, "MEMS designed for tunable capacitors," in *MTT-S International Microwave Symposium Digest*, vol. 1, 7 – 12 June 1998, pp. 127 – 129.
36. H. Sehr, I. S. Tomlin, B. Huang, S. P. Beeby, A. G. R. Evans, A. Brunnschweiler, G. J. Ensell, C. G. J. Schabmueller, "Time constant and lateral resonance of thermal vertical bimorph actuators," *Journal of Micromechanics and Microengineering*, vol. 12, no. 4, July 2002, pp. 410 - 413.

37. K. L. Aubin, "Radio Frequency Nano/Microelectromechanical Resonators: Thermal and Nonlinear Dynamics Studies," *Ph.D. Thesis*, Cornell University, Ithaca, NY, Jan. 2005.
38. J. R. Clark, W.-T. Hsu, and C. T.-C. Nguyen, "Measurement techniques for capacitively-transduced VHF-to-UHF micromechanical resonators," in *Digest of Technical Papers, the 11th Int. Conf. on Solid-State Sensors & Actuators (Transducers'01)*, Munich, Germany, June 10-14, 2001, pp. 1118-1121.
39. D. W. Carr and H. G. Craighead, "Fabrication of nanoelectromechanical systems in single crystal silicon using silicon on insulator substrates and electron beam lithography," *J. Vac. Sci. Technol. B*, vol. 15, no. 6, pp. 2760, Nov/Dec 1997.
40. L. M. Roylance and J. B. Angell, "A batch fabricated silicon accelerometer," *IEEE Trans. Electron Devices*, vol. ED-26, pp. 1911 – 1917, Dec. 1979.
41. T. Toriyama, K. Sawa, Y. Tanimoto, S. Sugiyama, "Micromechatronics and Human Science," in *MHS '99. Proceedings of 1999 International Symposium on*, 23-26 Nov. 1999, pp. 215 – 220.
42. J. A. Harkey, T. W. Kenny, "1/f noise considerations for the design and process optimization of piezoresistive cantilevers" *J. Microelectromech. Syst.*, vol. 9, no. 2, June 2000, pp. 226 – 235.
43. W. P. Mason and R. N. Thurston, "Use of piezoresistive materials in the measurement of displacement, force and torque," *J. Acoust. Soc. Am.*, vol. 10, pp. 1096, 1957.
44. Bargatin, E. B. Myers, J. Arlett, B. Gudlewski, and M. L. Roukes, "Sensitive detection of nanomechanical motion using piezoresistive signal downmixing" *Appl. Phys. Lett.*, vol. 86, pp. 133109, 2005.

45. P.M. Morse and K.U. Ingard, *Theoretical Acoustics*, Princeton, NJ: Princeton University Press, 1986.
46. W. Soedel, "A Natural Frequency Analogy between Spherically Curved Panels and Flat Plates," *J. Sound Vib.*, vol. 29 no. 4, 1973, pp. 457.
47. M. Zalalutdinov, K. L. Aubin, M. Christopher, R. B. Reichenbach, T. Alan, A. Zehnder, B. Houston, J. Parpia, and H. Craighead, "Shell-type micromechanical oscillator", in *Proc. SPIE - Microtechnologies for the New Millennium*, v. 5116 I, 2003, pp. 229 – 236.
48. V. B. Braginsky, *Systems with Small Dissipation*, Chicago, IL: Univ. Chicago Press, 1985.
49. T. V. Roszhart, "The effect of thermoelastic internal friction on the Q of micromachined silicon resonators," in *Tech. Dig. 1990 Solid-State Sensor and Actuator Workshop*, Hilton Head, SC, 1990, pp. 13–16.
50. S. Nowick and B. S. Berry, *Anelastic Relaxation in Crystalline Solids*, New York: Academic Press, 1972.
51. C. Zener, "Internal Friction in Solids (II General Theory of Thermoelastic Internal Friction)," *Phys. Rev.* vol. 53, Jan. 1, 1938, pp. 90.
52. T. V. Roszhart, "The effect of thermoelastic internal friction on the Q of micromachined silicon resonators" in *Tech. Dig. of the 1990 Solid-State Sensor and Actuator Workshop*, Hilton Head, SC, 1990, pp. 13 – 16.
53. M. Panday, R. B. Reichenbach, and A. Zehnder, "Minimization of Anchor Losses in MEMS Resonators Using MESA Structures" to be published.
54. D. A. Czaplewski, J. P. Sullivan, T. A. Friedmann, D. W. Carr, B. E. N. Keeler, and J. R. Wendt, "Mechanical dissipation in tetrahedral amorphous carbon," *Appl. Phys.* vol. 97, no. 2, pp. 023517, Jan. 2005.

55. Reprinted from V. Mosser, J. Suski and J. Goss, "Piezoresistive pressure sensors based on polycrystalline silicon," *Sens. Actuators A*, vol. 28, 1991, pp. 113-132, with permission from Elsevier.
56. M. Zalalutdinov, K. L. Aubin, R. B. Reichenbach, J. M. Parpia, and H. G. Craighead, "Acoustic Method for Local Telemetry," Provisional Patent Application Serial Number 60/496,450, Aug. 2003.
57. B. Warneke, M. Last, B. Liebowitz, K.S.J. Pister, "Smart Dust: communicating with a cubic-millimeter computer" *Computer*, vol. 34, no. 1, Jan. 2001, pp. 44 – 51.
58. R. B. Reichenbach, M. K. Zalalutdinov, Keith L. Aubin, Jeffrey W. Baldwin, Brian Houston, J. M. Parpia, and H. G. Craighead, "Resonant Spectrum Identification," Provisional Patent Application Serial Number 60/793,334, April 2006.
59. B. van der Pol, "Forced oscillations in a circuit with non-linear resistance," *Phil. Mag.*, vol. 3, pp. 65 – 80, 1927.
60. M. Zalalutdinov, K. L. Aubin, M. Pandey, A. T. Zehnder, R. H. Rand, H. G. Craighead, and J. M. Parpia, "Frequency Entrainment for Micromechanical Oscillator," *Appl. Phys. Lett.*, vol. 83, pp. 3281 – 3283, 2003.
61. R. Adler, "A study of Locking Phenomena in Oscillators," *Proc. IEEE*, vol. 61, no. 10, pp. 1380 – 1385, 1973.
62. B. A. Razavi, "Study of Injection Locking and Pulling in Oscillators," *IEEE J. Solid -State Circuits*, vol. 39, no. 9, Sept. 2004, pp. 1415 – 1424.
63. K. Kurokawa, "Injection locking of Microwave Solid-State Oscillators," *Proc. IEEE*, vol. 61, no. 10, Oct, 1973, pp. 1386 – 1410.

64. G. M. Rebeiz, T. Guan-Leng, J. S. Hayden, "RF MEMS phase shifters: design and applications," *IEEE Microwave Magazine*, vol. 3, no. 2, June 2002, pp. 72 – 81.
65. B. Razavi, *RF Microelectronics*, Upper Saddle River, NJ: Prentice Hall PTR, 1998.
66. R. H. Rand, *Lecture Notes on Nonlinear Vibrations*, Published on-line by The Internet-First University Press, 2004, <http://hdl.handle.net/1813/79>.
67. K. L. Aubin, M. Zalalutdinov, T. Alan, R. B. Reichenbach, R. Rand, A. Zehnder, J. Parpia, and H. Craighead, "Limit Cycle Oscillations in CW Laser-Driven NEMS," *J. Microelectromech. Syst.*, vol. 13, no. 6, pp. 1018-1026, Dec. 2004.
68. R. Navid, J. R. Clark, M. Demirci, and C. T.-C. Nguyen, "Third-order intermodulation distortion in capacitively-driven CC-beam micromechanical resonators," in *Technical Digest, 14th Int. IEEE Micro Electro Mechanical Systems Conference*, Interlaken, Switzerland, Jan. 21-25, 2001, pp. 228-231.
69. S. A. Bhave, and R. T. Howe, "Internal Electrostatic Transduction for Bulk-mode MEMS Resonators," in *Dig. of Tech. Papers, the 12th Int. Conf. on Solid-State Sensors & Actuators (Transducers'03)*, Boston, Massachusetts, June 8-12, 2003, pp. 947-950.
70. V. Kaajakari, T. Mattila, A. Oja, and H. Seppä, "Nonlinear Limits for Single-Crystal Silicon Microresonators," *J. Microelectromech. Syst.*, vol. 13, no. 5, pp. 715-724, Oct. 2004.
71. W.N. Sharpe Jr, B. Yuan, R. Vaidyanathan, and R. L. Edwards, "Measurements of Young's modulus, Poisson's ratio, and tensile strength of polysilicon," in *Proc. 10th Annual International Workshop on Micro Electro Mechanical Systems*, Jan 26-30, 1997, pp. 424-429.